TECHNISCHE
UNIVERSITÄT
WIEN
Vienna University of Technology

Doctoral Thesis

Optimization of depth resolved X-ray absorption spectroscopy in grazing emission mode for characterizing compositionally complex alloys

submitted in satisfaction of the requirements for the degree
Doctor of Technical Sciences
supervised by

Ao. Univ. Prof. Dipl.-Ing. Dr. techn. Christina Streli
E141-Atominstitut
submitted at the Vienna University of Technology
Faculty of Physics
by

Cafer Tufan Cakir

[redacted]

Examining Board: Prof. Dr. **U. E. A. Fittschen**
Materials Analysis and Functional Solids
Clausthal Univeristy of Technology
Arnold-Sommerfeld-Str. 4, 38678 Clausthal-Zellerfeld, Germany
Prof. Dr. **Laszlo Vincze**
Department of Chemistry
Ghent University
Krijgslaan 281 - S3, B-9000 Ghent, Holland

Berlin, November 2024

Abstract

Layered materials are fundamental to technological advancements, offering distinct properties that differentiate them from bulk materials. In electronics, for instance, thin-film transistors (TFTs) are used to enhance charge transport and flexibility, thereby improving device performance. In the same way, thin-film photovoltaic devices used in renewable energy use strategic layering to absorb light more efficiently and separate electron-hole pairs more effectively, which leads to higher energy conversion efficiency. In recent decades, the development of new alloys has highlighted the importance of layered materials in another context. Compositionally complex alloys, for example, form multiple oxide layers on their surfaces when they oxidize. Studying these corrosion layers is crucial for understanding material-environment interactions.

Typical surface analysis techniques, including X-ray photoelectron spectroscopy (XPS), secondary ion mass spectrometry (SIMS), and Meitner-Auger electron spectroscopy (M-AES), provide valuable insights but are constrained by their requirements for high vacuum conditions and their limited depth analysis. In contrast, X-ray absorption near-edge structure (XANES) spectroscopy presents a versatile and advantageous alternative. It operates effectively under ambient conditions and allows time-resolved measurements, enhancing the analysis of materials in real-time as they undergo structural and compositional changes. This adaptability broadens the scope for material analysis, allowing for a more comprehensive understanding of dynamic processes.

Grazing Emission X-ray Fluorescence (GEXRF) spectroscopy stands out as a non-destructive, depth-resolved, element-specific characterization technique important for collecting depth-resolved information at the nanometer scale. Its ability to collect in-depth resolved information based on the grazing emission angle of the fluorescence radiation makes it ideal for investigating thin films, corrosion layers, and interfaces within layered materials. The integration of XANES in emission mode with GEXRF enables detailed exploration of the chemical states of the analyzed atom and provides depth-resolved information. This study discusses grazing emission X-ray absorption near-edge structure spectroscopy (GEXANES), a novel layer analysis technique that is created by integrating these two methods.

This study also innovatively combines machine learning with GEXANES spectroscopy to reduce experimental times. By using active learning, a subset of machine learning, it refines the data acquisition process, enabling more efficient and streamlined methods. The application of active learning in this context illustrates the potential of data-driven approaches to transform experimental methodologies, particularly in resource-limited environments such as synchrotron facilities, thereby accelerating scientific research and discovery.

Kurzfassung

Schichtmaterialien sind grundlegend für technologische Fortschritte und bieten Eigenschaften, die sie von Massivmaterialien unterscheiden. In der Elektronik werden beispielsweise Dünnfilmtransistoren (TFTs) verwendet, um den Ladungstransport und die Flexibilität zu verbessern, wodurch die Geräteleistung gesteigert wird. Auf die gleiche Weise verwenden Dünnschicht-Photovoltaikgeräte, die in der erneuerbaren Energie eingesetzt werden, strategische Schichtungen, um Licht effizienter zu absorbieren und Elektronen-Loch-Paare effektiver zu trennen, was zu einer höheren Energieumwandlungseffizienz führt. In den letzten Jahrzehnten hat die Entwicklung neuer Legierungen die Bedeutung von Schichtmaterialien in einem anderen Kontext hervorgehoben. Zusammensetzungsbedingt komplexe Legierungen bilden beispielsweise mehrere Oxidschichten auf ihren Oberflächen, wenn sie oxidieren. Das Studium dieser Korrosionsschichten ist entscheidend für das Verständnis der Wechselwirkungen zwischen Material und Umgebung.

Typische Oberflächenanalysetechniken, einschließlich der Röntgen-Photoelektronenspektroskopie (XPS), der sekundären Ionenmassenspektrometrie (SIMS) und der Meitner-Auger-Elektronenspektroskopie (M-AES), liefern wertvolle Einblicke, sind jedoch durch ihre Anforderungen an Hochvakuumbedingungen und ihre begrenzte Tiefenanalyse eingeschränkt. Im Gegensatz dazu stellt die Röntgen-Nahkanten-Absorptions-Spektroskopie (XANES) eine vielseitige und vorteilhafte Alternative dar. Es funktioniert effektiv unter Umgebungsbedingungen und ermöglicht zeitaufgelöste Messungen, wodurch die Analyse von Materialien in Echtzeit verbessert wird, während sie strukturelle und zusammensetzungsbedingte Veränderungen durchlaufen. Diese Anpassungsfähigkeit erweitert den Rahmen für die Materialanalyse und ermöglicht ein umfassenderes Verständnis dynamischer Prozesse.

Die Grazing Emission Röntgenfluoreszenz (GEXRF) Spektroskopie zeichnet sich als eine zerstörungsfrei, tiefenauflösende, element-spezifische Charakterisierungstechnik aus, die wichtig ist, um tiefenauflösende Informationen auf Nanometerskala zu sammeln. Seine Fähigkeit, detailliert aufgelöste Informationen basierend auf dem Streuwinkel der Fluoreszenzstrahlung zu sammeln, macht es ideal für die Untersuchung von Dünnschichten, Korrosionsschichten und Grenzflächen innerhalb geschichteter Materialien. Die Integration von XANES im Emissionsmodus mit GEXRF ermöglicht eine detaillierte Untersuchung der chemischen Zustände des analysierten Atoms und liefert tiefenaufgelöste Informationen. Diese Studie behandelt die Grazing Emission Röntgen-nahkanten-absorptions-Spektroskopie (GEXANES), eine neuartige Schichtanalysetechnik, die durch die Integration dieser beiden Methoden entstanden ist.

Diese Studie kombiniert auch maschinelles Lernen mit GEXANES-Spektroskopie, um die Experimentierzeiten zu verkürzen. Durch die Verwendung von aktivem Lernen, einem Teilbereich des maschinellen Lernens, verfeinert es den Datenakquisitionsprozess und ermöglicht effizientere und optimierte Methoden. Die Anwendung von aktivem Lernen in diesem Kontext veranschaulicht das Potenzial datengestützter Ansätze, experimentelle Methoden zu transformieren, insbesondere in ressourcenlimitierten Umgebungen wie Synchrotronanlagen, wodurch die wissenschaftliche Forschung und Entdeckung beschleunigt werden.

Acknowledgements

First, I would like to express my sincere gratitude to my supervisor, Dr. Christina Streli, for giving me the opportunity to undertake this work. Her guidance, support, and open communication have been invaluable throughout this journey.

I extend special thanks to my supervisors at BAM, Dr. Ana Guilherme Buzanich and Dr. Martin Radtke, whose inspiration, leadership, and patience in answering countless questions were instrumental in the successful completion of this work and in conducting the beamline experiments.

I am also deeply appreciative of my colleagues in the Structure Analysis division, as well as the division head, Dr. Franziska Emmerling, for fostering such a pleasant, inspiring, and open working environment.

I would like to honor the memory of Dr. Uwe Reinholz, whose contributions and commitment to the field have been a lasting inspiration. His presence is greatly missed.

I would also like to extend my heartfelt gratitude to my wife, Irem Duman Çakır, for her unwavering support, encouragement, and patience throughout this journey. Her presence and understanding have been a constant source of strength.

This work is dedicated to my son, Milo Mete Çakır.

Parts of this work have been published in the following publications:

- **Machine Learning for Efficient Grazing-Exit X-ray Absorption Near Edge Structure Spectroscopy Analysis : Bayesian Optimization Approach** Cakir, Cafer & Bogoclu, Can & Emmerling, Franziska & Streli, Christina & Buzanich, Ana & Radtke, Martin. Machine Learning Science and Technology (2024). 5(2).025037.
- **Exploring the Nb_2O_5 coating deposited on the Ti-6Al-4V alloy by a novel GE-XANES technique and nanoindentation load-depth.** Gelamo, Rogério & Leite, Natália & Amadeu, Nader & Tavares, Michel & Oberschmidt, D. & Klemm, Sophie & Fleck, Claudia & Cakir, Cafer & Radtke, Martin & Moreto, J. Materials Letters (2023). 355. 135584. 10.1016/j.matlet.2023.135584.
- **BAMline —A real-life sample materials research beamline.** Guilherme Buzanich, Ana & Radtke, Martin & Yusenko, Kirill & Stawski, Tomasz & Kulow, Anicó & Cakir, Cafer & Röder, Bettina & Naese, Christoph & Britzke, Ralf & Sintschuk, Michael & Emmerling, Franziska. The Journal of Chemical Physics (2023). 158. 10.1063/5.0157194.
- **Exploring the Depths of Corrosion: A Novel GE-XANES Technique for Investigating Compositionally Complex Alloys** Cakir, Cafer & Piotrowiak, Tobias & Reinholz, Uwe & Ludwig, Alfred & Emmerling, Franziska & Streli, Christina & Buzanich, Ana & Radtke, Martin. Analytical chemistry (2023). 95. 10.1021/acs.analchem.3c00404.

Other publications:

- **Time-, space- and energy-resolved in situ characterization of catalysts by X-ray absorption spectroscopy.** Peters, Stefan & Kunkel, Benny & Cakir, Cafer & Kabelitz, Anke & Witte, Steffen & Bernstein, Thomas & Bartling, Stephan & Radtke, Martin & Emmerling, Franziska & Abdel-Mageed, Ali & Wohlrab, Sebastian & Guilherme Buzanich, Ana. Chemical Communications (2023). 59. 10.1039/D3CC03277A.

- **Dispersive X-ray Absorption Spectroscopy for Time-Resolved In Situ Monitoring of Mechanochemical Reactions.** Guilherme Buzanich, Ana & Cakir, Cafer & Radtke, Martin & Haider, M. & Emmerling, Franziska & Oliveira, Paulo & Michalchuk, Adam. The Journal of Chemical Physics (2022). 157. 10.1063/5.0130673.

Conference contributions related to parts of this work have been presented as

Talks:

- C.T.Cakir, U.Reinholz, F.Emmerling, C.Streli, A.G. Buzanich, M.Radtke : Grazing exit X-ray fluorescence (GEXRF) analysis of high entropy alloys (HEA) and compositionally complex alloys (CCA), International Conference on High Entropy Materials ICHEM, 2020
- C.T.Cakir, U.Reinholz, F.Emmerling, C.Streli, A.G. Buzanich, M.Radtke: Unrevealing the depths of compositionally complex alloys with grazing exit XANES, The 18th International XAFS Conference XAFS, 2021, online
- C.T.Cakir, U.Reinholz, F.Emmerling, C.Streli, A.G. Buzanich, M.Radtke: Scanning-Free Grazing Exit XANES Analysis of Stratified Samples and the Optimization of the Data Collection Process, Denver X-Ray Conference DXC, 2022
- C.T.Cakir, U.Reinholz, F.Emmerling, C.Streli, A.G. Buzanich, M.Radtke: Optimization of Depth Resolved X-Ray Absorption Spectroscopy in Grazing Emission Mode for Characterizing Compositionally Complex Alloys, The 19th International XAFS Conference XAFS, 2022, online
- C.T.Cakir, U.Reinholz, F.Emmerling, C.Streli, A.G. Buzanich, M.Radtke: High Speed for High Entropy Materials, Berlin Science Week, 2022

Posters:

- C.T.Cakir, U.Reinholz, F.Emmerling, C.Streli, A.G. Buzanich, M.Radtke: Bayesian optimization for depth resolved analysis of complex alloys with grazing exit XANES, European Conference on X-ray Spectrometry EXRS, 2022

- C.T.Cakir, U.Reinholz, F.Emmerling, C.Streli, A.G. Buzanich, M.Radtke: Unravelling the depths of complex alloys with grazing exit XANES, Denver X-Ray Conference DXC, 2021, online

Contents

List of Figures

List of Tables

Chapter 1

Introduction

The emergence of nanoscale engineering and the increasing complexity of modern materials have created an urgent need for advanced analytical techniques that can study layered materials with a depth resolution beyond the existing methods. Layered materials play an important role in various technological advancements, offering unique properties that distinguish them from their bulk. For instance, in electronics, thin-film transistors (TFTs) leverage these layered configurations to enhance charge transportation and flexibility, thus increasing device performance [1]. Renewable energy technologies, like thin-film photovoltaic systems, also use strategic layering to maximize light absorption and ensure efficient electron-hole pair separation, leading to higher energy conversion efficiencies [2].

The study of corrosion, in which the corrosion damage significantly impacts the global economy—accounting for approximately 3.4% of the global GDP or US$2.5 trillion annually [3], also underscores the importance of layered materials. Layered materials formed because of oxidation are crucial for understanding how materials interact with their environments [4]. However, effectively addressing corrosion damage requires a deep understanding of the interactions that occur at material surfaces or interfaces. A better insight into the relationship between the corrosion process and surface composition can drive the development of new materials.

This is particularly relevant in the field of compositionally complex alloys (CCAs), which diverge from conventional material development strategies where small proportions of alloying elements are added to a base material and then heat-treated to meet the requirements of various applications [5]. CCAs offer an innovative approach by allowing the mixing of multiple elements in equal or near-equal proportions, leading to materials with superior structural properties suited for high-temperature applications and harsh environments, such as those found in the aerospace and power generation industries [6–8]. The components used in these applications often face challenges related to oxidation behaviors. Under extreme conditions, materials can degrade significantly due to corrosion. The complexity and atomic interactions of CCAs under varying conditions are not yet fully understood, with only a few studies addressing their surface degradation due to processing or corrosion [4, 5]. Thus, advancing our understanding of CCAs can provide insights into mitigating corrosion and enhancing material performance across multiple industries. The CrCoNi system was chosen as a test case due to its extensive prior characterization in the literature and its relevance as a CCA. By demonstrating the capabilities of the grazing emission X-ray absorption near-edge structure spectroscopy (GEXANES) on this well-studied material, the goal was to validate its effectiveness and highlight its potential for providing insight into the depth-resolved chemical states of complex alloy systems.

Numerous examples, including those mentioned above and others, highlight the crucial role of layered materials in a wide range of research and application areas [9–14]. This necessitates a deep understanding of the interactions at material surfaces or interfaces, paving the way for the further development of materials. This requires the use of nondestructive techniques that allow investigating these materials at ambient conditions.

Surface analysis techniques such as X-ray photoelectron spectroscopy (XPS), secondary ion mass spectrometry (SIMS), and Meitner-Auger electron spectroscopy (M-AES) are traditionally employed to study these complex layered materials. Despite providing valuable insights, these methods are limited by their need for ultra-high vacuum (UHV) conditions and their low depth analysis capabilities [15–20]. The specifics of these techniques are summarized in Table 1.1.

X-ray absorption near-edge structure spectroscopy (XANES) offers a versatile solution to overcome the limitations of traditional film analysis techniques. XANES provides information about the electronic structure and chemical state of the atom of interest. The ability to operate effectively under ambient conditions supports in-situ analysis, allowing

Methods	XPS	SIMS	M-AES	GEXANES
Probe Beam (In)	X-rays	Ions	Electrons	X-rays
Analysis Beam (Out)	Electrons	Ions	Electrons	X-rays
Sampling Depth (nm)	<10 nm	<2 nm	<7 nm	>10 nm
Sample environment	UHV	UHV	UHV	Ambient

Tab. 1.1: Comparison of Surface Analysis Techniques—XPS, SIMS, M-AES, and GEXANES detailing the probe and analysis beams, sampling depth, and sample environment required.

the tracking of changes in materials in different sample environments[21, 22]. Although XANES spectroscopy is a phenomenon related to absorption, the XANES spectrum can also be derived from emitted fluorescence radiation, providing versatility in data acquisition that allows angle-resolved XANES analysis in the emission mode.

X-ray fluorescence spectroscopy (XRF) is a non-destructive technique for analyzing material compositions. Angle-resolved XRF analysis, such as grazing emission XRF (GEXRF), provides depth-resolved information. This method is capable of obtaining information ranging from a few tens to several hundreds of nanometers [23, 24]. The combination of emission-mode XANES spectroscopy and grazing exit geometry provides detailed, depth-resolved insight into the electronic structure and chemical state of the atom under study [25, 26].

To perform GEXRF, two primary approaches are used to capture emitted XRF intensity as a function of the grazing emission angle. The first is the use of a one-dimensional (1D) energy-sensitive detector, which detects different emission angles by moving the detector position [27]. The application of a two-dimensional (2D) detector with spatial resolution allows direct intensity capture without the need for scanning [23]. In this work, a pnCCD was used as a detector, which allows scanning-free and energy-dispersive experiments to be carried out. Balancing angular resolution and fluorescence intensity was crucial. Specifically, the angular resolution is influenced by the distance between the detector and the sample; increasing this distance enhances the resolution (solid angle of detection per pixel). However, the intensity is inversely proportional to the square of the distance, meaning that as the distance increases, the intensity decreases. Consequently, a reduction in intensity will extend the experiment time. This balance is achieved by calculating the angular intensity profile that will be obtained from the GEXRF.

X-ray tubes can be used for GEXRF, but collecting multiple GEXRF datasets with low-flux X-ray tubes is a time-consuming process. However, synchrotron radiation is an excellent option for conducting GEXANES. The high flux of synchrotron radiation can overcome this issue.

This work not only combines GEXRF and XANES into GEXANES but also innovatively integrates machine learning with GEXANES to reduce experimental time. This approach aims to overcome the limitations of conventional analytical methods by leveraging the inherent strengths of XANES, taking advantage of the grazing exit geometry's depth-resolved information acquisition capabilities, and increasing the efficiency of data acquisition.

Machine learning, with its proven effectiveness in data analysis, image processing, and material synthesis, offers new ways to address challenges in the GEXANES data acquisition process [28–41]. The application of machine learning in this context represents an innovative direction whose potential to facilitate the data collection process has not yet been fully realized.

Active learning can change traditional, static data collection methods used in XANES spectroscopy and other research areas. Using mathematical models, active learning guides the optimization of data collection strategies. Within this framework, Bayesian optimization (BO) emerges as a particularly powerful tool for scenarios where function evaluation is expensive or time-consuming. BO uses prior probability distribution over the objective function and updates them as new data are acquired, thus aiding model interpretation and decision-making through its ability to quantify uncertainty via gaussian process regression (GPR) [42–46].

The incorporation of active learning exemplifies the broader impact of machine learning on experimental methods, marking a shift toward more efficient, data-driven approaches. This shift is particularly relevant in resource-constrained environments, such as synchrotron facilities. Machine learning, especially its active learning subset, has already been used in synchrotron radiation research with positive results, showing that it has the potential to make scientific investigations faster and more effective [47–53].

This work aims to address key questions crucial for enhancing material analysis capabilities.

- It will explore the application of spectroscopic techniques like GEXANES to provide depth-resolved insights into layered materials under non-destructive and ambient conditions.
- The study will investigate the integration of machine learning, particularly active learning techniques, to improve the efficiency of spectroscopic data acquisition. This includes examining the role of these computational methods in reducing data acquisition times and thereby increasing overall research productivity.

In order to answer a given key question, this work is divided into four chapters, as follows:

- **Chapter 2**, entitled "Theoretical Background," introduces the key concepts of X-ray-based spectroscopic methods. It begins with an overview of the historical development of these methods, focusing on their interaction with matter. This chapter then delves into the specifics of XRF spectroscopy and angle-resolved XRF analysis, providing a thorough explanation of the principles involved. Following this, it explores the theoretical background of GEXRF, which is central to this study, covering its historical background, the calculation of intensities, excitation sources, and the detection of emitted fluorescence radiation. The chapter concludes by highlighting X-ray absorption fine structure (XAFS) spectroscopy and discusses the application of machine learning in the data acquisition process to increase the time efficiency of the experiment. To this end, the focus is on active learning, in particular BO, as an innovative approach within this research area.
- **Chapter 3**, "Experimental Setup," details the experimental framework used in this study. It outlines the X-ray source and the detector involved in the detection of emitted fluorescence radiation. The chapter further examines the geometrical arrangements of the experimental setup, discussing the achievable depth of information. It proceeds to describe the data processing techniques employed, with a particular

focus on how BO has been implemented to enhance the experimental process. The chapter wraps up with a comprehensive description of the samples used throughout the study, setting the stage for the experimental analysis presented in subsequent chapters.

- **Chapter 4**, "Results and Discussion," integrates the presentation of results with their analysis. It begins with a proof of concept, examining the results obtained from a reference sample and discussing their significance. The chapter then presents findings from the analysis of a real-life CrCoNi sample, which was subjected to various temperatures for different durations. Additionally, it explores how layers influence angular intensity profiles and discusses the potential applications of this information in in-situ analysis. The final section of this chapter highlights the results derived from optimized experimental procedures, demonstrating the advantage of the study's integrated approach.
- **Chapter 5**, "Conclusion and Outlook," provides a summary of the study's main findings and contributions to the fields of material science and offers perspectives on future research directions, particularly emphasizing the promising role of machine learning and active learning in further advancing the capabilities of spectroscopic analysis and material characterization.

1.1 Theoretical Concepts Overview

This work's design required to consider a wide range of theoretical information. The most important ones were (1) the analytical method, which included the X-ray source, detection, and setup geometry; (2) the choice of optimization tools, such as machine learning; and (3) the samples that need the method developed here to answer a relevant analytical question, such as reference samples. The roadmap is mind-mapped in Fig. 1.1.

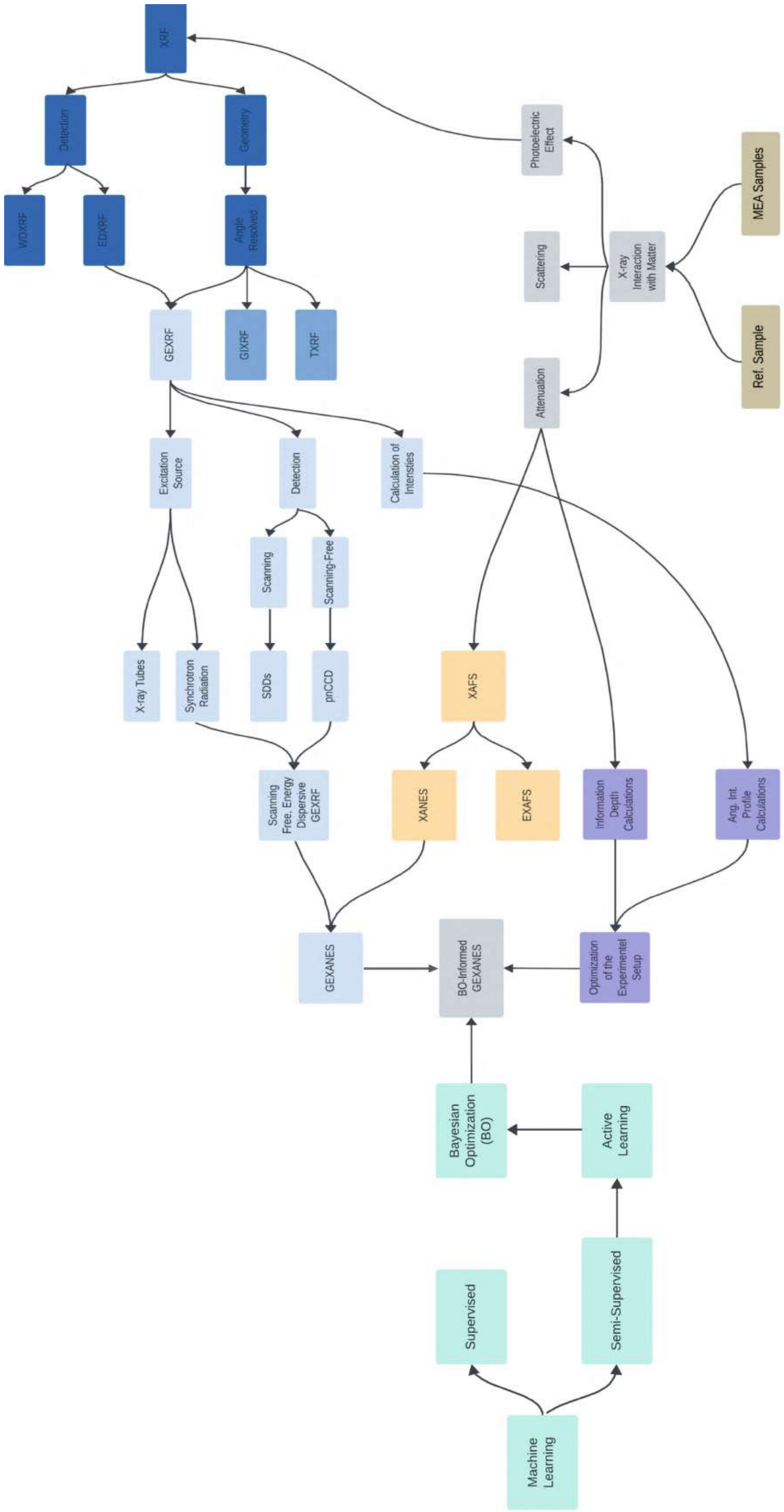

Fig. 1.1: The mind map illustrates the key components and their interconnections.

The mind map illustrates the following key elements:

- **Photoelectric Effect**: When XANES is in emission mode, it is linked to the photoelectric effect, which makes it possible to follow specific atomic fingerprints.
- **X-Ray Attenuation**: A fundamental understanding of X-ray attenuation is crucial for calculating the information depth in GEXANES analysis.
- **XRF Techniques**: A detailed understanding of how XRF works, and which geometries provide depth-resolved information is essential.
- **GEXRF Intensity Calculations**: It is crucial to calculate the solid angle of detection to establish the proper experimental setup. Calculating the angular intensity profiles beforehand ensures that the experimental parameters are optimized for accurate data collection.
- **X-ray sources**: Choosing the correct source knowledge for X-ray sources is crucial in this work. In GEXANES, selecting a high-flux, monochromatized X-ray source is important due to the shallow detection angle, which typically results in low counts.
- **Detectors**: Choosing the right detector needs a solid understanding of available detectors.
- **Chemical State Analysis**: Identifying the chemical states of atoms requires knowledge of XAFS, particularly XANES.
- **Active Learning**: Fundamental knowledge of machine learning, especially active learning, is essential to enhance the efficiency of data acquisition.

Chapter 2

Theoretical Background

The main ideas of X-ray-based spectroscopic techniques are introduced in this chapter. It starts with a summary of how these techniques have evolved historically, emphasising how X-rays interact with matter. This chapter then provides a thorough explanation of the fundamental ideas and goes into great detail about XRF spectroscopy and angle-resolved XRF analysis. The theoretical underpinnings of GEXRF, a crucial aspect of this study, are then examined. The historical context, intensity calculations, excitation sources, and detection of fluorescence radiation are all covered in this subsection. X-ray absorption fine structure (XAFS) analysis and XANES are then introduced in this chapter. This chapter concludes by providing the theoretical underpinnings of Bayesian optimisation (BO) and active learning as cutting-edge methodologies in this field of study.

2.1 Overview of X-ray Spectroscopy

For decades, X-ray spectroscopy has played a crucial role in material research. X-ray spectra reveal important insight into the atomic and electronic structure of materials by means of analyzing the emitted and/or absorbed radiation. With X-ray spectroscopy, one can obtain the elemental composition of the sample, resolving the chemical state and collecting information about the electronic structure. With this non-destructive analysis method, one can get deep insights into atomic and molecular information.

X-ray spectroscopy techniques such as X-ray fluorescence spectroscopy (XRF), which measures the emitted radiation from the sample, and X-ray absorption spectroscopy (XAS), which directly measures the absorbed portion of the radiation, will be described more in detail in the following sections.

2.1.1 Historical Development

In 1895, Wilhelm Conrad Röntgen accidentally discovered X-rays, and the history of X-ray spectroscopy began. While experimenting with cathode rays, Röntgen observed a mysterious glow emitted from a fluorescent screen placed near his instrument. This observed glow, which remained even when the cathode ray tube was shielded, was soon identified as a new type of penetrating radiation, which Röntgen named "X-rays"—the "X" denoting their unknown nature. The discovery earned Röntgen his first Nobel Prize in Physics in 1901 and caused a sensation in the scientific world. Due to their unique properties, X-rays have been an indispensable instrument in many fields since their discovery. In our daily lives and in cutting-edge research, X-rays play an essential role.

This specific part of the electromagnetic spectrum between extreme ultraviolet and gamma radiation is called X-rays. They exhibit wavelengths ranging from about 10 nanometers to 10 picometers, which correspond to frequencies ranging from about 30 PHz to 30 EHz. Additionally, X-rays carry energies in the range of 124 eV to 124 keV.

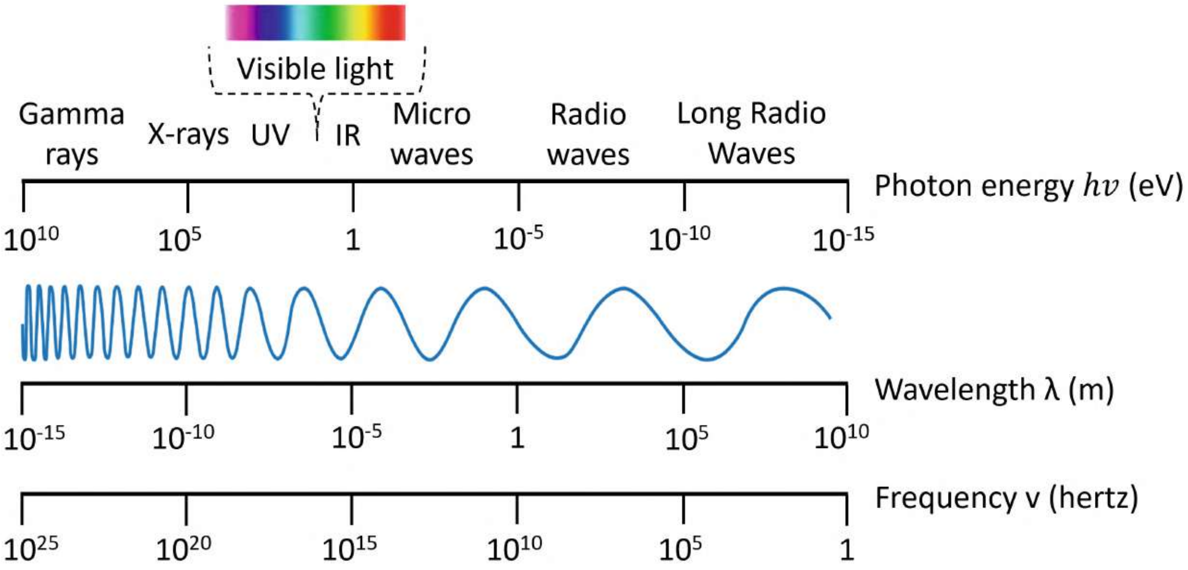

Fig. 2.1: Schematic representation of the electromagnetic spectrum. Adapted from [54].

Figure 2.1 is an electromagnetic spectrum chart, illustrating the relationship between frequency (in hertz), wavelength (in meters), and photon energy (in electron volts) for various types of electromagnetic radiation.

Early experiments with X-rays focused on understanding their behavior and properties. The first breakthrough result was that X-rays are absorbed differently by different elements when they pass through materials. As a result of this finding, X-rays began to be used for elemental analysis.

X-ray spectroscopy was rapidly developed in the 20th century. Instrumentation improved, techniques were refined, and the applications of X-ray spectroscopy expanded. One of the greatest progresses on this journey was the development of advanced X-ray sources, especially synchrotron radiation. Highly collimated and intense X-ray beams produced by synchrotrons improve the capabilities of X-ray spectroscopy. Such properties of the synchrotron's radiation allow for more detailed and faster analysis.

Detectors have evolved in parallel with advances in X-ray sources. Modern detectors have become more sensitive, faster, and capable of handling the intense beams from synchrotrons. Such improvements in the detectors provide the possibility to push the limits of X-ray spectroscopy even further.

To improve our fundamental understanding of X-ray spectroscopy, it is necessary to understand the interaction between X-rays and matter. Instead of passing through matter unchanged, X-rays undergo a series of different interactions. These interactions provide valuable information about the material. In the following sections, the interaction of X-rays with matter will be discussed in detail.

2.1.2 Interactions of X-rays with matter

X-rays interact with matter in several ways, including the photoelectric effect and scattering (both elastic, like Thomson or Rayleigh scattering, and inelastic, like Compton scattering). These interactions cause the overall effect of attenuation. The photoelectric effect is notable when the matter absorbs X-rays, and this process leads to the ejection of electrons from the atom. The scattering process occurs when photons are deflected by interactions with electrons or nuclei within atoms. These interactions can be elastic, where the photon is deflected without changing the energy states of the electrons, or inelastic, where the photon transfers energy to the electrons, possibly exciting them to higher energy states or removing them from their atoms (ionization). These interactions are crucial in various applications, from medical imaging to material analysis, and they are quantitatively described by the cross-section concept. The cross-section representing the effective area that quantifies the likelihood of an interaction is measured in barns ($1\ \mathrm{b} = 10^{-24}\ \mathrm{cm}^2$). The composition of the material and the energy of the incident X-rays affect the cross-section [55].

2.1.2.1 Photoelectric effect

In 1905, Albert Einstein introduced a groundbreaking theory of the photoelectric effect. The idea behind the theory is that the light is not just a continuous wave; it's made of individual packets of energy, called photons. Each photon carries an amount of energy given by the equation:

$$E = hv \tag{2.1}$$

where E is the photon's energy, v is its frequency, and h is Planck's constant.

If a photon has enough energy (hv) to overcome the atomic work function W, such an interaction causes the ejection of an electron with maximum kinetic energy K_{max} [56].

$$K_{max} = hv - W \tag{2.2}$$

The work function (W) is the minimum amount of energy needed to remove an electron from the material. It's connected to a specific threshold frequency (v_0). Below v_0, the photoelectric effect doesn't happen [56]. The following equation is used to describe this:

$$W = h(v - v_0) \tag{2.3}$$

Electrons within atoms, molecules, and solids are confined to specific states, each with a distinct binding energy ($E_{Bind.}$). When a photon delivers energy surpassing this binding energy to an electron, the electron can be ejected. The excess energy, which is the difference between the photon's energy hv and the electron's binding energy, is realized as the kinetic energy ($E_{Kin.}$), following the equation [56]:

$$E_{Kin.} = hv - E_{Bind.} \tag{2.4}$$

This kinetic energy distribution serves as a fingerprint of the quantum system. It mirrors the distribution of binding energies within the atomic, molecular, or crystalline structure. The photoelectron effect is shown in Figure 2.2.

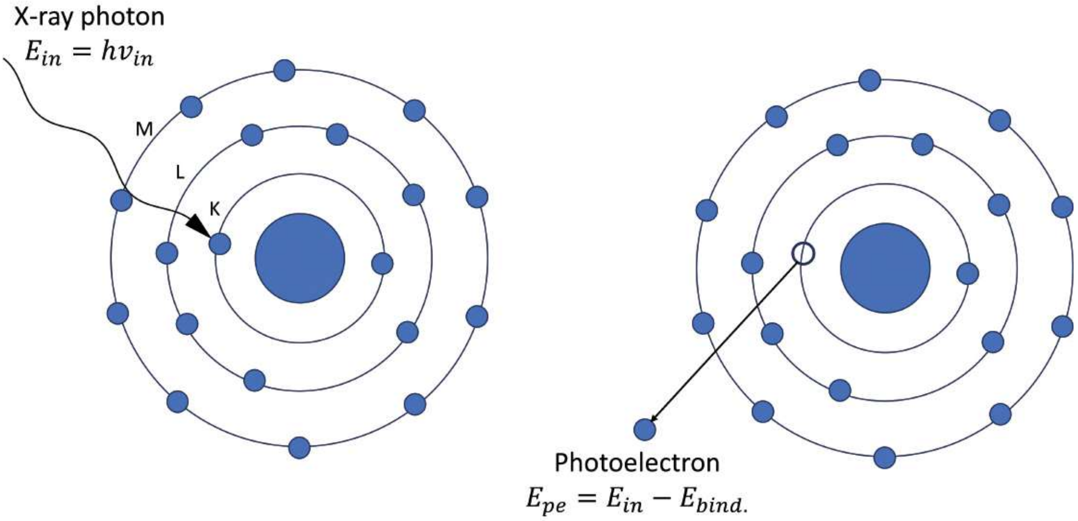

Fig. 2.2: Schematic representation of photoelectron generation.

An incoming photon can excite an atom if the energy of the photon is equal to or greater than the binding energy of the core-shell electron in the atom. The excited atom seeks to return to its equilibrium state. The process of returning to equilibrium involves fluorescence and the Meitner-Auger procedure.

When the outer shell electron fills the gap in the lower energy state, it releases the photon, called fluorescence radiation, with an energy equal to the energy difference between these two states. Since we already know that energy levels are elemental, each fluorescence ray therefore encapsulates elemental information. This relaxation process typically occurs quickly, with the photon often emitting within nanoseconds of the initial excitation [57].

The other relaxation mechanism is called the Meitner-Auger process, which is a non-radiative relaxation mechanism. After the inner shell electron is liberated, the electron from higher energy levels fills this gap, and an energy transfer occurs from the electron dropping into the lower energy state to another electron in an outer shell. This relaxation process is called the Meitner-Auger effect. Unlike fluorescence, the Meitner-Auger process results in the emission of an electron. The energy of the emitted Meitner-Auger electron is characteristic of the element, as it reflects the specific energy differences between the shells involved in the transition. This makes the Meitner-Auger process another valuable tool for elemental analysis. This mechanism also typically occurs rapidly, on a timescale comparable to that of fluorescence [58, 59]. Figure 2.3 shows the schematical representation of these two relaxation mechanisms.

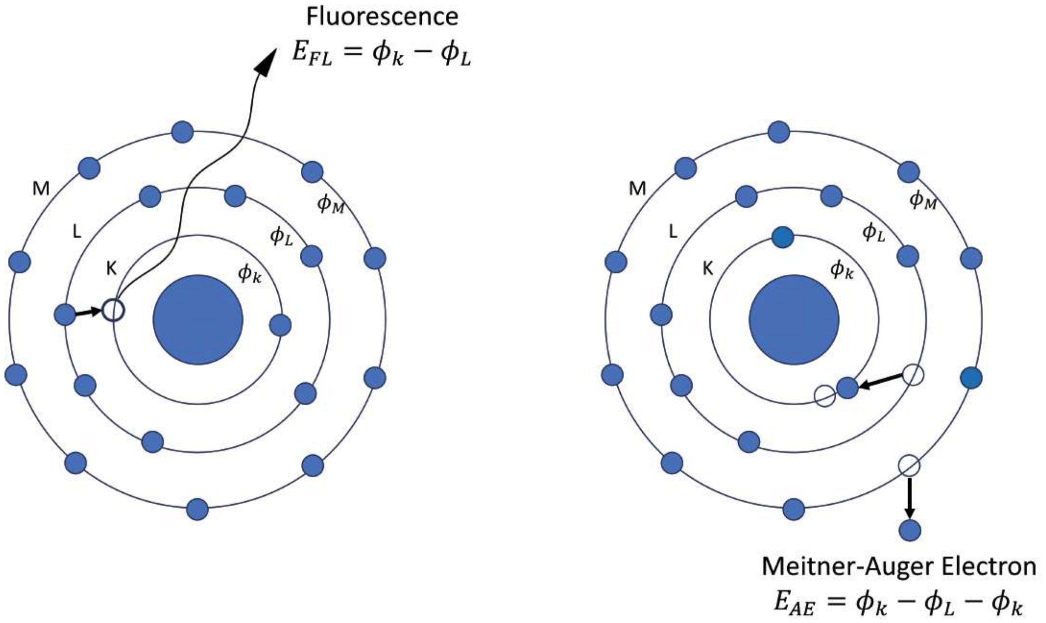

Fig. 2.3: Schematic representation of fluorescence photon and Meitner-Auger electron process.

2.1.2.2 Scattering

Another important interaction between X-rays and matter is scattering. In a scattering interaction, the incoming photon is scattered by the electrons of the atomic shell. Scattering can be classified into elastic (Rayleigh and Thomson) and inelastic (Compton) depending on the energy exchange and the state of the electron (free or bound).

Both Rayleigh and Thomson scattering are coherent processes, meaning the scattered radiation maintains the same frequency as the incoming light. This coherence is attributed to the photon stimulating the charged particle, whether free or bound, to oscillate at the incoming light's frequency. The oscillating particle then acts as a dipole emitter, radiating energy at the same frequency but in a different direction [60].

Rayleigh scattering occurs when photons interact with bound electrons. In Rayleigh scattering, the electrons are considered weakly bound relative to the energy of the incoming photon. The important characteristic of Rayleigh scattering is that while the direction of the photon may change, the energy remains the same [60].

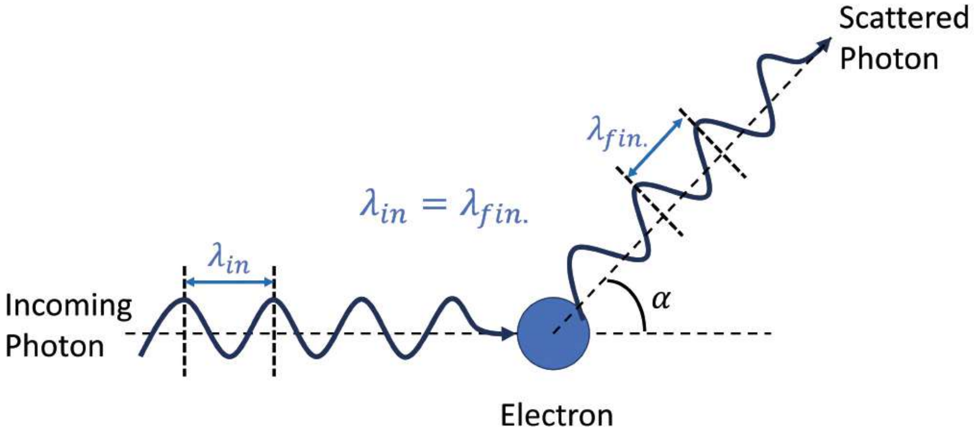

Fig. 2.4: Elastic scattering of an incoming photon with wavelength λ_{in} from an electron.

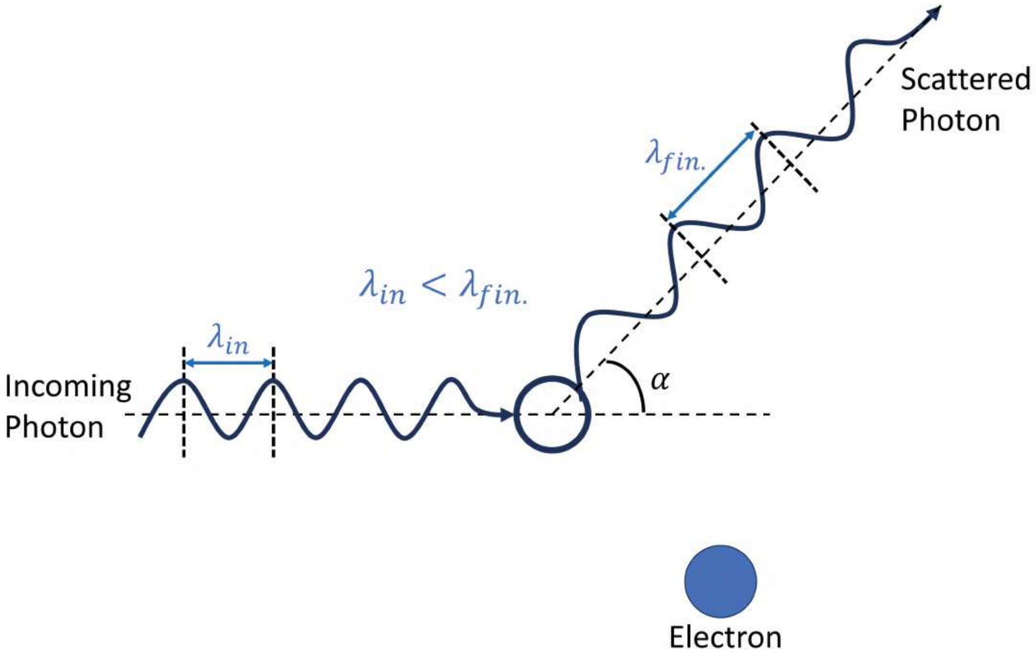

Fig. 2.5: Inelastic scattering of an incoming photon with wavelength λ_{in} from an electron.

On the other hand, Thomson scattering occurs when photons scatter off free or quasi-free electrons. These electrons are not bound to any atoms. They are free to interact with incoming photons. In this process, the energy of the photon remains unchanged after scattering. However, the direction of the photon can vary. Thomson scattering is often thought of as the classical limit of Compton scattering. It works when the photon's energy isn't high enough to significantly change the electron's kinetic energy [60]. Figure 2.4 shows the elastic scattering process.

Unlike elastic scattering, compton scattering, also known as incoherent scattering or inelastic scattering, involves the transfer of energy from the X-ray photon to an electron. As a result of this interaction, the electron from the atom is ejected. The scattered photon after interaction has reduced energy compared to the incident photon [60]. Figure 2.5 represents the inelastic scattering process.

2.1.2.3 Attenuation

When X-rays interact with matter, photons also experience loss of intensity, and this phenomenon is called attenuation. This process is described by Lambert-Beer law [61], which is illustrated in Figure 2.6.

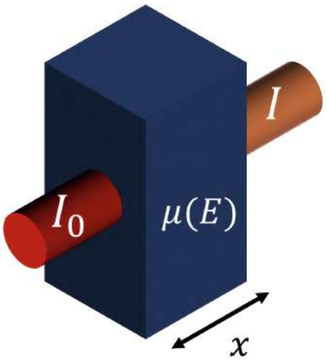

Fig. 2.6: Illustration of the Lambert-Beer's law $I_0 = Ie^{(-\mu(E)x)}$.

Where:

- I_0 represents the initial intensity of X-rays.
- I denotes the diminished intensity after the X-rays have passed through an absorber with a specific thickness x.
- The term $\mu(E)$ represents the linear attenuation coefficient. This coefficient varies based on the energy of the incoming photons and the properties of the material being interacted with.

The important role of the absorption cross section $\sigma(E)$, which has already been briefly explained, becomes apparent at the point of calculation of the linear attenuation coefficient $\mu(E)$, and their relationship can be expressed as follows [61]:

$$\mu(E) = \rho\sigma(E) \tag{2.5}$$

In this relationship, ρ represents the density of the absorbing material. The total absorption cross section, σ, is the sum of the cross sections resulting from the various interactions. This includes a range of phenomena from Thomson scattering and Compton scattering to photoelectric absorption and pair production [61].

In cases where the X-ray beam interacts with a mixture of different materials, the attenuation coefficient of the absorber is obtained by combining the coefficients of all its components [62].

Given the principles outlined previously, it's theoretically possible to calculate the depth the primary beam can reach within the observed material. Furthermore, the distance covered by the characteristic fluorescence originating from the sample can also be determined. Typically, this distance is measured in terms of length, where either the fluorescence or the primary beam experiences a reduction in intensity by approximately 37%, aligning with a $1/e$ ratio.

2.2 X-ray Fluorescence spectroscopy (XRF)

XRF takes advantage of the characteristic X-rays emitted by atoms, which are unique to each element due to their specific electronic configuration. These emissions act as a distinctive fingerprint that is essential for identifying and quantifying the elemental components of a sample.

XRF spectroscopy is a versatile and widely used analytical method. In academic research, it is employed to study diverse samples, while industries rely on it for quality assurance and process control to ensure products meet required standards and specifications. XRF is practical for analyzing major and trace elements in various materials due to its ease of application, low cost of sample preparation, and stability [63, 64].

Depending on the degree of sensitivity required, different detection methods and experimental geometry can apply XRF spectroscopy [63, 64]. The most common applications include the following:

By detection methods:

- Wavelength-Dispersive XRF spectroscopy (WDXRF)
- Energy-Dispersive XRF spectroscopy (EDXRF)

By experimental geometry:

- Total Reflection XRF (TXRF)
- Grazing Incidence XRF (GIXRF)
- Grazing Emission XRF (GEXRF)

WDXRF is a well-developed analytical technique used for the precise identification and quantification of elemental compositions. This method uses high-energy resolution analyzing crystals to disperse emitted fluorescence X-rays according to their wavelengths. This dispersion is crucial for X-ray lines closely spaced. They would overlap and become impossible to separate. WDXRF makes it possible to accurately find elements with closely spaced X-ray lines [63, 64].

A WDXRF setup includes several key components designed to achieve high spectral resolution:

- **The Analyzing Crystal** scatters the emitted X-rays based on their different wavelengths, which is crucial for the separation of X-ray lines.
- **The Goniometer** facilitates the rotation of the analyzing crystal and the detector, enabling the measurement of X-rays across a spectrum of wavelengths.
- **The Detector** captures and measures the intensity of the dispersed X-rays, providing essential data for determining elemental presence and concentration.

One way to find characteristic radiation in WDXRF is to use sequential scanning by an analyzer crystal-detector assembly and follow the Bragg condition. This lets you figure out the Bragg angle, crystal lattice parameters, and the wavelength or energy of the characteristic radiation. Another way characteristic radiation can be detected is by dispersing the XRF radiation simultaneously over a selected energy/wavelength range using a 2D array detector (such as a CCD or CMOS) [63, 64].

The technique is based on Bragg's Law ($n\lambda = 2d sin\theta$), where n is the diffraction order, λ the wavelength, d the lattice constant, and θ the Bragg angle, allows for precise determination of elemental compositions [63, 64].

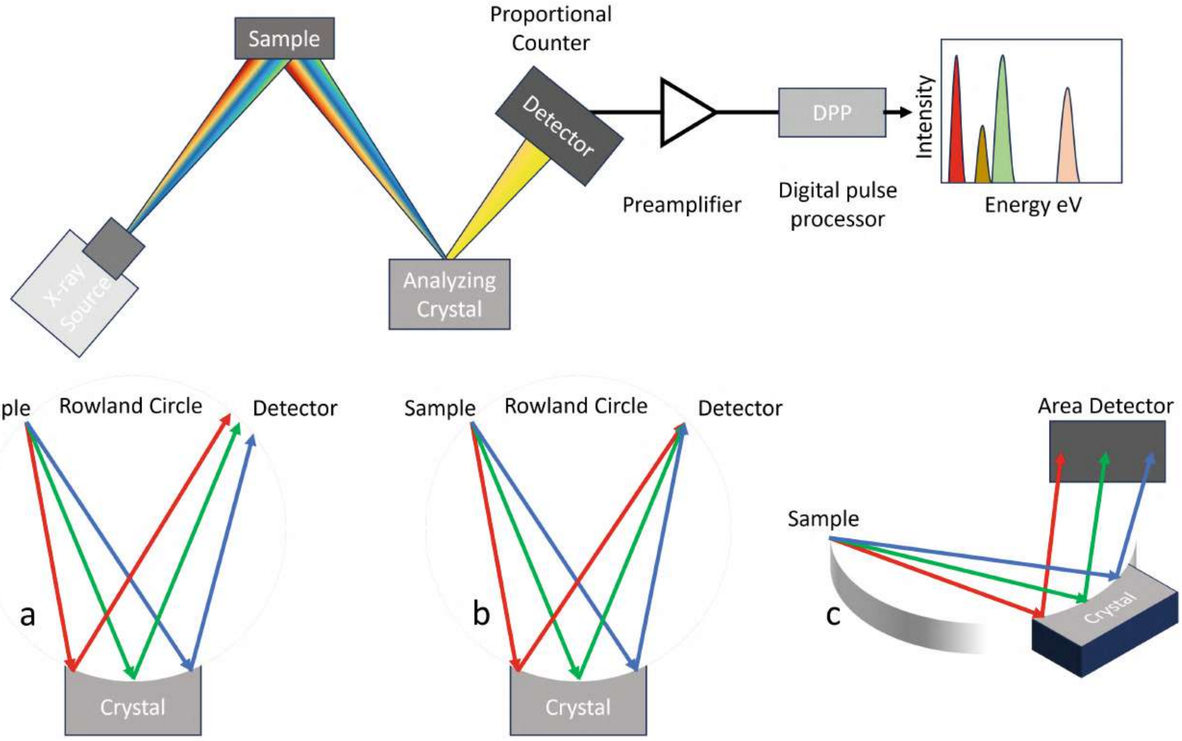

Fig. 2.7: Illustration of the WDXRF experimental setup. a) Johann Geometry, b) Johansson Geometry and c) Von Hamos Geometry

WDXRF spectroscopy has evolved with different geometries for enhanced performance, including:

- **Johann Geometry:** Introduced by H. H. Johann in 1931, utilizes a crystal where both the crystal planes and the surface have a 2R radius, leading to aberrations in the dispersed rays but offering ease of production.

- **Johansson Geometry:** Developed in 1933, features a crystal with lattice planes curved to a 2R radius and an inner surface polished to match the Rowland circle perfectly, ensuring X-rays deflected by the crystal converge on the same focal point without aberration.

- **Von Hamos Geometry:** Proposed by Von Hamos in 1932, employs a cylindrically bent crystal in the vertical direction to disperse radiation along a straight surface horizontally, focusing X-rays along the axis of curvature onto a single line on the detector chip.

Each geometry has its advantages, with the Johann and Johansson geometries using the Rowland circle for dispersion. Von Hamos geometry provides focused dispersion for increased sensitivity. Flat crystals are also used for their ease of production and instrument integration, but they have a lower sensitivity compared to bent crystals due to a decreased detected solid angle. Figure 2.7 illustrates the WDXRF setup with the Johann, Johansson, and Von Hamos geometries [63, 64].

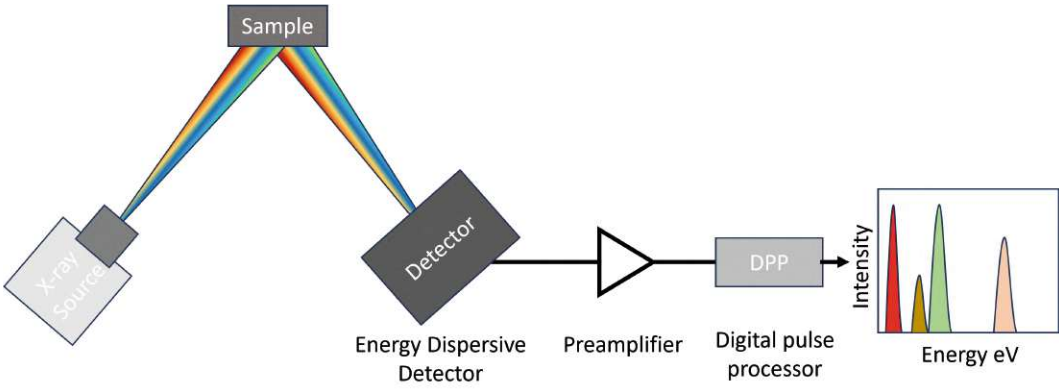

Fig. 2.8: Illustration of the EDXRF experimental setup.

WDXRF stands out for its high spectral resolution, enabling clear separation of closely spaced X-ray lines and the accurate detection of elements that may be difficult to distinguish using other techniques. This precision, coupled with the methodical design of the WDXRF apparatus and the strategic use of different crystal geometries, makes WDXRF a powerful tool in the field of material analysis [63, 64].

Energy-sensitive Si(Li) solid-state semiconductors or silicon drift detectors (SDD) achieve the detection of emitted X-rays based on their energy levels. EDXRF setup is more flexible than WDXRF and enables rapid simultaneous multi-element analysis, but this flexibility comes with some downsides, such as high spectral background and low energy resolution. Figure 2.8 shows a schematic representation of the EDXRF setup.

2.2.1 Angle resolved XRF analysis

Standard XRF techniques encounter challenges in analyzing thin films or nanoscale materials, primarily due to scattering from the substrate. The signal from the substrate can easily mask signals from the surface or near-surface regions. To address these issues, angle-resolved XRF techniques have been developed. These methods involve adjusting the angles of incident and detecting photons relative to the sample surface. By minimizing these angles, the information depth is reduced, thereby diminishing the influence of deeper sample layers and enhancing surface sensitivity.

Angle-resolved XRF techniques, such as total reflection XRF (TXRF), grazing incidence XRF (GIXRF), and grazing emission XRF (GEXRF), use this angular approach for detecting the surface of the analyzed material. These methods are particularly effective for analyzing surface-near elements, significantly improving thin-film analysis and applications requiring nanoscale resolution. Subsequent sections will delve deeper into the principles, methodologies, and applications of angle-resolved XRF analysis.

2.2.1.1 Total reflection XRF (TXRF)

The phenomenon of X-rays undergoing total reflection was first observed by Compton in 1923. He noted that the reflectivity of a flat target increases at angles below about 0.1°. Despite this discovery, it was not until 1971 that Yoneda and Horiuchi [65] realized the potential of this effect to increase the sensitivity of XRF analysis by placing the sample on a flat reflector. This method was further developed and elaborated by Wobrauschek in his doctoral research, and subsequent work by various researchers gave it the name "total reflection X-ray fluorescence analysis" or TXRF [66, 67].

TXRF is a powerful analytical technique with a wide range of advantages. It offers a wide elemental detection range covering almost the entire periodic table, from boron to uranium. With optimal excitation and detection conditions, TXRF can detect femtograms (10^{-15} g). TXRF offers fast analysis times, often just a few seconds, and can simultaneously detect multiple elements present in a sample [68].

TXRF works as an EDXRF method and uses the principle of total reflection of incident photons. When X-rays hit the sample at an angle smaller than the critical angle, the primary beam is almost completely reflected. Only a small fraction of this primary beam penetrates the sample. This leads to a significant reduction in the spectral background, typically caused by scattering on the substrate [67, 68].

Furthermore, once the incident beam is fully reflected from the sample, it ensures that the sample is excited by both the direct incident and reflected beams. This dual excitation effectively doubles the fluorescence intensity. TXRF's unique grazing angle geometry allows the detector to be positioned extremely close to the sample surface. This proximity provides a significant solid angle for the emitted fluorescence radiation to be captured, thus optimizing detection efficiency and minimizing background signals [67].

Interference occurs when two waves (in this case, the incident X-ray beam and its reflection) overlap. This overlapping produces what we call a "standing wave field." A standing wave field is characterized by stationary points where there seems to be no wave activity—these are called "nodes"—and points where the wave amplitude appears to be at its maximum, known as "antinodes". In the context of TXRF, this standing wave field is formed very close to the surface of a thick, flat substrate, such as the sample being analyzed. The pattern and spacing of these nodes and antinodes are influenced significantly by the angle at which the X-ray beam strikes the substrate. Particularly, this effect becomes pronounced at or near the "critical angle"—the angle where the reflection maximizes interference effects. The nodes (where there is minimal wave activity) and antinodes (where wave activity is maximal) are crucial because they influence how the sample is excited by the X-ray beams. The antinodes, having higher energy intensities, are particularly effective in exciting the atoms in the sample. This excitation is critical for enhancing the fluorescence emitted by the sample, which is what TXRF measures [67, 69].

TXRF has become a dominant tool in the semiconductor industry, primarily for the non-destructive analysis of surface contaminants. It is also a valuable method for chemical trace analysis, with impressive detection limits. With X-ray tube excitation, it can find contaminants as small as a picogram. When synchrotron radiation is used, it can find contaminants as small as a femtogram. The integration of synchrotron radiation into TXRF and angle-dependent XRF techniques in general is particularly advantageous. The inherent properties of synchrotron radiation, such as its high intensity, linear polarization, minimum source size, and inherent collimation, perfectly match the demands of these analytical methods, increasing their sensitivity and reliability [67].

2.2.1.2 Grazing incidence XRF (GIXRF)

Another angle-dependent XRF method, so-called grazing incidence X-ray fluorescence (GIXRF), is also an important analysis method in thin film analysis. This non-destructive analytical method offers insights into the composition and characteristics of thin layers. This method provides detailed information on the depth distribution and overall concentration of elements, even at nanometer depths.

GIXRF operates on the principle of analyzing the fluorescence emitted by a material when it is excited by X-rays at a grazing incidence. The primary X-rays penetrate deeper into the material with increasing angles of incidence, thus enabling the analysis of both the elemental composition within the layers and the underlying substrate.

The X-ray standing wave field is also a critical phenomenon in GIXRF, arising when the incident X-ray beam, with low divergence and monochromatic properties, interferes with its reflection from the flat surface of the sample. This interference generates a standing wave pattern at the surface and near-surface regions. The intensity of the X-ray standing wave field varies significantly with the depth and the angle of incidence, which in turn markedly enhances the fluorescence intensity emitted by the sample. This enhancement is pivotal for increasing the sensitivity of GIXRF, allowing for the detection and quantification of elements present in the thin films with high accuracy. Despite its advantages, the sensitivity of GIXRF to deeper layers is somewhat limited. The enhancement effect of the X-ray standing wave field predominantly benefits the first few nanometers of the sample surface. Beyond this depth, the influence of the X-ray standing wave field on fluorescence intensity diminishes, leading to a slight degradation in sensitivity for elements located further within the material [70].

Parratt's work of 1954 [71] is an important contribution to the historical development of GIXRF. He pioneered a method that takes into account the angle of incidence to clarify the modulation of the electromagnetic field, while also considering phenomena such as reflection and refraction at interference near surfaces. Parratt's calculations provide the basis not only for X-ray reflectivity (XRR) but also for GIXRF analysis.

The core of his work suggests that understanding the field dynamics allows predictions to be made about photoelectric absorption events and subsequent fluorescence photons. This theoretical framework was practically demonstrated by Becker et al. in 1983 [27] using a homogeneous sample, showing how a decaying field can activate atomic responses in materials. Based on this, Iida et al. investigated an arsenic-implanted layer in silicon using synchrotron radiation in 1986 [72]. By 1991, de Boer [73] further enriched the field by introducing a rigorous derivation of fluorescence in layered samples. In particular, de Boer's work was the first demonstration of simultaneous measurement and analysis of GIXRF and XRR in stratified media [74]. However, ongoing developments in nanofabrication and material science have since addressed these challenges, enabling more precise control over thin film production and, by extension, expanding the application of GIXRF [75].

2.3 Grazing emission XRF (GEXRF)

The theoretical framework for analyzing X-ray standing waves was established by Parratt in 1954 [71], offering a rigorous mathematical model for their study. This groundwork facilitated the accurate quantitative analysis that was crucial in grazing-angle fluorescence studies. Further development of the Parratt findings was done by Becker et al. in 1983 [27]. This study explains the shared principles of GIXRF and GEXRF. They highlighted the principle of microscopic reversibility, asserting that the characteristics of the electric field between two points in emission and detection scenarios are invariant. This discovery confirmed the natural theoretical link between GIXRF and GEXRF, showing how they can be used together to learn more about X-ray fluorescence phenomena.

While GIXRF and GEXRF work on a basic level, they are set up in a way that makes the roles of excitation and detection in the X-ray fluorescence process reversed. In other words, in GEXRF, the primary beam is perpendicular to the sample surface, and the detection of the emitted radiation is made at a shallow detection angle. Due to perpendicular penetration of the primary beam, the XSW pattern is not created in this experimental setup. As shown in Figure 2.9, this change flips the technique from angle-dependent excitation under grazing incidence conditions (GIXRF) to angle-dependent detection under grazing emission conditions (GEXRF). Crucially, owing to the principles of microscopic reversibility and reciprocity [76], these setups are physically equivalent. This means that when both GIXRF and GEXRF experiments use the same wavelength (λ), they yield identical atomic distributions in the fluorescence outcomes [71]. This equivalence shows that X-ray fluorescence can be studied in a very consistent way, whether it is through incidence or emission [70].

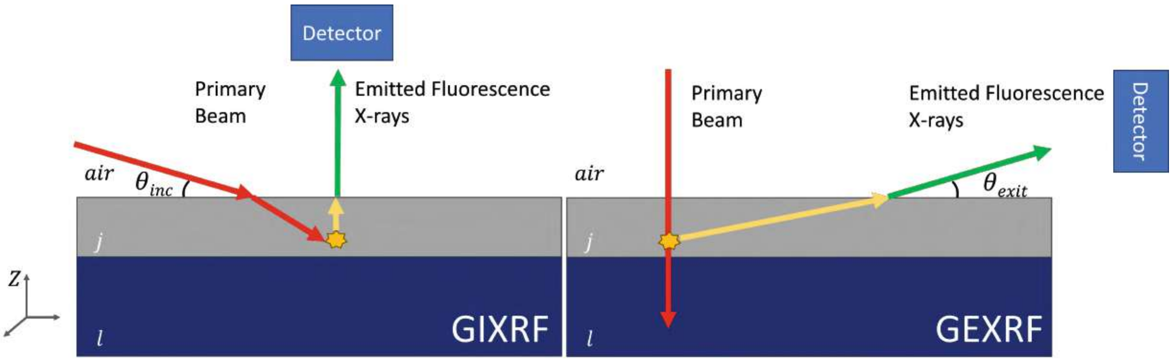

Fig. 2.9: Illustration of the basic concept for GIXRF and GEXRF experimental setups.

The principle of reciprocity, which comes from the way radiating dipoles behave, says that switching the positions of the source and the detector does not change the outcome of an interaction. Mathematically, for two dipoles at positions r_1 and r_2 with moments P_1 and P_2, the reciprocity theorem is expressed as follows [77]:

$$\vec{E}_1(\vec{r_2}) \cdot \vec{P}_2 = \vec{E}_2(\vec{r_1}) \cdot \vec{P}_1 \tag{2.6}$$

Where:

- The electric field $\vec{E}_k(\vec{r_l})$ represents the field generated at position $\vec{r_l}$ by a radiating source situated at $\vec{r_k}$.

Equation 2.6 demonstrates that swapping the positions of the source and detector does not alter the outcome, illustrating the principle of reciprocity for sound and electromagnetic waves. This concept has historical roots tracing back to the works of Rayleigh, Stokes, Lorentz, and Helmholtz [77].

The unique aspect of GEXRF lies in its surface sensitivity, achieved through specific emitted angles. At small angles relative to the sample surface, ranging between 0 mrad and the material's critical angle, only XRF emitted by atoms in the first tens to hundreds of nanometers is detectable. When X-rays come from atoms deeper inside the sample, they are reflected away from the surface as they pass through the interface. This is similar to how they come in during GIXRF, but it goes the other way [70].

When the observation angle exceeds the critical angle, fluorescence signals from deeper within the sample become observable. However, the effective probed depth remains within the submicrometer scale due to shallow observation angles that extend the emission paths within the sample, leading to significant absorption.

Based on these principles, GEXRF enables precise 2D mapping by using an X-ray microbeam. This technique benefits from synchrotron radiation micro-beams [78, 79] and polycapillary X-ray optics [80, 81]. Moreover, by integrating depth profiling with surface-sensitive scans, GEXRF setups facilitate 3D scanning capabilities [80], which increases the analytical range of the method.

GEXRF has also been enhanced by the adoption of position-sensitive detectors, allowing for the acquisition of complete angular profiles in a single measurement without the need to scan across different grazing emission angles [23, 82, 83]. This innovation streamlines the data collection process, significantly reducing the time required for comprehensive angular analyses [84].

GEXRF has been effectively applied in trace element analysis [79, 85] and the characterization of thin films [23, 86, 87], as well as in depth profiling studies [82, 88]. GEXRF and

XAFS were used together to show depth-resolved absorption studies in emission mode in Kayser et al. (2015) and Cakir et al. (2023) [26, 89].

Despite its advantages, GEXRF faces challenges related to its lower sensitivity, a consequence of the reduced solid angle of detection. This results in higher detection limits compared to GIXRF, where energy-dispersive detectors are positioned closer to the target surface, capturing a larger solid angle [26, 80]. Also, grazing emission conditions made absorption effects stronger because the path lengths through the sample were longer, which changed the sensitivity and detection limits [84, 90].

This work depends on GEXRF since it enables the gathering of depth-resolved data, which is essential to grasp the complex characteristics of layered materials. With a high angular resolution setup, GEXRF enables the detection of XRF signals from varying depth levels, providing detailed insights into the compositional changes across a sample. Moreover, its capability to operate under ambient conditions facilitates in-situ analysis, allowing for real-time observations of dynamic processes and interactions within materials.

2.3.1 Calculation of the intensities

GEXRF is essential to this study because it makes it possible to gather depth-resolved data, which is necessary to comprehend the complex characteristics of layered materials. With a high angular resolution setup, GEXRF enables the detection of XRF signals from varying depth levels, providing detailed insights into the compositional changes across a sample. Moreover, its capability to operate under ambient conditions facilitates in-situ analysis, allowing for real-time observations of dynamic processes and interactions within materials.

Figure 2.10 represents the interaction between emitted fluorescence radiation and the interfaces of various layers. As the primary beam enters the sample, it excites atoms along its path, leading to the emission of characteristic fluorescence radiation. Upon reaching the interface between air and the medium j, the emitted radiation faces two potential outcomes: a portion may pass through into the air, while the rest may be reflected at the air and medium j interface. A similar phenomenon occurs when the reflected fluorescence radiation meets the interface between medium j and medium l; it is either transmitted through medium l or reflected. This reflection from the medium l can cycle back to the air and medium j interfaces, initiating a continuous loop of reflection and transmission. The calculation's main goal is to ascertain the proportion of fluorescence radiation that is transmitted into the air through these interactions.

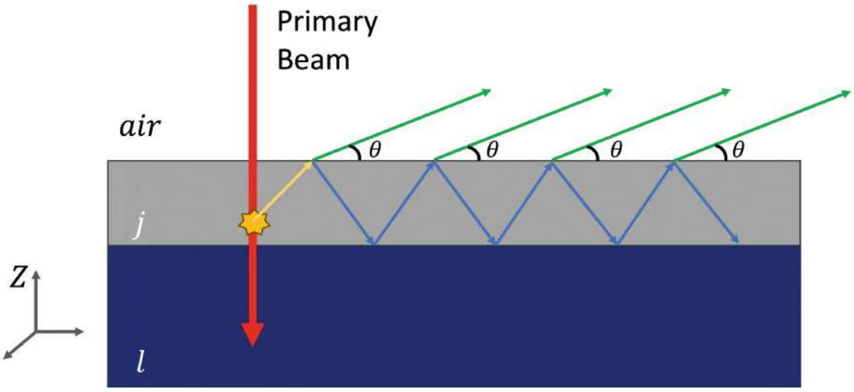

Fig. 2.10: Illustration of the transmission and reflection of the emitted fluorescence radiation between different mediums.

To accurately model this process, it is essential to consider and calculate three critical phenomena that occur:

- **Change in Field Strength:** This involves quantifying how the field strength of the emitted fluorescence radiation changes as it transmits from the surface through to the air.
- **Intensity Loss:** This accounts for the attenuation of fluorescence radiation's intensity as it propagates within the layer, a crucial factor in understanding the overall transmission efficiency.
- **Refraction and Reflection:** This describes how the intensity and phase of the emitted light is modified after multiple reflections within the layer before it exits.

These factors collectively enable a comprehensive analysis of the fluorescence radiation's behavior within layered samples, facilitating a deeper understanding of its transmission dynamics [70, 76, 91].

Before starting the calculation, it's crucial to highlight the significance of the complex refractive index for X-rays. This index delineates the degree to which wave propagation is influenced within a material, encapsulated by the formula:

$$n_j = 1 - \delta_j + i\beta_j \tag{2.7}$$

Where:

- n_j represents the complex refractive index for the atom j.
- δ_j and β_j are the real and imaginary components, respectively. These components elucidate the dispersive and absorptive dimensions of the wave-matter interaction, essential for understanding how X-rays are altered by the material.

These components can be derived from the atomic scattering factors (f_1 and f_2) using the relations:

$$\delta_j = \frac{n_a r_e \lambda^2}{2\pi} f_1 \tag{2.8}$$

$$\beta_j = \frac{n_a r_e \lambda^2}{2\pi} f_2 \tag{2.9}$$

Here, n_a denotes the Avogadro number, r_e is the classical electron radius, and λ is the wavelength of the emitted fluorescence radiation. The scattering factors f_1 and f_2 quantify the dispersive and absorptive properties of the medium j towards X-ray wavelengths, respectively.

The initial phase in modeling the angular intensity profiles involves the calculation of wavenumbers for the emitted fluorescence radiation, both in the air and within the sample layer at each angle [70, 76, 91]. These wavenumbers are determined as follows:

- For air, the wave number k_{air} is given by:

$$k_{air} = \frac{2\pi}{\lambda} \sin\theta \tag{2.10}$$

- For the medium j within the layer k_j, the wave number is calculated using:

$$k_j = \frac{2\pi}{\lambda} \sqrt{n_j^2 - \cos^2\theta} \tag{2.11}$$

The transmission coefficient (t_j^+) is essential for understanding how the field strength of emitted radiation changes as it transitions from the surface to the air [70, 76, 91]. It is derived using the Fresnel equation:

$$t_j^+ = \frac{k_{air}}{k_j} \frac{\sqrt{n_j^2 - \cos^2\theta}}{\sin\theta + \sqrt{n_j^2 - \cos^2\theta}} \tag{2.12}$$

Where:

- For term $\frac{k_{air}}{k_j}$ indicates the ratio of the wave number in air to that in the subsequent medium. This ratio significantly influences the amplitude of the transmitted wave.
- The second term adjusts the transmission coefficient based on the refractive index of the next medium and the angle of incidence. This adjustment considers both the geometric and optical properties at the interface.

This approach allows for the calculation of changes in the field strength of the emitted radiation as it transmits from the surface to the air. Understanding the transmission coefficient is crucial for accurately predicting how fluorescence radiation behaves as it encounters different media interfaces [70, 76, 91].

To quantify the attenuation of the fluorescence radiation's intensity within a layer, one can use the imaginary part of the complex refractive index [70, 76, 91]. This part involves figuring out how much electromagnetic radiation the medium is absorbing. The attenuation calculation is performed as follows:

$$\frac{1 - exp\left[-2Im(k_j)d_j)\right]}{2Im(k_j)} \tag{2.13}$$

Where:

- $Im(k_j)$ represents the imaginary part of the wave number (or wave vector component along the z-axis) for the j medium. The imaginary part of the wave number is related to the attenuation (or absorption) of the wave as it propagates through the medium. A wave number, k, in complex form can be written as $k = k' + ik''$, where $k'' = Im(k)$ signifies the rate of the exponential decay of the wave amplitude within the medium j.

- d_j represents the thickness (or depth) of the layer or medium through which the wave is propagating.

- $exp\left[-2Im(k_j)d_j)\right]$ term represents the attenuation factor of the wave as it travels a distance d_j within the medium. The exponential decay is characterized by the product of the imaginary part of the wave number and the distance traveled, multiplied by 2 to account for both the forward and backward (or round-trip) paths in some interpretations, such as in the analysis of reflection or transmission through a layer.

The function can be interpreted as calculating a quantity related to the attenuation of a wave due to its propagation through a medium of thickness d_j. The denominator, $2Im(k_j)$, normalizes this value, potentially to derive a quantity like an effective penetration depth or a related measure of how the wave's intensity is reduced within the medium.

For the final step in understanding how the intensity and phase of emitted fluorescence radiation are modified after undergoing multiple reflections within a layer before its exit, one can delve into the calculation of reflection coefficients at the interfaces between different media. These calculations are critical for determining the behavior of emitted radiation as it interacts with the boundaries of the layer and substrate [70, 76, 91].

The reflection coefficients at an interface between two media, considering the change in refractive index from one medium j to the next medium l, and incorporating the angle of incidence (θ). These coefficients are derived from the Fresnel equations for reflection at an interface and are adapted to account for oblique incidence (non-normal incidence) based on the refractive indices of the two media involved and the angle of incidence [70, 76, 91]. Let's break down each term for clarity:

- Reflection coefficient for emitted radiation back into medium j:

$$r_j^- = \frac{\sqrt{n_j^2 - \cos^2\theta} - \sin\theta}{\sqrt{n_j^2 - \cos^2\theta} + \sin\theta} \tag{2.14}$$

  This coefficient is used when considering the reflection of emitted radiation that is moving from medium j to air and then reflects into medium j.

- Reflection coefficient for emitted radiation from medium l back into medium j:

$$r_j^+ = \frac{\sqrt{n_j^2 - \cos^2\theta} - \sqrt{n_l^2 - \cos^2\theta}}{\sqrt{n_j^2 - \cos^2\theta} + \sqrt{n_l^2 - \cos^2\theta}} \tag{2.15}$$

  This coefficient is used when considering the reflection of emitted radiation that is moving from medium j to medium l and then reflects into medium j.

With these reflection coefficients, the intensity and phase variations of the emitted light after multiple reflections can be calculated using the following expression:

$$\frac{1 + \left|r_j^-\right|^2 exp\left[-2Im(k_j)d_j\right]}{\left|1 - r_j^+ r_j^- exp\left[2i(k_l)d_j\right]\right|^2} \tag{2.16}$$

The intensity of the emitted fluorescence radiation as a function of emission angle, $I(\theta)$, can be approximated by combining the transmission coefficient, attenuation factor, and the reflection:

$$I(\theta) \approx \left|t_j^+\right|^2 \frac{1 - exp\left[-2Im(k_j)d_j)\right]}{2Im(k_j)} \frac{1 + \left|r_j^-\right|^2 exp\left[-2Im(k_j)d_j\right]}{\left|1 - r_j^+ r_j^- exp\left[2i(k_l)d_j\right]\right|^2} \tag{2.17}$$

This formulation encapsulates the effect of multiple reflections on the emitted light's intensity and phase, integrating the impact of changes in medium, angle of incidence, and the layered structure of the sample [70, 76, 91].

Calculating the intensity as a function of the emission angle is crucial for determining the optimal experimental geometry. These calculations were employed to establish the appropriate distance between the sample and the detector. Initially, the angular intensity profile of metallic chromium (Cr) was calculated, followed by the profile of chromium dioxide (Cr_2O_3). By comparing these profiles, the shift between the two in milliradians could be determined. This information was then used to select the experimental geometry.

2.3.2 X-ray sources

GEXRF experiments can be conducted with various ionizing radiation sources, from conventional X-ray tubes in laboratory setups to synchrotron radiation facilities. While synchrotron sources offer unique advantages, their limited accessibility remains a notable limitation. In contrast, advancements in X-ray tube technology provide promising alternatives for broader application. This section highlights the comparative roles of X-ray tubes and synchrotron radiation within the GEXRF experimental setup.

2.3.2.1 X-ray tubes

X-ray tube technology's widespread application underscores its significance in material research in laboratories. The main components of X-ray tubes are the cathode and the anode. These components are housed in evacuated glass. The cathode is designed to emit thermal electrons when heated by a current supplied from an external power source. The anode is made of high-purity metals such as molybdenum, copper, or tungsten. It serves as a target for accelerated electrons and facilitates the generation of X-rays upon impact [92].

The operation begins with the heating of the cathode, leading to the emission of thermal electrons. These electrons are then accelerated toward the anode by a high voltage. Upon striking the anode, two types of radiation are produced: Bremsstrahlung and the characteristic radiation. These two types of radiation contribute to the X-ray spectrum emitted by the tube [92]. The generation of X-rays by means of X-ray tubes is illustrated in Figure 2.11.

The X-ray spectrum from a tube is characterized by a continuous component, known as Bremsstrahlung, and discrete characteristic lines that are specific to the anode material. Factors like the anode material and acceleration voltage play crucial roles in determining the characteristics of the emitted X-ray spectrum [92].

Only 1% of the electrical power can be converted to X-rays; the remaining is converted to heat. Given the substantial heat load on the anode, efficient cooling mechanisms are essential [92]. These can be achieved by water or oil circulation systems around anodes or the use of a rotating anode to spread the heat over a larger area. A novel solution is the liquid-metal-jet anode, which uses a continuously regenerated liquid metal as the anode material to mitigate thermal damage and enhance the efficiency and brightness of the X-ray source [93].

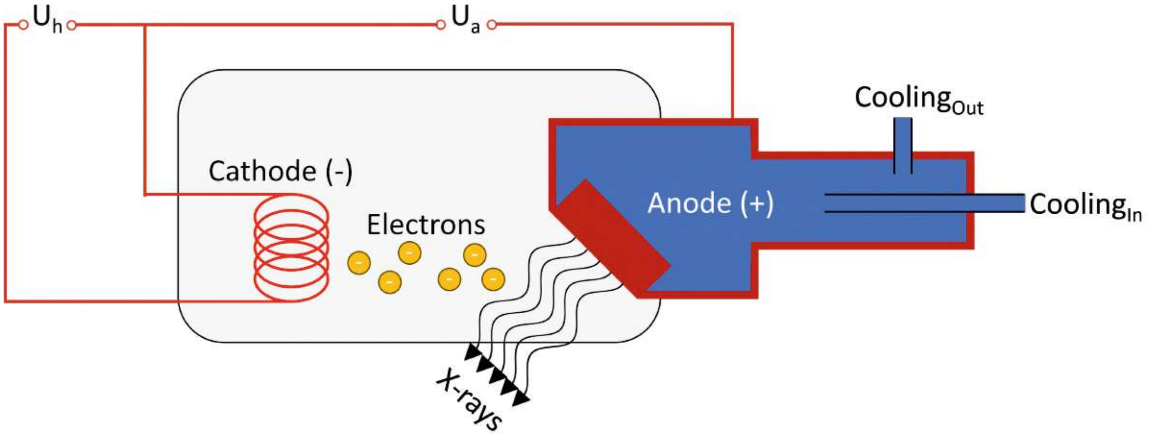

Fig. 2.11: A basic diagram of an X-ray tube, featuring both cathode and anode within a vacuum-sealed tube. The cathode's filament heats up, releasing electrons that are then propelled towards the anode by a high-voltage electric field. Upon colliding with the anode, X-rays are generated. To manage the resulting heat, cooling systems are applied to the anode.

Most of the applications of GEXRF were using a high power (P>1 kW) Rh or Mo anode X-ray tube, leading to long experiment times. The transition to more compact, low-power X-ray tubes (P<1 kW) in subsequent years, sometimes coupled with polycapillary lenses, highlighted the field's progression towards more versatile and accessible analytical tools [94].

2.3.2.2 Synchrotron sources

The historical background of synchrotron radiation began in 1940. When a charged particle radially accelerated at nearly the speed of light emits electromagnetic radiation, which is known as synchrotron radiation. It was first observed accidentally during experiments with early particle accelerators, known as synchrotrons, used to accelerate electrons to relativistic speeds. The phenomenon was initially seen as a problematic energy loss for the accelerators, causing unwanted electron deflection. But better understanding of this phenomenon led to the development of synchrotron light sources specifically designed to produce and use this radiation for scientific research, highlighting its transition from an undesired byproduct to a valuable research tool. Due to its unique properties, synchrotron radiation became an essential tool for research in various scientific fields [95].

In the 1960s and 1970s, the importance of synchrotron radiation for studying the structure and properties of matter was realized. The first dedicated synchrotron light sources were built to exploit this powerful and versatile form of electro-magnetic radiation. These early facilities paved the way for the advanced synchrotron radiation facilities available today, which offer highly collimated, intense, and tunable X-ray beams for a wide range of scientific and industrial applications [95].

The continuous improvement of synchrotron radiation is achieved by advancing in the design and construction of facilities, beamlines, and instrumentation.

Synchrotron radiation is generated through several steps. Initially, an electron source emits electrons, which are then accelerated to nearly the speed of light using a linear accelerator (LINAC). These electrons are further accelerated and synchronized in a booster ring to achieve their target energy level. Subsequently, they are injected into a storage ring, where they are maintained in a circular orbit by magnetic fields in an ultra-high vacuum environment. As electrons traverse through different magnetic devices, including bending magnets, undulators, and wigglers, they emit electromagnetic radiation, known as synchrotron radiation, ranging from infrared to hard X-rays. This radiation is directed to various experimental stations or beamlines for a wide range of research and analytical applications [61, 96]. A schematic representation of the synchrotron facilities is shown in Figure 2.12.

The journey of the ejected electrons starts in a linear accelerator. LINAC accelerates the electron very close to the speed of light. A LINAC consists of a series of radio frequency (RF) cavities, each providing an electric field that accelerates the electrons as they pass through. This phase of acceleration is critical, as it provides the initial boost needed to propel the electrons to high velocities. The efficiency of this process is important, as it sets the foundation for the subsequent stages of acceleration and the overall brightness and quality of the synchrotron radiation produced [61, 96].

After exiting the LINAC, the electrons are injected into a booster ring, a circular accelerator that further increases their energy. The booster ring uses magnetic fields to bend the electrons along a circular path. This stage is crucial for bringing the electrons up to the desired energy level before they are transferred to the main storage ring. The

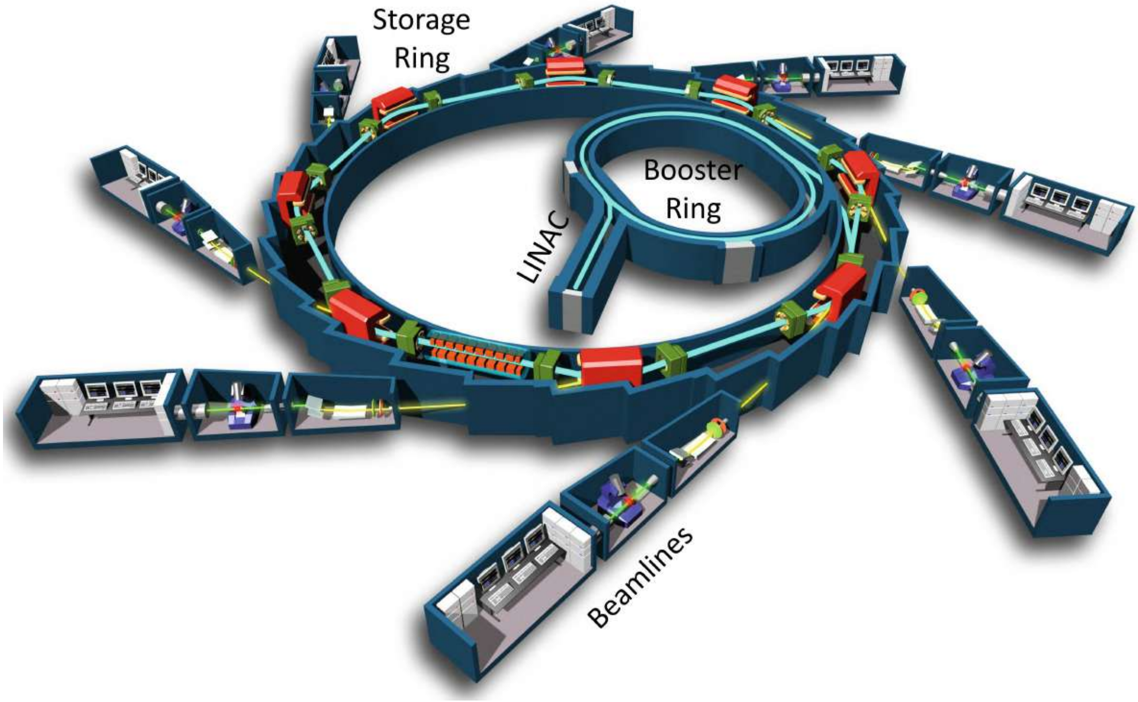

Fig. 2.12: General diagram of synchrotron facilities, adapted from [97]

booster ring serves not only to increase the energy of the electrons but also to pack them into tight bunches, optimizing the intensity and coherence of the radiation they will emit in the storage ring [61, 96].

The storage ring's primary function is to sustain the circular motion of electron bunches at relativistic speeds. Magnetic fields within the storage ring play an important role in controlling the path and dynamics of the electron beam. Bending magnets are responsible for keeping the electrons on their circular path. Quadrupole and sextupole magnets are responsible for the focusing of the beam. To ensure that the electrons remain tightly bundled, this configuration corrects for any spread in momentum and position. It is necessary to have precise control over the beam dynamics in order to get the best quality and intensity of synchrotron radiation [61, 96].

The change in direction of the electrons produced by the magnetic field results in the emission of synchrotron radiation. This radiation is characterized by its unique brightness and wide spectrum range. Based on the energy of the electrons and the configuration of the magnetic fields, the intensity and wavelength of the emitted radiation can be fine-tuned [61, 96].

Insertion devices are specialized magnets placed in straight sections of the storage ring to modify the trajectory of the electron beam and enhance the properties of the emitted synchrotron radiation. There are three main types of insertion devices: wavelength shifters, wigglers, and undulators, each serving distinct purposes [61, 96].

A wavelength shifter is designed to increase the energy of the synchrotron radiation. The direction of the electrons is changed by creating a strong magnetic field. As a result, the energy of the emitted radiation increases. This allows the generation of higher-energy photons, extending the synchrotron's capabilities for experiments requiring hard X-rays. The wavelength shifter comprises three magnetic poles: a powerful central pole generates synchrotron radiation, while two outer poles with a field opposing that of the central pole counteract the deflection of the electron beam path. By employing strong magnetic fields typically ranging from 5 to 10 Tesla, this setup results in a reduced radius of the electron's trajectory [61, 96].

Wigglers and undulators operate on a similar principle to wavelength shifters. However, instead of three poles, they use an N number of poles arranged in a periodic magnet structure with alternating magnetic fields. This arrangement force electrons to follow sinusoidal trajectories within the device. Similar to wavelength shifters, the outer poles are employed to counteract deflections in the electron beam trajectory, while all poles in between contribute to synchrotron radiation production [61, 96].

Wigglers are comprised of a sequence of magnets with alternating polarity, inducing electrons to oscillate or "wiggle" as they traverse through the device. This wiggling motion results in a broader spectrum of radiation with increased intensity, thereby generating a brighter beam. This enhancement is particularly beneficial for beamlines requiring high flux, significantly amplifying their capabilities [61, 96].

Undulators, similar to wigglers, have a series of alternating magnets, but the magnetic field strength and the spacing between magnets are designed such that the emitted radiation from consecutive oscillations interferes constructively. The result is highly coherent, very intense, and concentrated radiation in narrow energy bands. Undulators are essential for experiments requiring coherent beams [61, 96]. Principles of syncrotron radiation generation by various insertion devices are shown in Figure 2.13.

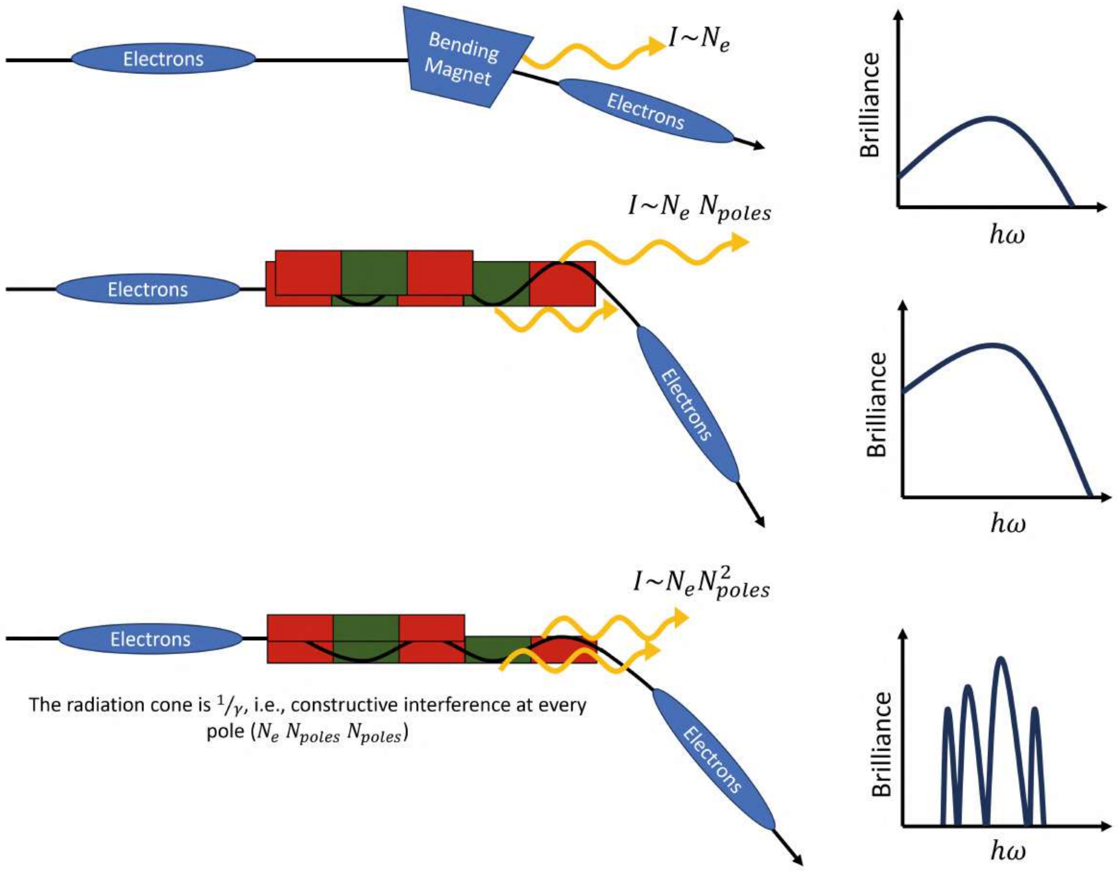

Fig. 2.13: The production of syncrotron radiation by bending magnets, wigglers, and undulators and the resulting energy spectra.

Beamlines are the channels through which synchrotron radiation is delivered from the storage ring to the experimental stations. Beamlines are designed to shape and refine the beam to meet the needs of specific experiments. Such customizable setups allow researchers to optimize the intensity, focus, and wavelength of the synchrotron radiation for their particular needs. After beamline optics, experimental instruments and detectors are positioned to measure the interaction between synchrotron radiation and matter.

The unique properties of synchrotron radiation provide researchers with opportunities to probe the microcosmic realms of matter. It is worth highlighting a few important features of synchrotron radiation that have had a major impact on the presented work.

- **High Brightness**

  At the heart of synchrotron radiation's appeal is its extraordinary brightness. This brilliance translates into an intense photon flux concentrated in a small, well-collimated beam. The implications for research are profound, as this high brightness ensures the availability of reduced experimental times and increases the sensitivity and resolution of experimental techniques such as GEXRF and GEXANES.

- **Broad Spectral Range**

  Synchrotron radiation covers a broad spectrum range that meets a great range of experimental requirements in several scientific disciplines. Researchers can study atomic structures, electronic states, and molecular dynamics using the same source, adjusting the wavelength to suit their specific requirements.

- **Tunable Energy**

  Another important characteristic feature of synchrotron radiation is its tunable energy. By adjusting the energy of the synchrotron radiation, it can be tailored to specific needs, such as the absorption edges of certain elements.

- **Small Source Size and Natural Collimation**

  Synchrotron radiation is emitted from a remarkably small source and exhibits natural collimation, resulting in a narrow, directed beam. This property is invaluable for performing experiments that require high spatial resolution and precision. The small, focused beam can be directed to specific areas of a sample, allowing localized analysis without affecting the surrounding material and also reducing the topographical effect on the experimental result.

2.3.3 Detection of fluorescence X-rays

In the field of X-ray fluorescence (XRF) analysis, the evolution of detector technologies is rapidly improving experimental setups. This section discusses two major types of detection strategies that have been used in GEXRF experimental setups. This includes energy dispersive detection and scan-free energy-dispersive detection methods.

2.3.3.1 Energy dispersive detection

In XRF analysis, silicon drift detectors (SDDs) have surpassed Si(Li) detection devices because they can resolve higher energies and produce less electronic noise. This is because they are better at picking up excited semiconductor current. Such an advancement is essential for GEXRF applications, facilitating the detailed discrimination of XRF signals from diverse elements. This capability allows researchers to capture the angular intensity profiles from different atoms simultaneously [94].

The scanning GEXRF experiment involves recording angular intensity profiles through detector movement. This movement can be either circular, centered on the sample to maintain a constant detection angle, or linear, moving perpendicular to the sample surface. Such methodologies allow for the sequential measurement of XRF radiation at varying grazing emission angles. The accuracy of these scanning measurements heavily relies on the precision and resolution of the positioning system for distinguishing features in the angular intensity profiles [94].

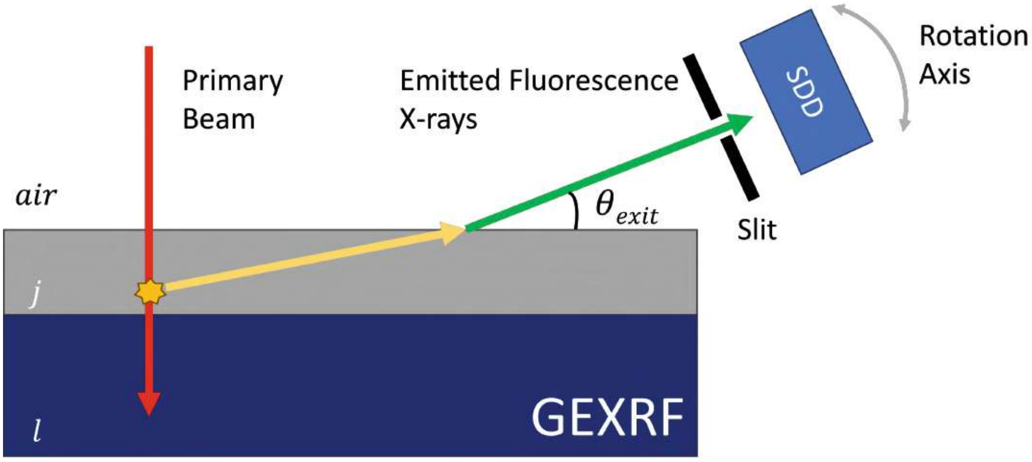

Fig. 2.14: Illustration of the detection of emitted fluorescence X-rays with energy dispersive detectors.

The required angular resolution varies depending on the XRF line energy and the characteristics of the sample, such as layer thickness in layered samples. However, the relatively large surface of SDDs poses a challenge to achieving the necessary angular resolution for GEXRF and requires the use of slits and a considerable distance between the sample and detector. These modifications, while crucial for enhancing angular resolution, unfortunately reduce the detection efficiency by decreasing the solid angle of detection and extending the experiment durations. This limitation has impacted the broader application of GEXRF [94]. A schematic representation of the GEXRF setup with energy dispersive detection is shown in Figure 2.14.

2.3.3.2 Scanning-free detection

In 1993 ([98]), Sasaki et al. did important work that made GEXRF possible by showing that angular intensity profiles could be recorded without moving the detector. They show that by using image plates, it is possible to measure the angular intensity profiles. This experiment aimed at detecting K_α fluorescence line from a Zn monoatomic layer on an Au substrate. Results show the clear visibility of interferences in the GEXRF signal. For quantitative analysis, however, more scanning with an energy-dispersive Ge detector was needed, which showed early problems with making measurements that didn't require scanning [94].

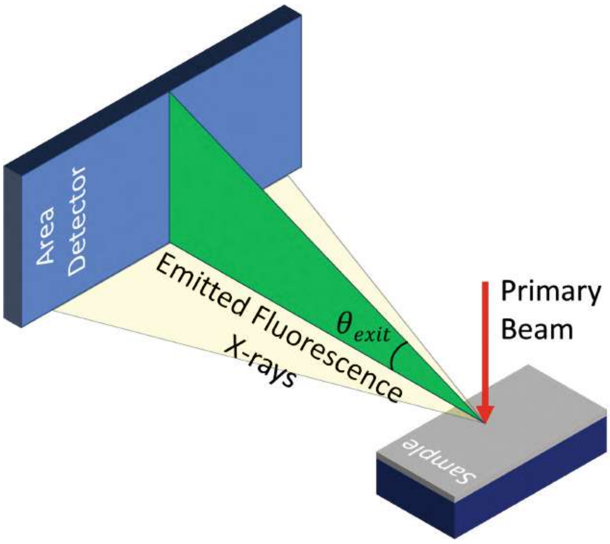

Fig. 2.15: Illustration of the detection of emitted fluorescent X-rays with a scan-free approach using an area detector.

Recent advancements have greatly improved the functionality of GEXRF using area-sensitive detectors, which outperform imaging plates in sensitivity and signal-to-noise ratio. Notably, detectors like the pnCCD are particularly effective for scan-free GEXRF. The pnCCD offers an optimal combination of pixel size, energy resolution, and frame rate for various X-ray applications [94].

The setup for scan-free GEXRF with an area-sensitive detector is illustrated in Figure 2.15.

2.4 X-ray absorption fine structure (XAFS) spectroscopy

X-ray absorption fine structure (XAFS) spectroscopy deals with changes in the absorption from an incident X-ray beam, depending on the energy and composition of the material. Specifically, XAFS refers to the modulation of an atom's X-ray absorption probability because of the atom's atomic and electronic structure. XAFS can provide detailed information about the chemical state, local symmetry, local atomic environment, and interatomic distances of samples regardless of their physical state [99–101].

There are two main parts to an XAFS spectrum: XANES (X-ray Absorption Near Edge Structure) and EXAFS (Extended X-ray Absorption Fine Structure) (see in Figure 2.16). Each provides different insights into the material's properties, enabling comprehensive characterization.

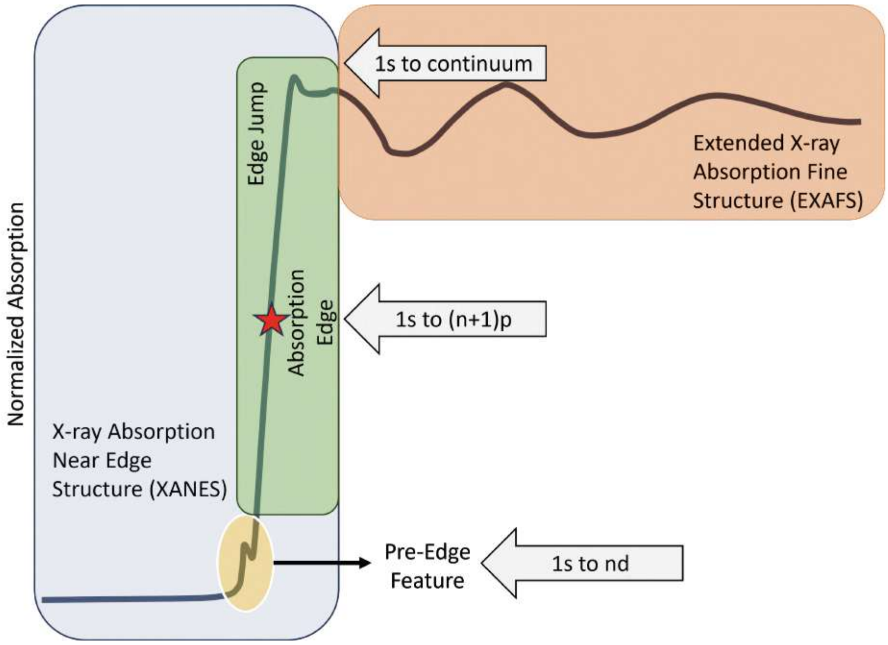

Fig. 2.16: Regions of XAFS spectrum

XANES shows details about the sample's electronic structure, such as its oxidation states and the atom's local coordination environment [99–101]. EXAFS extends the analysis by examining the interference pattern created by the scattering of the ejected photoelectrons off surrounding atoms. This technique can determine distances to nearest neighbors, coordination numbers, and identify neighboring atomic species, offering a detailed picture of the local atomic environment [99–101].

XAFS experiments can be conducted using two principal methods: transmission mode and fluorescence mode. Each method has its own specific experimental setup, advantages, and considerations, making them suited for different types of samples and research questions.

Transmission mode is the traditional approach to conducting XAFS experiments. In transmission mode, the intensity of the primary X-ray beam is measured before and after it passes through the sample. This method fundamentally relies on precisely tracking how much X-rays weaken as they move through a material. This reveals how the material absorbs X-rays at different energy levels. The experimental apparatus typically involves two ionization chambers placed before (I_0) and after (I) the sample. These chambers measure the intensity of the incoming and transmitted X-rays, respectively. This approach provides a direct measurement of the absorption of primary beam by sample as a function of X-ray energy and providing insights into the electronic structure and bonding environment of the atoms within the sample. The quality of the data obtained in transmission mode heavily depends on the sample's preparation. The sample must be homogeneous and thin enough to allow a significant portion of the X-rays to pass through without being completely absorbed. The ideal sample thickness varies depending on the material's absorption properties [102].

Fluorescence mode is particularly useful for samples unsuitable for transmission measurements. In this method, the experiment focuses on detecting the emitted fluorescence radiation by the sample when it is excited by a primary X-ray beam [99–101]. By drawing the variation of the interested emission line in the XRF spectrum as a function of the incident energy, an absorption spectrum can be obtained. The setup for fluorescence measurements often includes energy-dispersive detectors, such as silicon drift detectors

(SDD) or charged coupled devices (CCD), positioned to capture the emitted fluorescence radiation.

In fluorescence mode, self-absorption effects must be taken into account. Here, fluorescent X-rays are reabsorbed within the sample and can significantly affect the accuracy of the experiment, especially for high Z (atomic number) elements. To mitigate this, special geometries can be used that minimize the path length of the fluorescent X-rays through the sample, thereby reducing the self-absorption effect. Another solution is mathematical correction. The data can be corrected to account for self-absorption, but this requires accurate knowledge of the sample composition and geometry [99–101].

In the atomic model, electrons are arranged in shells around the nucleus, with each shell corresponding to a principal quantum number (n). These shells are further divided into subshells characterized by the azimuthal quantum number (l), which determines the shape of the electron's orbital. The interaction of X-rays with an atom primarily involves inner-shell electrons, leading to specific absorption phenomena known as absorption edges [100].

The absorption edge is a threshold at which an X-ray photon has sufficient energy to eject an electron from an inner shell, creating an electron vacancy. This process is highly dependent on the electron configuration of the atom, as different shells and sub-shells have distinct binding energies. The ionization of an electron from the $n = 1$ shell which corresponds to the K-edge. The L- and M-edges relate to the ionization of electrons from the $n = 2$ and $n = 3$ shells, respectively. The energy of the absorption edge provides valuable information about the electronic structure and chemical state of the atom [100].

The theoretical analysis of XAFS spectra involves understanding the transition probability of electrons between different states or the above-mentioned shells, which is influenced by the selection rules of quantum mechanics. The allowed electronic transitions between the energy levels of the hydrogen atom are shown in Figure 2.17. This diagram, also known as the Grotrian diagram, shows that only transitions between adjacent columns are allowed according to the $\Delta\ell = \pm 1$ selection rule. XANES provides insights into the electronic structure and chemical bonding of materials. XANES focuses on the energy region just at and above the core-level absorption edge. This region is sensitive to the unoccupied electronic states and can reveal information about the valence state, coordination chemistry, and the local symmetry of the absorbing atom [100].

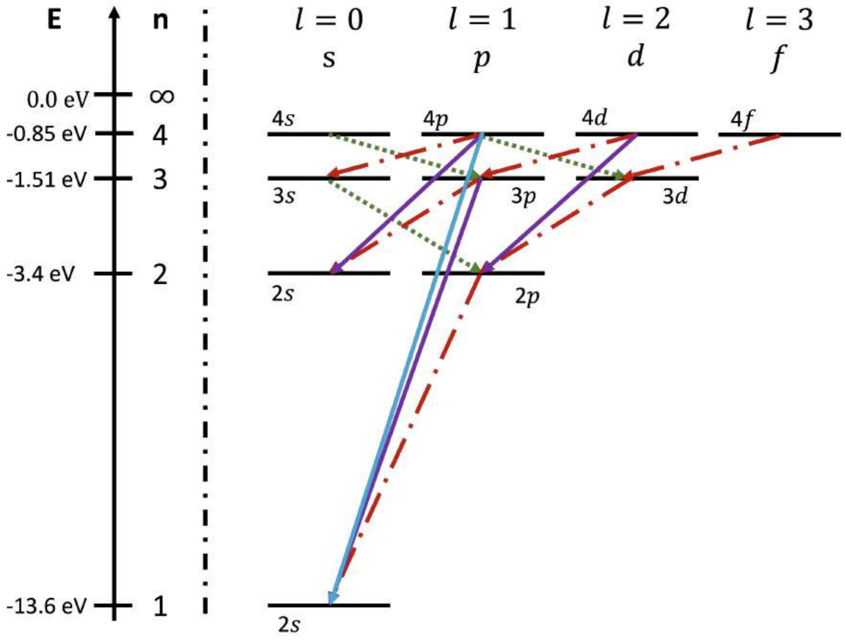

Fig. 2.17: The transition probabilities of the electron in the hydrogen atom, shown in the Grotrian diagram.

The XANES region is characterized by several key features:

- **Pre-edge features**, which may arise from transitions to bound states or hybridized orbitals and can provide information about the local geometry and electronic structure.
- **The absorption edge**, indicating the energy required to excite a core electron to the lowest unoccupied electronic state.
- **The edge jump**, reflecting the increase in absorption coefficient as the energy crosses the threshold for core-level electron excitation to continuum states.

Analysis of XANES data involves several steps:

- **Normalization:** The raw absorption spectrum is normalized to isolate the XANES features by removing the overall trend and scaling the edge jump to a standard value. This facilitates comparison between different spectra.

- **Extraction of Chemical Information:** By examining the energy position and shape of the absorption edge and pre-edge features, researchers can deduce the oxidation state and coordination environment of the absorbing atom. Shifts in the edge position can indicate changes in valence state, while the intensity and splitting of pre-edge peaks can provide insights into the local symmetry and electronic structure.
- **Comparison with Standards:** Often, the spectra of known compounds with similar chemical environments are used as references to help interpret the XANES features of a sample. This comparative approach can be particularly useful for identifying oxidation states and coordination geometries.

Feature	XANES	EXAFS
Region of Spectrum	Near the absorption edge	Beyond the absorption edge
Energy Range	Within a few tens of eV above and below the absorption edge	From just above the edge to several hundred eV beyond the edge
Information Provided	Chemical state, oxidation state, local symmetry	Local atomic environment, interatomic distances, disorder
Sensitivity	Sensitive to the electronic structure	Sensitive to the atomic structure

Tab. 2.1: Comparison of EXAFS and XANES detailing the region of spectrum, energy range, information and sensitivity

2.5 Active learning

Active learning, also known as "query learning" in statistics, is a transformative approach within the machine learning and artificial intelligence domains. This methodology diverges from traditional supervised learning by introducing a dynamic, selective process for data acquisition. Instead of passively learning from a predetermined set of labeled data, active learning enables algorithms to actively choose their training data. This strategy is predicated on the hypothesis that a model can perform better and learn more efficiently if it focuses on the most informative data points, effectively being "curious" about the data from which it learns [103].

In machine learning, data is called a "label" when it serves as the target or output value that a model aims to predict. Labels provide the correct answers for each input data point, making them essential in guiding a model's learning process. For example, in image classification tasks, the label might describe what is depicted in the image, such as "dog" or "cat."

In traditional supervised learning, large data sets with predefined labels are used to train the model. The goal is to learn the correlations between inputs and outputs. This method, while straightforward, often faces practical challenges, notably the availability of labeled data. Labeling extensive datasets is not only time-consuming but also costly, especially in fields requiring expert knowledge for accurate annotation [104].

Active learning presents a solution by introducing a model that is not a passive recipient but an active participant in its learning process. This paradigm shift allows the model to achieve greater accuracy with fewer training labels by selectively choosing the data points from which to learn. The essence of active learning lies in its ability to operate efficiently in scenarios where there is an abundance of unlabeled data but where labeled data is either scarce or too expensive to acquire [104, 105].

In active learning, labels are requested more selectively. The model identifies specific, informative data points and queries their labels or values, prioritizing the most uncertain or difficult examples. This approach enables the model to learn effectively with fewer labeled data points, reducing the overall cost and effort of labeling. The active learning algorithm focuses on querying labels at data points that are likely to provide the most value for the model's learning process. The ultimate goal is to minimize the need for labeled data while maximizing the model's performance and reducing labeling efforts and resources [103–105].

This dynamic approach to acquiring labels is a defining feature of active learning, enabling a model to achieve high accuracy with minimal labeling effort.

Active learning's versatility has led to its application across various domains, where precision and labeling costs are critical concerns. In these fields, active learning facilitates the development of robust models fine-tuned to the data's most informative aspects [103–105].

The active learning process evolves in three important steps:

- **Initialization**

  The active learning process begins with initial model training, which is performed on a relatively small set of labeled data. This preliminary model serves as a starting point to establish a basic understanding of the task. Despite its limited initial knowledge, this model can make initial predictions and identify gaps in its learning.

- **Query for Information**

  Once the initial model is created, the next step is for it to identify which data points in the unlabeled data set would be most informative for further training. This stage is critical and involves the model "querying" for information. The model evaluates the unlabeled data and selects specific instances where it predicts its performance could be significantly improved if those instances were labeled. The criteria for selecting these data points vary depending on the active learning strategy employed. Common strategies include uncertainty sampling, where the model queries the data points about which it is most uncertain, and query by committee, where multiple models (or a committee) are used and the data points with the most disagreement are queried.

- **Update the Model**

  Once the informative data points have been identified, the model is updated with this new information. This step involves retraining or fine-tuning the model to incorporate the newly acquired knowledge. The updated model now has a better understanding of the data and makes more accurate predictions.

The cycle then begins again with the query phase, where the improved model searches for new data points to label [105]. This iterative cycle continues, with each query and update phase incrementally improving the model toward superior accuracy and functionality. The process is designed to continue until a predetermined performance benchmark is reached or a certain number of cycles are completed [106].

What makes active learning unique is its dynamic nature, which allows the model to progressively refine and adapt itself by focusing its learning on the most complex or insightful segments of the data [106]. This methodology ensures efficient allocation of scarce labeling resources, facilitating the creation of robust models in situations where labeling the entire dataset is impractical or impossible [107].

The success of active learning depends heavily on the diversity and size of the unlabeled data pool, which significantly affects the efficiency of the algorithm. A diverse data pool ensures exposure to a large number of data points, which improves generalization capabilities. Conversely, a larger data pool increases the model's potential for improvement over time [105].

In pool-based active learning, the algorithm strategically selects data samples from a reservoir of unlabeled information based on specific labeling criteria. This approach maximizes the efficient use of limited labeling resources by prioritizing data that, once labeled, will significantly improve model performance. The diversity of this data pool is critical to ensuring more productive learning [105].

Active learning strategies play an important role in enhancing the efficiency of the learning process by identifying and selecting the most informative data points for labeling. These strategies are crucial because they pinpoint the instances that will contribute most significantly to the model's learning. Below is an outline and a detailed description of some of the key query strategies commonly used in active learning.

- **Uncertainty Sampling**

  In uncertainty sampling, the model focuses on querying instances about which it is least confident. The rationale behind this strategy is straightforward: by learning from the most uncertain cases, the model can quickly gain new insights and reduce its overall uncertainty. For example, in a classification task, the model might focus on instances where it is unable to clearly distinguish between two or more classes [108].

  Advantages:

  - Quick identification of informative examples.
  - Simple to implement and understand.

Limitations:

  - May lead to the selection of outliers or noise.
  - Can be biased towards densely populated regions of the feature space.

- **Query by Committee**

  Query by committee (QBC) involves maintaining multiple models (the committee) that are trained on the same dataset. The instances about which the committee members disagree the most are considered the most informative and are selected for labeling. This disagreement is a measure of uncertainty, and querying these instances helps in refining the model by focusing on the most contentious points [109].

  Advantages:

  - Incorporates multiple perspectives, reducing the risk of selecting outliers.
  - Effective in reducing model variance.

  Limitations:

  - More computationally intensive due to maintaining multiple models.
  - May not be as effective in cases where models converge to similar hypotheses.

- **Expected Model Change**

  This strategy focuses on selecting instances that, if labeled, are expected to induce the most significant change in the current model. The idea is to choose instances that will lead to the greatest improvement in the model. This strategy often involves a more complex computation to predict the impact of adding each instance to the training set, but it can be highly effective in rapidly improving the model [110].

  Advantages:

  - Focuses on the most impactful data points.
  - Can lead to rapid improvements in model performance.

  Limitations:

  - Computationally expensive, as it requires estimating the impact of each instance on the model.

  - May not always select diverse instances.

- **Expected Error Reduction**

  In this approach, the instances are chosen based on their expected contribution to reducing the overall error of the model. This strategy aims to select instances that will not only improve the model but also enhance its generalization capabilities. By focusing on reducing the error, this strategy can be particularly useful in applications where precision is critical [111].

  Advantages:

  - Directly targets error reduction, improving model accuracy.
  - Aligns closely with the ultimate goal of many learning tasks.

  Limitations:

  - Requires estimating the model's future performance, which can be challenging and resource-intensive.
  - May not be suitable for all models or problem types due to the complexity of error estimation.

Each strategy brings unique advantages, tailored to diverse problem sets and data environments. The choice among these strategies is dictated by the learning task's unique goals, the data's nature, and any existing constraints within the learning environment.

Active learning, characterized by its tactical data selection for labeling, presents a paradigm shift from conventional supervised learning, offering numerous benefits while also posing some challenges. Below are refined and polished insights into the advantages and disadvantages of active learning.

Advantages:

- **Efficient Use of Data:** One of the most significant advantages of active learning is its ability to achieve high model performance with fewer labeled instances. This is particularly beneficial in scenarios where data labeling is costly or time-consuming.

- **Cost-Effectiveness:** By reducing the number of samples that need labeling, active learning can significantly cut down the costs associated with data annotation, especially in fields requiring expert knowledge.
- **Improved Model Performance:** Active learning can lead to more accurate models as it focuses on the most informative data. This targeted approach can enhance the learning process, resulting in improved model performance.
- **Usefulness in Sparse Data Contexts:** In situations where unlabeled data is plentiful but labeled data is scarce, active learning becomes an invaluable tool. It allows for the efficient utilization of available labeled data.

Disadvantages:

- **Dependency on Interactive Labeling:** Active learning requires the ability to interactively query for labels. This is not always feasible, especially in scenarios where immediate feedback from an expert is not available.
- **Strategy-Specific Effectiveness:** The success of active learning heavily depends on the chosen query strategy. Not all strategies work equally well across different problems and datasets, which can affect the overall effectiveness of the approach.
- **Potential for Bias:** If the initial set of labeled data is not representative of the overall dataset, there's a risk of biasing the model. This can happen if the model continuously queries for similar types of data, leading to a lack of diversity in the training set.
- **Complexity in Implementation:** Implementing active learning algorithms, especially with more sophisticated querying strategies, can be more complex than standard supervised learning algorithms. This complexity might pose challenges in terms of development and computational resources.

While active learning offers a promising approach to dealing with the challenges of data labeling, it requires careful consideration of the strategies used and the context in which it is applied. Its advantages in reducing labeling costs and improving model performance must be weighed against the potential difficulties in implementation and the need for interactive labeling processes.

2.5.1 Bayesian Optimization

In this study, Bayesian optimization (BO) is used as an active learning process, exemplifying a pool-based active learning algorithm that adeptly employs various query strategies for effective sampling. BO, which is a probabilistic framework, employs Gaussian process (GP) models for the optimization of functions that are considered "black-box" and may be linked to expensive objectives, with the integration of noise. These objectives typically carry high evaluation costs, whether it is time, computational resources, or other types of expense, such as long synchrotron radiation experiments [112]. The GP models form an important part of BO, creating a framework to understand the relationship between a system's inputs and outputs based on a pool of training samples.

This relationship is depicted through a GP, which is a probability distribution over functions. It is denoted as:

$$\mathcal{GP}(\boldsymbol{\mu}(\mathbf{x}), \boldsymbol{\Sigma}(\mathbf{x})),$$

where:

- $\boldsymbol{\mu}(\mathbf{x})$ is the mean function, which provides the expected value of the function at input $\mathbf{x}$,
- $\boldsymbol{\Sigma}(\mathbf{x})$ is the covariance function, specifying the covariance between the function values.

.

Such a representation allows us to make informed predictions about system output in the face of new inputs while also quantifying the associated uncertainty. A GP can be conceptualized as an endless collection of Gaussian probability distributions, with each distribution employed to represent the subtleties of functions [113].

Gaussian Process Regression (GPR) refers to the application of a GP for regression tasks and involves setting up a prior distribution over possible functions, denoted as

$f(\mathbf{x}) \sim \mathcal{GP}(\boldsymbol{\mu}(\mathbf{x}), \boldsymbol{\Sigma})$. This reflects the researcher's expectations about the functions that most likely characterize the system or process of interest. Typically, this prior distribution is Gaussian, with mean and covariance functions driven by assumptions about the underlying function. Post-data collection, Bayes' theorem is applied to revise beliefs about the function $f(\mathbf{x})$. To put it in specific terms, the posterior distribution $p(f(\mathbf{x})|\mathcal{D})$ over functions $f(\mathbf{x})$ is calculated by combining the prior distribution $p(f(\mathbf{x}))$ with the likelihood $p(\mathcal{D}|f(\mathbf{x}))$ of the observed data $\mathcal{D}$, given the function $f(\mathbf{x})$. This combination is done using Bayes' theorem:

$$p(f(\mathbf{x})|\mathcal{D}) \propto p(f(\mathbf{x})) \times p(\mathcal{D}|f(\mathbf{x})) \tag{2.18}$$

To construct a GP model, a prior distribution over function values $f(\mathbf{x})$ at the input points $\mathcal{D}$ needs to be determined. This usually involves the assumption that $f(\mathbf{x})$ is drawn from a zero-mean Gaussian distribution with a covariance matrix $\mathbf{K}$. Similarly, the likelihood of the observed data, given the function $f(\mathbf{x})$, is generally assumed to be a Gaussian distribution with mean $f(\mathbf{x})$ and a noise parameter σ^2. The posterior distribution can then be estimated as follows:

$$p(f(\mathbf{x})|\mathcal{D}) \propto \mathcal{N}(0, \mathbf{K}) \times \mathcal{N}(\mathcal{D}|f(\mathbf{x}), \sigma^2\mathbf{I}) \tag{2.19}$$

Here, $\mathcal{N}$ signifies the normal distribution of probability density function (PDF). The multiplication of normal distribution of the PDFs of the prior and likelihood functions, both normal distributions, yield another normal distribution—denoted as the posterior distribution. The mean and variance of this posterior distribution can be computed using the following equations:

$$\boldsymbol{\mu}(\mathbf{x}) = \mathbf{K}(\mathbf{X}^*, \mathbf{X})(\mathbf{K}(\mathbf{X}, \mathbf{X}) + \sigma^2\mathbf{I})^{-1}\mathbf{y} \tag{2.20}$$

$$\boldsymbol{\Sigma}(\mathbf{x}) = \mathbf{K}(\mathbf{X}^*, \mathbf{X}^*) - \mathbf{K}(\mathbf{X}^*, \mathbf{X})(\mathbf{K}(\mathbf{X}, \mathbf{X}) + \sigma^2\mathbf{I})^{-1}\mathbf{K}(\mathbf{X}^*, \mathbf{X})^T \tag{2.21}$$

Within this context, if there are n training points and n^* testing points, $K(\mathbf{X}, \mathbf{X}^*)$ represents the $n \times n^*$ matrix containing covariances evaluated for all combinations of training and testing points and similarly for the other entries $\mathbf{K}(\mathbf{X},\mathbf{X})$, $\mathbf{K}(\mathbf{X}^*,\mathbf{X}^*)$, $\mathbf{K}(\mathbf{X}^*,\mathbf{X})$. Furthermore, σ^2 denotes the observation noise variance, $\mathbf{I}$ is the identity matrix, and $\mathbf{y}$ is the vector of observed target values corresponding to the training points $\mathbf{X}$.

The kernel function is a core component of the GP, which measures how similar two points are in the data set. This helps build the covariance matrix $K(\mathbf{X},\mathbf{X})$, a collection of covariances between all training data pairs, and plays a part in creating covariance vectors for training and testing data points.

The Matérn kernel is commonly used by GP to model a wide range of data relationships. It is flexible, able to track both stable, smooth functions as well as sudden changes and gaps. However, depending on the problem and data, other kernels may work better in different scenarios. The Matérn kernel, which is an extension of the Radial Basis Function (RBF) kernel, has an extra hyperparameter, ν, that manages the smoothness of the resulting function. A smaller ν leads to a less smooth approximation, while a larger ν makes the kernel behave like the RBF kernel.

Specifically, for XANES analysis, the Matérn kernel with $\nu = 1.5$ is very effective in describing the link between input and output variables. This kernel's ability to accurately predict optimal measurement points helps reduce the duration of the experiment. The Matérn kernel is also capable of handling data noise and irregular patterns, common in XANES analysis. The Matérn kernel includes another hyperparameter, the length scale, which decides how much neighboring points influence each other. The Maximum Likelihood Estimation (MLE) method is used to optimize these hyperparameters, striking a balance between fitting the data well and avoiding overfitting and thereby improving prediction accuracy. Accurate predictions, even with data noise, are crucial to minimizing the time spent on XANES experiments and obtaining accurate results.

The first step in the BO process is to find a new measurement point by using the mean (Eq. 2.20) and variance (Eq. 2.21) functions, which are important parts of making acquisition functions. In this investigation, we employed the Upper Confidence Bound (UCB) sampling function to iteratively determine the subsequent sample points and optimize the objective function. The UCB, a popularly employed acquisition function in BO, balances exploration and exploitation to efficiently probe unexplored regions within the input space. The forthcoming sample point is selected by maximizing the UCB function. The following equation represents the UCB acquisition function:

$$\mathrm{UCB}(\mathbf{x}) = \boldsymbol{\mu}(\mathbf{x}) + \kappa \times \boldsymbol{\Sigma}(\mathbf{x}) \tag{2.22}$$

In BO, the equilibrium between exploitation ($\boldsymbol{\mu}(\mathbf{x})$) and exploration ($\boldsymbol{\Sigma}(\mathbf{x})$) is maintained by factoring the variance function with a trade-off parameter (κ). The variance function's impact on the UCB function is directly proportional to the trade-off factor, which remains consistent throughout the optimization process. Nevertheless, as the sample size increases, the values derived from the variance function decrease due to the reduction in model uncertainty. This leads to an increased emphasis on the exploitation of the learned model, while the focus on exploration diminishes. The variance function could be used directly as a utility function to guess the next calculation points in maximum exploration mode, but this could mean that pre-peaks are missed, which happens a lot in XANES analyses. To circumvent this issue, we use the UCB function to calculate the next point instead of solely relying on the maximum of the variance function.

To summarize, GPR uses multiple Gaussian processes (GPs) to simulate a black-box function. Based on observed data, it iteratively updates the mean and covariance functions using Bayes' theorem. Theoretically, Euclidean distance can be used to correlate the sampling points in order to generate the covariance function. However, because of its versatility in managing data with different degrees of noise and smoothness, the Matérn kernel—a generalization of the Radial Basis Function (RBF) kernel—is employed in this study. Acquisition functions, which balance exploration and exploitation by using the mean and covariance predictions from the GP model, are used to predict new sampling point.

For a more comprehensive understanding of BO and GP, the following seminal works are recommended: ”Bayesian Optimization” by Garnett (2023) [114] and ”Gaussian Processes for Machine Learning” by Rasmussen et al. (2006) [115]. These resources offer a deeper exploration of the concepts, methodologies, and applications of these techniques, which facilitates a more thorough grasp of the material discussed in this text.

Chapter 3

Experimental Setup

The experimental setup detailed in the following sections includes the introduction of BESSY II and the μspot beamline, the specific geometrical arrangements employed, and the advantages of using the pnCCD detector in GEXANES applications. Additionally, the optimization of this setup through Bayesian optimization (BO) is discussed, showcasing how this method fine-tuned the experimental conditions for better accuracy. The document concludes with information on the samples selected for the case study, emphasizing the practical applications of the setup.

3.1 BESSY II

In the field of synchrotron radiation research, BESSY II is an important facility for X-ray-based analysis. BESSY II is located at the Helmholtz Center Berlin in Germany. It produces X-rays in a wide range of energies, enabling ground-breaking experiments and research in a variety of scientific disciplines.

BESSY II is a third-generation electron storage ring designed specifically to produce synchrotron radiation. It has a 240-meter circumference and houses a magnetic structure consisting of 32 bending magnets that hold the electrons in their orbits. These electrons reach 1.7 GeV with a nominal beam current of 300 mA. Since its opening in 1999, BESSY II has played a major role in synchrotron radiation research.

Since 2012, BESSY II has been operating in a "top-up" mode by injecting electrons every 90 to 120 seconds, allowing a constant flux over 24 hours, a significant improvement compared to the previous eight-hour intervals (decay mode). In addition to this continuous photon flux, the average photon flux has increased compared to the decay mode. The standard fill pattern at BESSY II is a multi-bunch hybrid pattern. The electrons, moving at a frequency of 1.25 MHz, complete the 240-meter circumference of the ring in 800 ns. This pattern consists of about 300 electron bunches, each with a length of 45 ps (or 0.0135 m) (FWHM), supplemented by a longer intense bunch and seven slicing bunches. These configurations are adaptable to different experimental needs, including time-resolved measurements. Special operating modes, such as single-bunch and low alpha modes, have been introduced to meet specific experimental requirements. In single-bunch mode, for example, only one bunch of electrons circulates in the ring. Although this mode operates with a beam current of only 13 mA, it is particularly suitable for time-resolved measurements and certain experiments where high photon flux is not essential. The low alpha mode also lets electrons be spread out more evenly, which leads to shorter photon pulse lengths and better coherence [116, 117].

BESSY II is equipped with 50 experimental stations to meet a wide range of research needs [118]. While most of these stations are primarily focused on the soft X-ray range (below 1 keV to around 15 keV), specific beamlines such as BAMline and µspot extend the facility's capabilities into the medium and hard X-ray ranges through the use of the wavelength shifter (WLS) as an insertion device [119, 120].

The BAMline [21] and μspot [121, 122] beamlines are multi-purpose beamlines. There are no dedicated terminal stations. Instead, several experiments can be realized using either a single method or a combination of several methods (multimodal). The following techniques and methods are available at the BAMline and μspot beamlines:

- **BAMline**: X-ray fluorescence spectroscopy (XRF), X-ray absorption spectroscopy (XAS); X-ray computed tomography (CT), X-ray Refractometry (XRR)
- **μspot**: X-ray diffraction (XRD), small/wide-angle X-ray scattering (SAXS/WAXS), XRF

3.1.1 μSpot beamline

The GEXANES experiments were performed on the μSpot beamline. This beamline is designed to provide a micro-focused X-ray beam with high spatial resolution (micrometres) together with high flux (10^{11}-10^{12} p/s), making it an ideal tool for photon-hungry experiments. μSpot beamline was established in 2004 as a collaboration between the Max Planck Institute of Colloids and Interfaces (MPIKG) Golm, the Technical University of Berlin (TUB), and the Federal Institute for Materials Research and Testing (BAM). The beamline is designed to allow different X-ray analytical methods to be performed with the small spot size. The beam focus varies between 1.5 and 100 µm, depending on the method to be used [121]. Examples of these methods include fluorescence imaging, powder diffraction, elastic scattering, reflectivity, small and wide-angle x-ray scattering (W-SAXS), and reflectometry.

The beamline source is a 7 T wavelength shifter (WLS), equipped with a toroidal mirror, and three monochromator elements: a double multilayer monochromator (DMM), a double crystal monochromator (DCM) with Si [111] arrangement, and a DCM with Si [311] arrangement. These components are all housed within the optical hutch. The toroidal mirror plays a vital role in this configuration, significantly enhancing photon flux compared to the BAMline. This increase in photon flux is a primary factor in the selection of this specific beamline.

In collaboration with BESSY-II, the Budker Institute of Nuclear Physics has designed, fabricated, and tested a superconducting 3-pole wavelength shifter (WLS) capable of generating a maximum magnetic field of 7 T at its central pole. The superconducting 7 T magnet, positioned at the center of the "non-dispersive" straight section, serves as the core component of the WLS. In addition to the superconducting magnet, two normal conducting correction magnets are located at the ends of the straight section, creating a compensated orbit deviation to ensure that the radiation point remains fixed at the center of the WLS. The magnetic field distribution and the electron beam trajectory along the WLS straight line are shown in Figure 3.1. The initial cryostat had a consumption of 3 liters of liquid helium per hour and had a single copper thermal screen cooled by liquid nitrogen. For an electron energy of 1.9 GeV and a field strength of 7 T, the maximum angular deviation and orbital displacement inside the WLS are 65 mrad and 15.5 mm, respectively [123, 124].

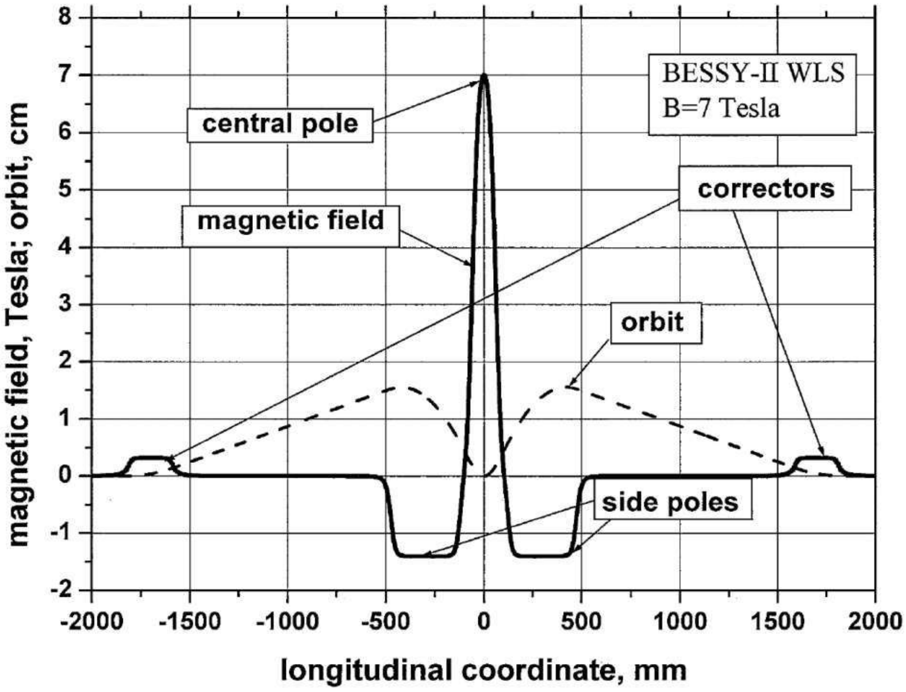

Fig. 3.1: Magnetic field distribution and electron beam orbit deviation throughout the 7 T BESSY-II WLS straight section. Adapted from Borovikov et al. [123]

The beamline configuration shown in Figure 3.2 illustrates the arrangement of the optical elements. The source, focused on the sample by a toroidal mirror, shown as M1 (cylinder with a bend), performs the task of vertically collimating the beam. M1 is located in the front-end system, 13 meters from the source. A double crystal monochromator (DCM) or double multilayer monochromator (DMM) is located 28.5 meters from the source. Using ultra-high vacuum windowless technology, the beamline is isolated from the experiment by two differently pumped Kapton windows [125].

The μSpot beamline monochromator uses two sets of crystal monochromators: Si (111) with $\lambda/\Delta\lambda$ around 5,000 and Si(311) with $\lambda/\Delta\lambda$ around 10,000. There is also a double multilayer mirror with a Mo/B4C coating where $\lambda/\Delta\lambda$ is around 30. The period of the multilayer is 2 nm. Compared to crystals, these multilayer mirrors provide about a 50-fold increase in photon flux on the sample due to their lower energy resolution. This adaptable

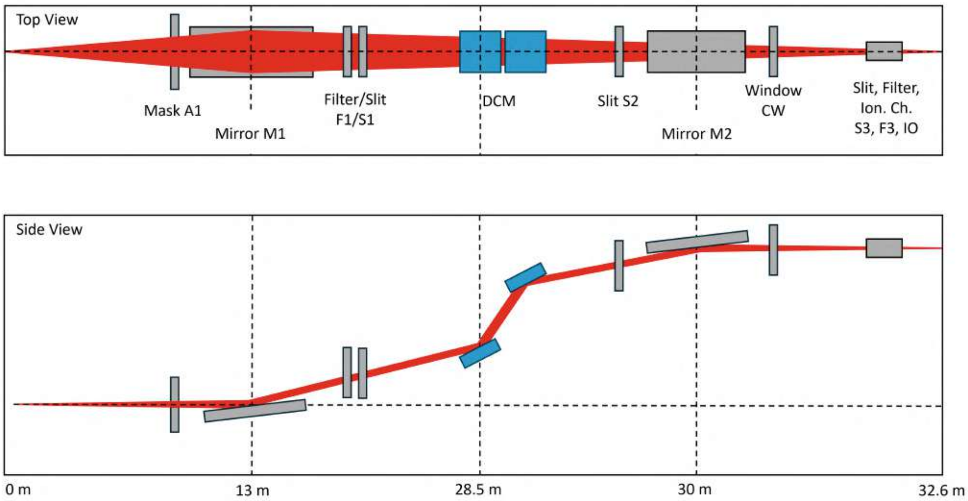

Fig. 3.2: Optical configuration of the μSpot beamline. Adapted from Zizak [122]

monochromator is designed for a range of experiments, allowing the photon flux and energy bandwidth to be selected as required [122].

The GEXANES experiments used the DCM Si(111) configuration, which is favored for its superior energy resolution. This high resolution is particularly critical for XANES analysis, which requires precise detection of subtle shifts and features in the absorption spectra.

3.2 pnCCD

The GEXANES experimental setup incorporates a pnCCD area and an energy-sensitive detector. This type of detector is well known for its ability to distinguish between different energies, and its 12.7 x 12.7 mm^2 area is invaluable in providing a scanning-free approach. Such an approach not only simplifies the experimental process but also leads to a significant reduction in data acquisition time. The pnCCD is different from detectors like the PILATUS because its pixels are smaller. This makes it possible to get better angular resolution in grazing emission setups [23, 89]. In addition to the timesaving and simplified experimental setup, the pnCCD detector is even more important for the present study because it can analyze specific X-ray emission lines and increase the reliability and precision of data interpretation. The design, development, and subsequent validation of this detector were a joint initiative of the Institute for Scientific Instruments GmbH (IfG), the Federal Institute for Materials Research and Testing (BAM), PNSensor GmbH, and the Institute for Applied Photonics e.V. (IAP).

Technical Overview of the pnCCD Detector:

- **Composition**: Housed within a robust frame, the detector is equipped with cooling, data acquisition apparatus, and specialized software.
- **Resolution attributes**: Offering a matrix of 264 x 264 pixels, it boasts 69,696 pixels, with each pixel sized at 48 x 48 μm^2. This results in an imaging area of 12.7 x 12.7mm^2 [126, 127].
- **Functional characteristics**: Its effectiveness is noticeable in the X-ray spectrum and is designed for quick parallel readout. It has an energy resolution of 152 eV at the manganese K_α emission line (5898.75 eV), comparable to the Silicon Drift Detector (SDD). Its frame rates can be selected between 400 Hz and 1000 Hz and has a quantum efficiency of over 95% between 3 keV and 10 keV. Detailed specifications are provided in Table 3.1 [127].

Parameter	Value
pnCCD type	column-parallel, split frame readout
Pixel size	48x48 μm^2
Number of pixels	69696
Image area	12.7 x 12.7 mm^2
Sensitive depth	450 μm
Frame rate	400 Hz-1000 Hz
Pixel readout speed	28 Mpixel/s
Quantum Efficiency	>95% at 3keV -10keV; >30% at 20keV
Readout noise (rms)	<3e$^-$ / pixel
Charge transfer eff.	>0.99995

Tab. 3.1: Summary of the pnCCD parameters

- **Detector architecture**: The detector uses a 450 μm thick n-doped silicon substrate surrounded on both sides by p+ structures. At the back there is a homogeneous p+

doped layer for radiation penetration. In front, there are p+ sections structured in a three-phase arrangement, three of which form a pixel for charge dynamics. When voltage is applied, the n-doped silicon substrate is fully activated against radiation [127].

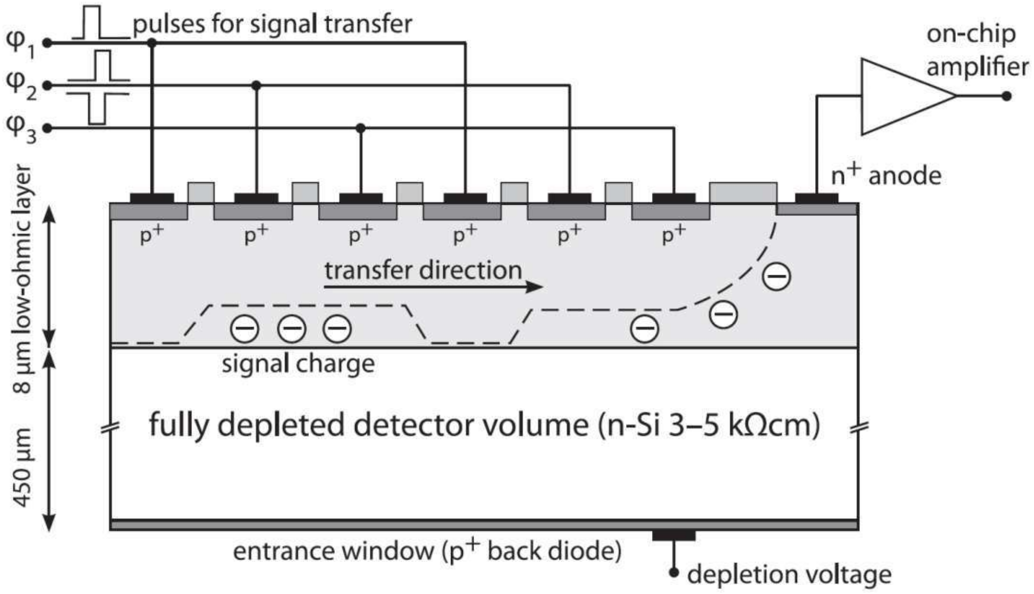

Fig. 3.3: Diagram showing the working mechanism of the pnCCD. Photons entering from the backside of the detector creates electron clouds that are trapped in electric potential minima. Each pixel uses three registers ($\varphi1$, $\varphi2$, $\varphi3$) to transmit the signal charges to transmit the signal charges to a JFET located at the end of each row. This process happens simultaneously on all channels. Adapted from Ordavo et al. [127]

- **Principle of operation**: A pnCCD works when an X-ray photon strikes the substrate, creating electron-hole pairs. Under voltage, these pairs separate, and electrons are collected at the potential minimum of each pixel. Fast recording voltage shifts allow the transfer of electrons to neighbouring pixels, as shown in detail in Figure 3.3. The pnCCD performs a channel-parallel readout, meaning that all pixels in a row are processed simultaneously. Each CCD channel results in an on-chip junction field-effect transistor (JFET) in a source-follower configuration, whose gate is connected to the corresponding readout anode for initial amplification.

Simultaneous readout, known as channel-parallel readout, uses a local amplifier for the initial signal, which is then processed by four dedicated chips [127].

- **Analysis software**: By evaluating the electrons produced, the software distinguishes the position and energy of the photon. Cases where electron clouds from an event spread across several pixels, known as "split events", are handled by summing electrons from nearby pixels. This remains accurate until event overlap potentially affects the count rate [126].

3.2.1 Incorporation and benefits of the pnCCD detector on GEXANES setup

A major advantage of the GEXANES setup is the integration of the energy-sensitive pnCCD detector. This integration enhances the ability to differentiate the fluorescence signal based on its energy. In conventional area-sensitive detectors, the angular intensity profile represents the cumulative number of photons in all energies. With the pnCCD, however, it is possible to discriminate between different emission lines, allowing only the desired angular intensity profile of a specific emission line to be captured.

Figure 3.4 illustrates the need for an energy sensitive approach. It shows angular intensity profiles for a reference sample consisting of a double layer structure on Si wafer with a 500 nm chromium metal layer on top of the wafer and a 300 nm chromium oxide layer on top of the chromium metal layer. The full spectrum counts are shown in red, the Cr-K_α emission line in blue, and the Cr-K_β emission line in orange. These variations in the angular intensity profile are important in determining the number of layers present in the sample being analyzed.

In particular, the Cr-K_β emission line (5946.8 eV) appears at lower angles than the Cr-K_α line (5411.6 eV). This variation in the angular intensity profiles is due to the high emission energy of Cr-K_β, which is characterized by a different complex refractive index and wave numbers compared to the Cr-K_α emission line. Therefore, if the total number of photons spanning different emission lines is analyzed, it could potentially mask the true number of layers in the sample. In contrast, isolating and analyzing the Cr K_α and

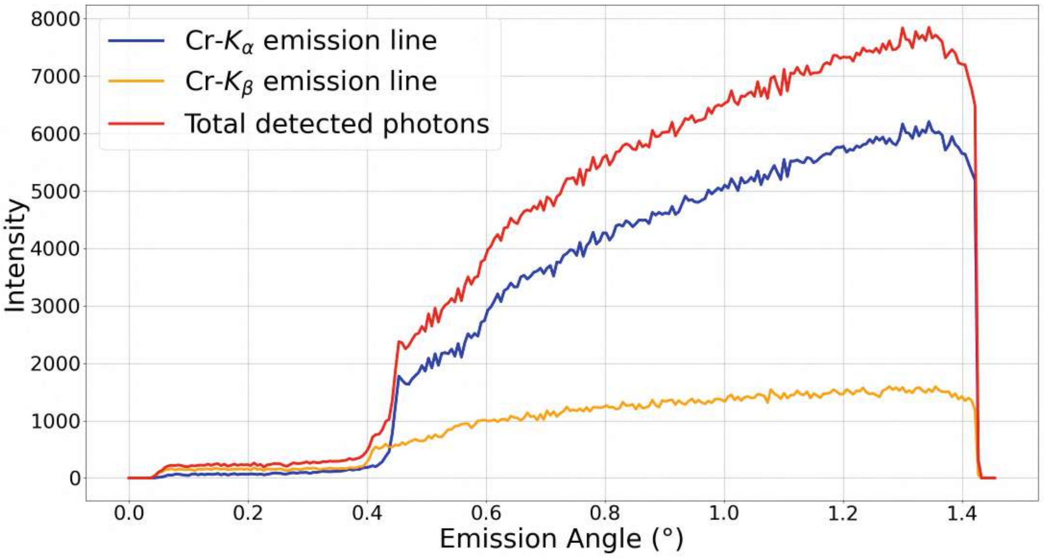

Fig. 3.4: Angular intensity profiles of reference sample, derived from the total photons detected (in red), alongside the Cr-K_α emission line (in blue) and the Cr-K_β emission line (in orange) for the reference sample, illuminated at 6033 eV.

Cr-K_β signals separately offer more accurate XANES results. The energy-sensitive pnCCD detector also provides the unique advantage of being able to examine multiple atoms simultaneously during a single measurement.

3.3 Geometrical arrangements

An important measure of this setup is the distance between the sample and the detector. This distance must be carefully chosen so that XRF signals emitted from different layers within the sample can be distinguished by the angular intensity profiles on the detector. If the angular resolution is insufficient, there is a risk that fluorescence signals emitted by different layers at different depths within the sample will overlap. To avoid such interference and to accurately resolve the depth profile, it is important to provide a reduced solid angle of detection per each pixel of the detector.

Figure 3.5 represents the experimental setup of the GEXANES. Ensuring this shallow opening angle with detectors of fixed pixel size requires increasing the distance between the sample and the detector (referred to as D in Figure 3.5). In the GEXANES, this increase

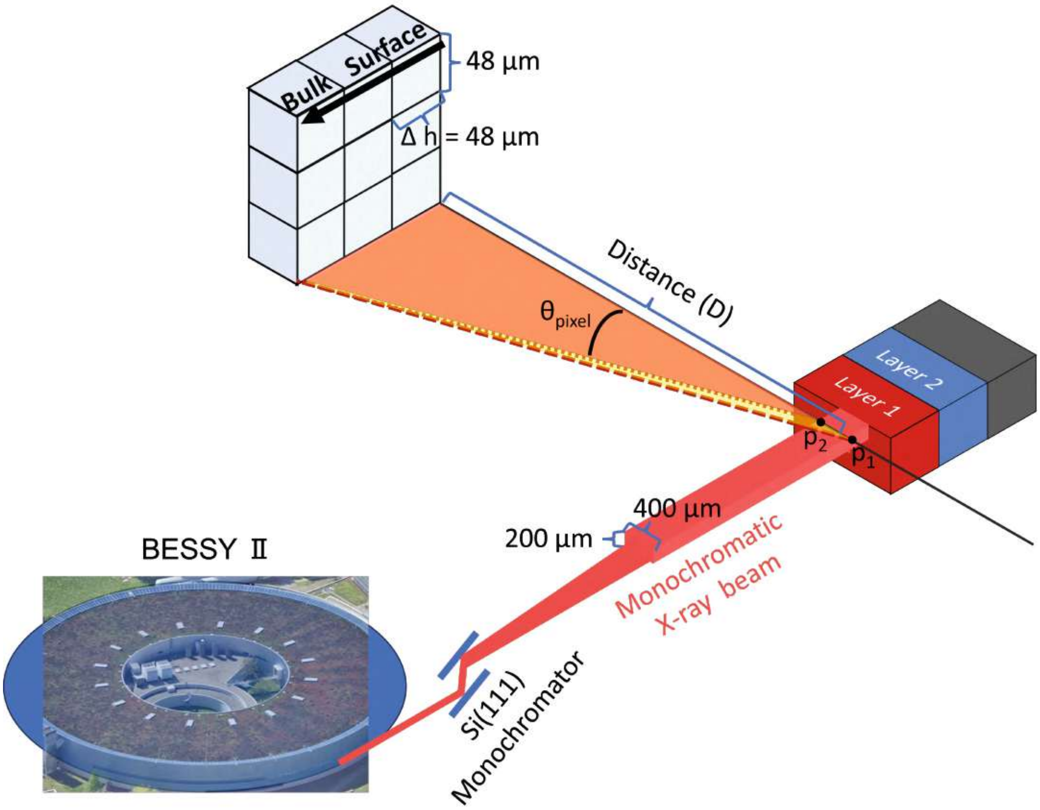

Fig. 3.5: Schematical representation of experimental setup.

causes the solid detection angle to decrease and subsequently the detected intensity to decrease by a factor equivalent to D^2. It should be emphasized that although an increase in D leads to an increase in air absorption, this effect is insignificant when compared with the decrease in the solid detection angle. This air absorption can be effectively avoided by creating a vacuum or applying a helium atmosphere.

The pnCCD's maximum range of detectable emission angles (θ_{pixel}) can be calculated using following formula:

$$\theta_{pixel} = arctan(\frac{n_{pixel}\Delta h}{D}) \tag{3.1}$$

where n_{pixel} is the number of pixels on a specified axis and Δh the pixel height, given as 48 μm.

Furthermore, the solid angle between two specific pixels (j, k) can be determined by the following equation:

$$\Delta\theta_{pixel} = arctan(\frac{jn_{pixel}\Delta h}{D}) - arctan(\frac{kn_{pixel}\Delta h}{D}) \tag{3.2}$$

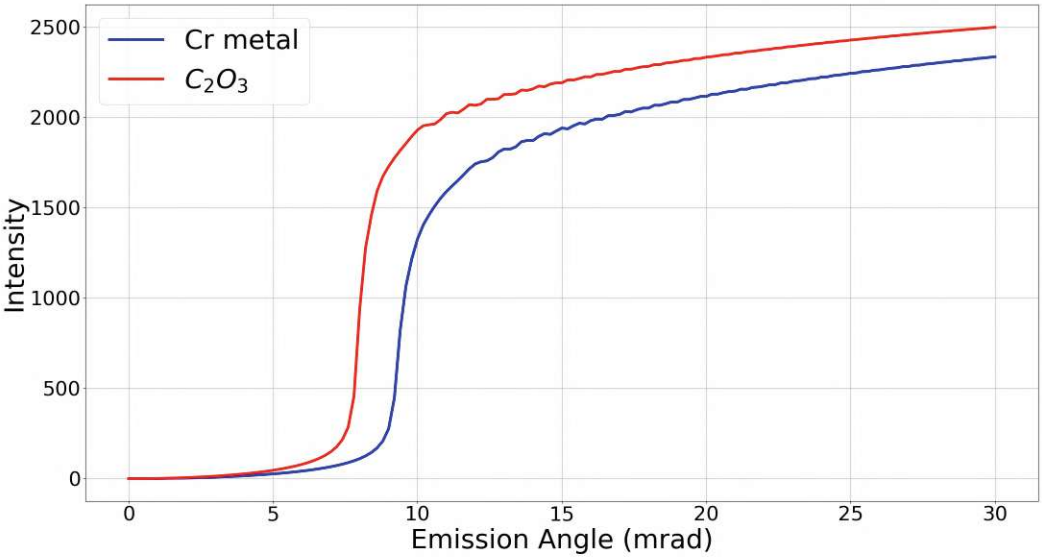

Fig. 3.6: Calculated angular intensity profile of Cr metal and Cr_2O_3 with 300 nm thickness on Si substrate.

The initial step in determining the optimal distance between the detector and the sample involved using the formula outlined in the 'Calculation of intensity' subsection. This formula was employed to calculate theoretical angular intensity profiles for both Cr metal layer and Cr_2O_3 layer on a Si substrate. The resulting angular intensity profiles from these calculations are depicted in Figure 3.6. These profiles were calculated for Cr metal and Cr_2O_3 layers, each with a thickness of 300 nm.

Figure 3.7 illustrates the first derivative of these results, employed to precisely determine the shift between angular intensity profiles. As indicated in Figure 3.7, the difference between the peaks is approximately 1.38 mrad, or equivalently, 0.08°. The choice of a range of about 15 pixels was sufficient for a reasonable duration of the experiment.

Due to these considerations, a D value of 50 cm was opted for, aiming to optimize the balance between angular resolution and data collection time. This distance provides a comprehensive angular range of 1.455° and a horizontal solid angle of 0.0055° per pixel. It should be noted that when an incident beam excites an area of material (400 μm x 200

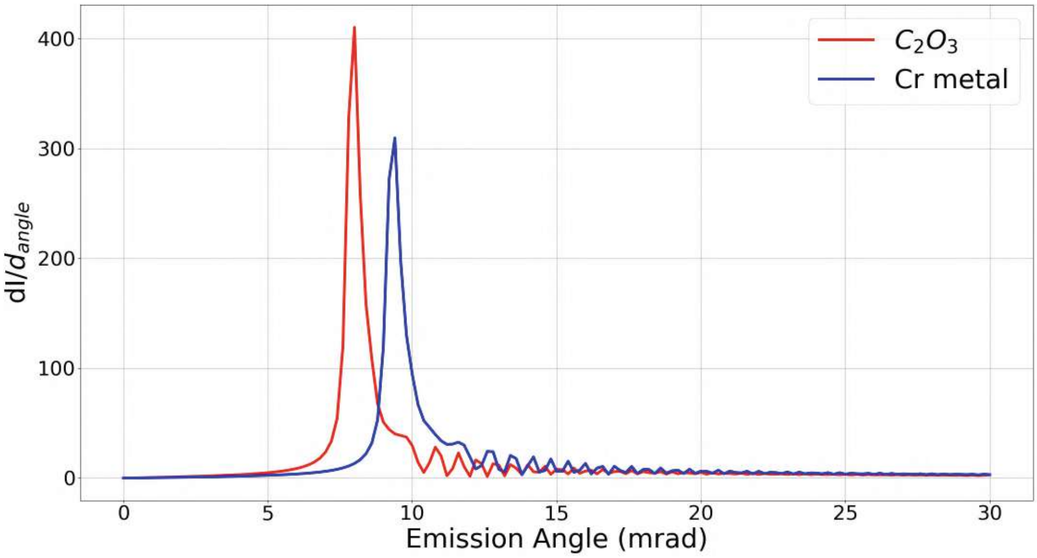

Fig. 3.7: Derivative of the calculated angular intensity profiles of Cr metal and Cr_2O_3.

μm), the fluorescence signal hits the detector at varying solid angles. However, at D=50 cm, the variability in the detected angles is negligible, only ± 4.44x$10^{-6\circ}$ per pixel.

3.4 Information depth

The depth range probed in a GEXANES measurement is primarily determined by the energy of the fluorescent X-ray. The experimental procedure analyzes the emitted fluorescence signal from the sample, which has a constant energy. The critical angle of total reflection can be calculated using the following formula:

$$\theta_{critic} = \sqrt{2\delta} \tag{3.3}$$

where δ is the real part of the complex refractive index.

During energy scanning in the experimental procedure, the critical total reflection angle is constant due to the constant emitted energy. The perpendicular entrance of the primary beam minimizes the attenuation of the incident beam in this method. This is due to the reduced path length of the incident beam through the sample compared to other methods such as GIXRF or TXRF. However, GE geometry presents a challenge in terms of "sample self-absorption". This is because fluorescence emitted from deeper levels must travel a longer path through the remaining sample material before reaching the detector. However, previous studies indicate that the GE setup experiences less self-absorption effects than the GI setup [89, 90].

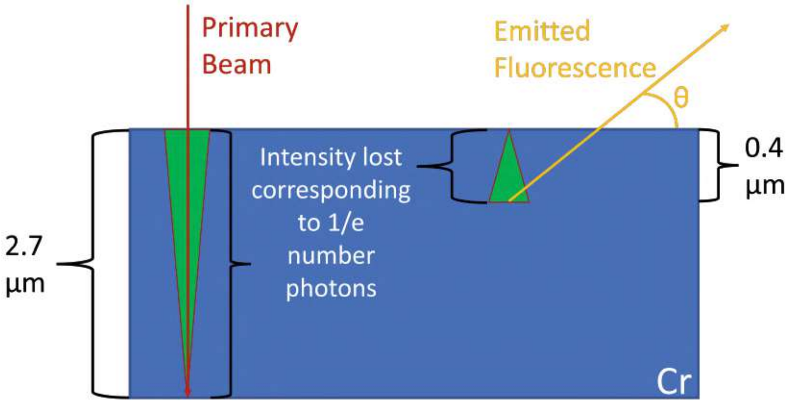

Fig. 3.8: Schematical representation of the penetration and information depth until intensity lost corresponding to 1/e number photons in Cr metal.

In the case presented, the energy of the incident beam is between 5975 and 6035 eV. If the energy is below the absorption energy, the beam can penetrate deeply. However, when the absorption energy is reached, the penetration depth decreases dramatically. As a result, the attenuation length for both Cr_2O_3 and Cr metal ranges from 33 μm to 2.7 μm within this energy range. Regardless, the total thickness of the sample layers is expected to be less than 2.7 μm in all cases. Given these details, the primary beam will penetrate deep enough for analysis. For constant-energy photons emitted by the sample under analysis, the context changes slightly. Given our geometric configuration, only 1/e of the signal emitted from a depth of 430 nm is detectable; the rest is absorbed by the sample before it reaches the detector (see in Figure 3.8).

3.5 Data processing

The first step in data processing, performed by the pnCCD software, involves background correction by subtracting a dark image and removing cosmic rays. The software then formats the 3D data captured by the pnCCD detector, which consists of arrays of 264 x264 pixels. Each pixel functions as a silicon drift detector, recording an XRF spectrum across 1024 energy channels at a frame rate of 1024 Hz. This results in a comprehensive 3D dataset (264 x 264 x 1024), as shown in Figure 3.9.

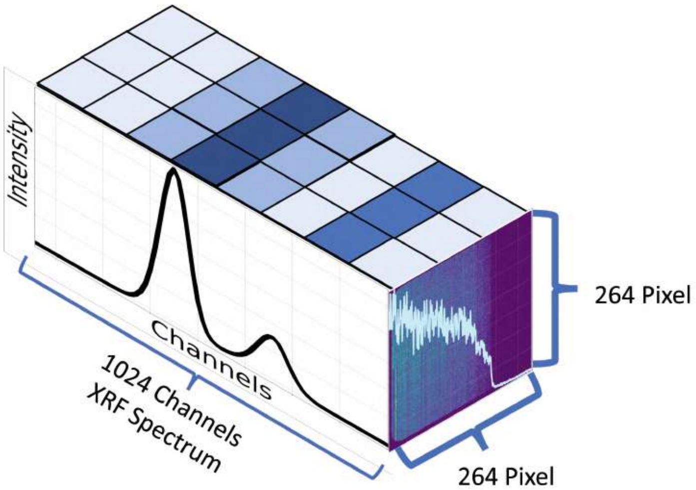

Fig. 3.9: Schematical representation of 3D data cube obtained from pnCCD detector.

To refine this dataset, the channel corresponding to the center of the fluorescence line of the analyzed atom is identified. The pnCCD software simplifies this step by allowing direct selection of the element of interest. For example, the Cr-K$_\alpha$ emission line corresponds to channel 205. A region of interest (ROI) is defined as ± 10 channels around this center, reducing the dataset to a smaller 3D data cube of size 264 x 264 x 21. This step effectively removes scattering peaks and other unwanted contributions, such as K$_\beta$ lines or fluorescence from other atoms.

Next, the data is converted to a two-dimensional (2D) format by summing the intensities across the selected ROI channels. In the resulting 2D data:

- The horizontal axis represents the emission angle, showing how intensity varies with depth.
- The vertical axis represents signals collected from the illuminated area of the sample, and summing it improves the statistical accuracy of the angular intensity profiles.

Figure 3.10 illustrates the selected ROI in the XRF spectrum and the corresponding 2D dataset derived from it. These angular intensity profiles are further analyzed as a function of excitation energy within the XANES region of the analyzed atom to generate depth-resolved XANES spectra.

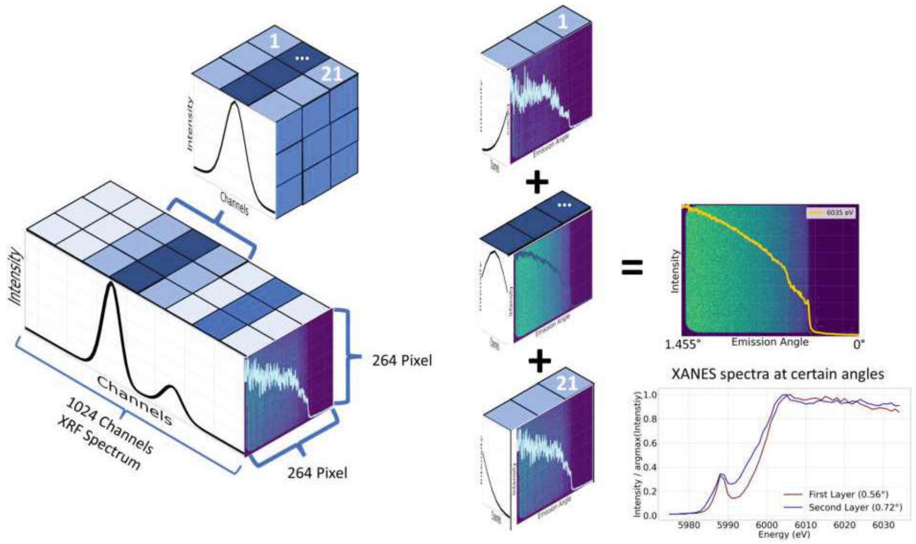

Fig. 3.10: Illustration of generation of angular intensity profile.

3.5.1 Decomposition of the multilayered sample data

In the present study, non-negative matrix factorization (NMF) enhanced by coordinate descent (CD) was used to decompose the angular intensity profiles of different layers within the samples. NMF is a dimensionality reduction technique designed to decompose a non-negative matrix into two smaller non-negative matrices, W and H, making it easier to interpret the data. This process simplifies the complex relationships in the data while preserving the most relevant patterns and minimizing information loss [128].

Mathematically, the decomposition aims to approximate the original matrix V as follows [128]:

$$V \approx W \times H \tag{3.4}$$

where:

- V is the original non-negative matrix $(m \times n)$ representing the data to be analyzed.

- W is a matrix ($m \times k$) representing the basis patterns (in this context, related to individual layers).
- V is a matrix ($k \times n$) representing the contributuins of these patterns.
- k is the number of components, corresponding to the number of layers in the sample.

The optimization objective is to minimize the difference between V and the product $W \times H$, typically measured using the Frobenius norm [128]:

$$\|V - WH\|_F^2 = \sum_{i,j} (V - WH)_{i,j}^2 \tag{3.5}$$

Like PCA, NMF reduces the dimensionality of the data, allowing us to interpret complex datasets more easily. In PCA, the data matrix is decomposed into principal components (directions of maximum variance) and their weights. However, PCA allows for negative values in its components, which can be less interpretable when dealing with count data like intensities, where negative values have no real meaning. NMF, on the other hand, ensures that all components and weights are non-negative, making it especially useful for datasets like intensity profiles, where values are inherently non-negative.

In this study the dataset is three-dimentional. The variation of intensities occurs as a function of emission angle and energy. This can be thought of as a large matrix V containing the intensity values, indexed by energy and emission angle. By applying NMF, V matrix decomposed into two matrices:

- W represents the intensity - emission angle relationship, isolating angular intensity profiles for each layer.
- H represents the intensity - energy relationship, isolating the XANES spectrum of each layer.

The optimization to find W and H is performed using coodinate descent (CD). The idea behind CD is to optimize a multivariate objective function by breaking the problem into simpler sub-problems, where one variable (or "coordinate") optimized at a time, while holding all other variables constant. In the context of NMF, coordinate descent is used to minimize the Frobenius norm of the difference $\|V - WH\|_F^2$. The optimization alternates betwen fix H and update W one element at a time and fix W and update H one element at a time. This iterative process converges to a local minimum of the objective function, effectively decomposing V into the two factor matrices W and H [128].

3.6 Implementation of bayesian optimization to data acquisition

The integration of Bayesian optimization (BO) into our GEXANES data acquisition workflow marks a significant methodological advancement. BO is a probabilistic model-based optimization technique, particularly well-suited for scenarios where objective function evaluations are resource-intensive. This capability makes it an invaluable tool for optimizing experimental procedures. Figure 3.11 illustrates the integration of BO into the data collection process at the BESSY II μSpot beamline.

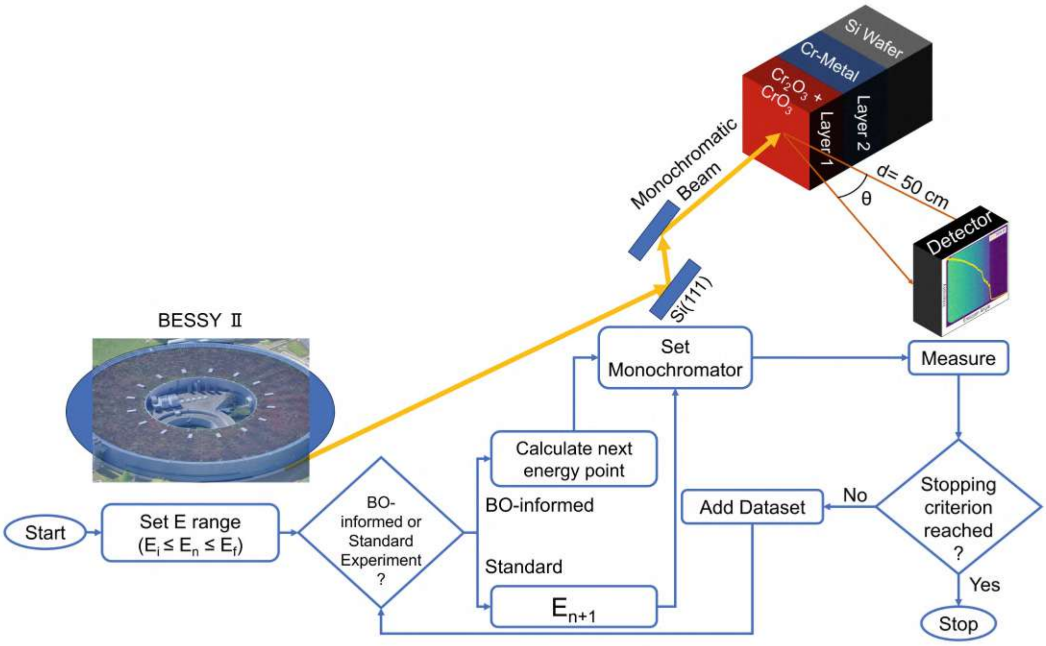

Fig. 3.11: Overview of the BO-informed experimental process used in the GEXANES technique. This illustration highlights the key steps of our approach.

3.6.1 Data Flow and System Integration

The BO algorithm is implemented on the control computer of the pnCCD detector. Analog data from the detector is first converted into digital form via an analog-to-digital converter (ADC) and subsequently transferred to the control computer. This raw digital data is processed by Racoon software and stored in a designated memory location on the same computer. To efficiently access this data, QSharedMemory is used to retrieve it directly from the memory region, avoiding the overhead and latency associated with network-based data transfer. This setup ensures efficient communication between the BO algorithm and the pnCCD detector, which is critical given the substantial data volume generated by the detector.

3.6.2 Workflow and Iterative Process

With the data flow established, the experimental workflow begins by defining the energy range for measurements (5975–6035 eV in this study). The process is initiated by placing seven equidistant points within the defined energy range. Measurements are taken at these initial points to create a baseline data set.

The iterative process then involves the following steps:

1. **Energy Prediction:** The BO algorithm uses the initial data set to predict the next energy point based on the Gaussian process model.
2. **Conversion and Execution:** The predicted energy value is converted into the corresponding angle for the monochromator. The calculated angle is then sent to the monochromator motors.
3. **Data Acquisition:** Once the monochromator is set to the target angle, it signals the BO algorithm, which triggers the pnCCD detector to collect data.
4. **Integration and Update:** The acquired data is processed, integrated into the existing data set, and used to refine the Gaussian process model.

This cycle is repeated iteratively until a predefined stopping criterion, such as a maximum number of iterations, is met.

3.7 Analyzed materials for case study

The case study was conducted by creating and analyzing a benchmark sample and two real-life samples. These samples were carefully designed, synthesized, and subjected to a thorough analytical process. The effectiveness and accuracy of our methodological approach were confirmed by a well-structured reference sample. This reference sample was prepared with a known and precisely defined composition and layer thickness. This factor is extremely important, especially given the nature of the oxidation process, which offers no controls to achieve a specific layer thickness. Due to the unpredictable nature of this process, it was important to have a solid reference sample to confirm the accuracy of the results.

3.7.1 Cr-Oxide / Cr reference sample

The analysis of a sample containing multiple film layers is primarily focused on this research, and the sample was produced by magnetron sputtering by the Chair for Materials Discovery and Interfaces, Ruhr-University Bochum, Germany. The properties of the layers had been controlled via process parameters. The magnetron sputtering technique allowed us to create films from chromium (Cr) obtained from an elemental target. Careful planning and execution of this procedure, using state-of-the-art equipment, allowed precise control over the sample properties. The specifics of the method used are described here, including the materials, gases, and parameters that were allowed to ensure its consistent quality. Figure 3.12 illustrates the reference sample.

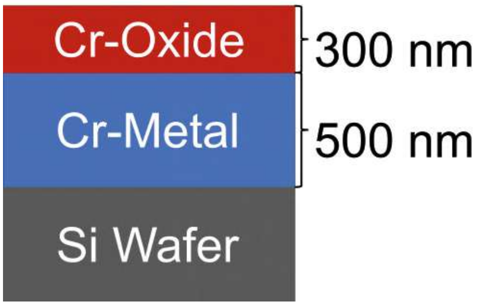

Fig. 3.12: Schematic representation of the reference sample

The film was prepared by sequential magnetron sputtering of Cr from an elemental target (pure metal disk, 4-inch diameter, 99.95% Cr purity, Sindlhauser Materials GmbH) in a commercial sputtering system (AJA International, ATC 2200). The Cr target was sputtered at a direct current (DC) power of 100 watts. During the synthesis phase, Ar and O2 gases with a high purity of 6N (99.9999%) were used. The argon gas line is equipped with a SAES Pure Gas Type MC1-903T purifier, which effectively removes elements such as O_2, H_2O, CO, CO_2, organic/NMHC compounds below 100 ppt, and a 0.003 µm particle filter. The base pressure of the operating system was in the range of 10^{-6} Pa. All coatings were applied at a measured pressure of 0.4 Pa, at room temperature, without heating. A 500 nm metallic Cr layer was sputtered with a steady flow of Ar at a rate of 80 sccm. On top of this chromium layer, a secondary layer of chromium oxide was sputtered with a thickness of 300 nm. For this process, an O_2 / Ar flow ratio of 40 sccm / 80 sccm was maintained. The thickness of both the metallic chromium and chromium oxide layers was controlled during the deposition phase by using the predetermined deposition rates: 0.085 nm/s for chromium and 0.0144 nm/s for chromium oxide, according to the specific sputtering parameters. Adherence to these measures ensured a high degree of precision and consistency throughout the fabrication process.

3.7.2 Compositionally complex CrCoNi alloy

CrCoNi represents a unique class of alloys within the broader category of compositionally complex alloys (CCAs). This equiatomic ternary alloy, comprising chromium, cobalt, and nickel in approximately equal atomic ratios, falls under the classification of medium-entropy alloys (MEAs) [129]. While MEAs contain fewer elements than traditional high-entropy alloys (HEAs), they still exhibit many of the remarkable properties associated with CCAs [130]. CrCoNi is characterized by its face-centered cubic (FCC) solid solution structure and has garnered significant attention due to its outstanding mechanical properties. These properties, including exceptional strength, ductility, and fracture toughness, often surpass those of conventional alloys and even some more complex HEAs. The oxidation behavior of CrCoNi, particularly under high-temperature conditions, is a subject of ongoing research interest. This interest is partly due to the presence of chromium, known for its ability to form protective oxide layers [4]. Given its relatively simple composition compared to more complex HEAs, CrCoNi serves as an ideal model system for investigating and understanding the fundamental principles underlying the unique properties of CCAs.

The case study for the actual samples is a compositionally complex CrCoNi alloy made from metals with an extremely high purity level of 99.9%. The alloy was melted in a specialized vacuum induction melting furnace, specifically a Leybold Heraeus IS 1/III. The objective was to detect Cr oxide layers formed after exposure to high temperatures and cooling using GEXANES.

During the melting and casting phases, strict measures were taken to protect against oxidation. The furnace chamber was first evacuated to a pressure of 3 mbar. After this evacuation, the chamber was filled with Ar and the pressure increased to 500 mbar. After successfully producing ingots weighing approximately 2.1 kilograms each, the diameter reduction process was applied. The initial diameter of 45 mm was reduced to 40 mm by turning the ingots on a lathe, giving them the desired dimensions for the next steps.

The ingots were then sealed in evacuated quartz tubes at a pressure of 3×10^{-5} mbar. The ingots were then homogenized at 1200 °C for 48 hours. After homogenization, the diameter of the ingots was further reduced to 17 mm using a rotary swaging operation. Importantly, this operation was performed at room temperature to avoid any thermal influence on the alloy properties. One sample was subjected to a temperature of 600°C for 10 minutes and one to a higher temperature of 800°C for one hour. These procedures were performed in a tube furnace with an atmospheric composition of 2% O_2 and 98% Ar. This controlled environment provided optimal conditions for the processes.

The heating and cooling processes were performed under an argon atmosphere at a controlled rate of 10 K per minute. Argon of high purity (99.999%) was used for these processes, containing minimal impurities such as 2 ppm O_2, 3 ppm H_2, and 5 ppm N_2. Once the target temperatures were reached, an oxidizing gas was introduced into the tubular reactor chamber. The introduction of this gas was carefully controlled to maintain the consistency of the gas mixture. It is worth noting that when Cr is oxidized, it forms a protective layer. This layer acts as a barrier to further degradation of the material, maintaining its quality and integrity throughout the process.

In this study, CrCoNi was chosen as the real-life material due to its extensive research in the field of compositionally complex alloys (CCAs). This alloy has been the subject of numerous research studies, resulting in a rich repository of data covering a wide range of experimental conditions and applications. This extensive body of research provides a solid foundation for comparative studies, allowing us to compare new data with well-established findings.

Chapter 4

Results & Discussion

This chapter discusses the results of the GEXANES spectroscopy, divided into two main sections. The first section discusses the results obtained using the standard mode, which involves scanning a total energy range of 60 eV in discrete steps of 1 eV. The next section describes the use of an optimization mode, where the selection of energies is guided by the Bayesian optimization algorithm. In this work, the terms 'first layer' and 'second layer' refer to the layers of the reference sample (Cr and Cr-oxide layers), whereas 'surface layer' and 'bulk' are used to describe the layers of real-life MEA sample. The details of each mode are described in their respective sub-sections.

4.1 Proof of concepts

In order to validate the GEXANES technique with area- and energy-sensitive detectors, a reference sample was used. This sample consisted of a double layer structure: a 300 nm layer of mixed Cr_2O_3 and CrO_3 on top of a 500 nm layer of chromium metal, both deposited on a silicon wafer. The method was then used to study real-life materials, in particular compositionally complex CrCoNi alloys, exposed to corrosive environments at high temperatures ($\geq 600°C$). Such materials are promising for corrosion prevention. At elevated temperatures, chromium is known to form an oxidized surface layer, which acts as an oxidized surface layer that acts as a protective barrier against further material corrosion.

4.1.1 Cr-Oxide / Cr reference sample

In this study, the known composition of the reference sample provides a benchmark. This is particularly crucial for the validation of a new analytical method. This allows the sensitivity of the GEXANES method to be evaluated.

Measurements for GEXANES were performed in standard mode with the incident energy scanned between 5975-6035 eV in 1 eV increments. Each increment was measured for 20 minutes. This duration was required to achieve a total count rate of 10^6 for the entire XANES spectrum at the Cr-K_α peak.

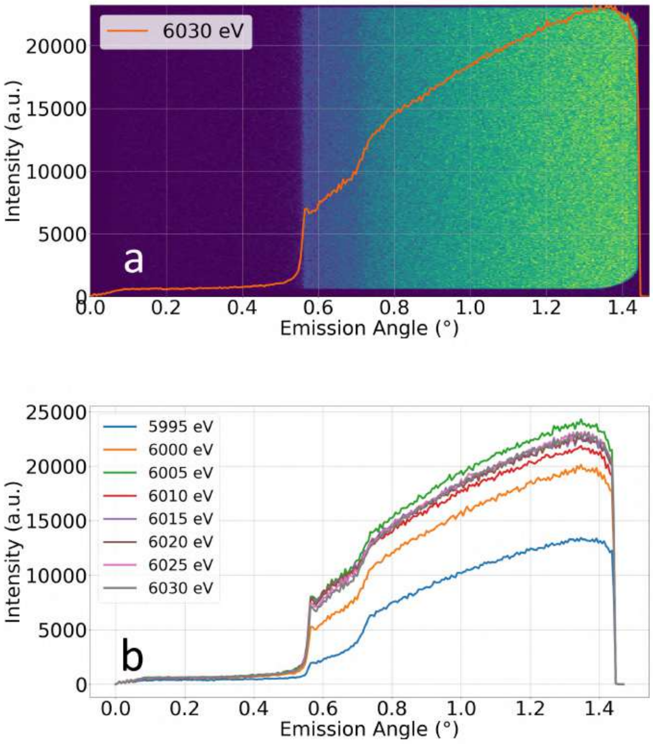

Fig. 4.1: a) Angular intensity profile of the reference sample at 6030 eV. b) Collection of angular intensity profiles of the reference sample as a function of excitation energy.

The initial phase of the analysis focused on the angular intensity profile of the reference sample, particularly at 6030 eV - an energy level beyond the chromium K absorption edge. This investigation was critical to understanding the layered structure. Figure 4.1(a) shows the presence of two distinct intensity jumps at emission angles of approximately 0.5° and 0.7°. These variations are key to identifying the layered composition of the sample, with the shallower angle corresponding to the surface chromium oxide layer and the wider angle indicating the deeper metallic chromium layer.

The next stage of the investigation was to examine the behaviour of the intensity variations of the reference sample over a range of excitation energies in order to establish a full XANES profile. As shown in Figure 4.1(b),the intensity fluctuations at approximately 0.55° and at about 0.7° showed distinct patterns over different excitation energies. These different patterns serve as indicators of the different electronic structures and absorption properties of each of the two layers of the sample.

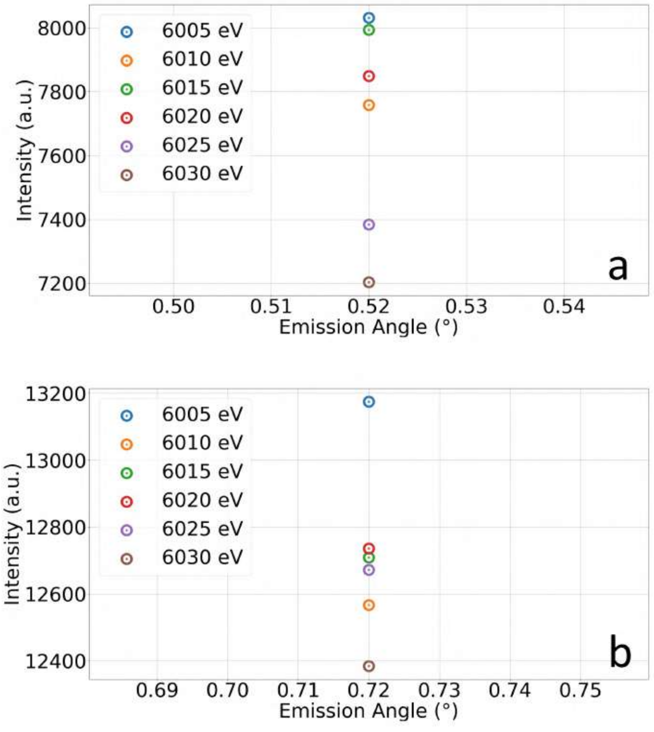

Fig. 4.2: (a) Intensity changes for different excitation energies at 0.52° emission angle. (b) Intensity changes for different excitation energies at 0.72° emission angle.

Detailed analysis of the intensity fluctuations across excitation energies, particularly at emission angles of 0.56° and 0.72°, as shown in Figures 4.2(a) and 4.2(b). The highest intensity at both angles is at 6005 eV, but the subsequent order of decreasing intensity shows some differences.

Specifically, at 0.72°, the descending order of intensities is 6020 eV, 6015 eV, 6025 eV, and 6010 eV, followed by 6030 eV. At 0.56°, the order is 6015 eV, 6020 eV, 6010 eV, 6025 eV, and then 6030 eV. These variations are due to different electronic environments of chromium in each layer, which will give rise to the XANES profile.

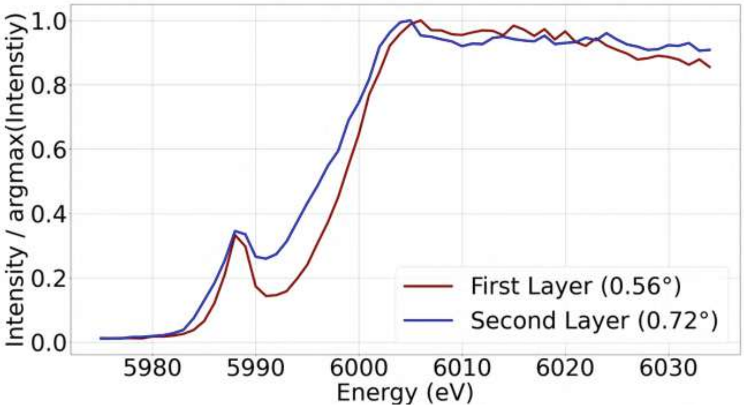

Fig. 4.3: XANES spectra at 0.56° and 0.72° Emission Angles.

Figure 4.3 shows the full XANES spectra for the reference sample, derived from the two specific emission angles of 0.56° and 0.72°. An s pre-peak visible in the spectrum from 0.56° is attributed to the 3d←1s dipole transition. Coordination with ligands induces hybridization of the 3d and ligand p-states, which is shown by the prominent pre-peaks seen in the XANES spectrum of the chromium oxide surface layer. Furthermore, the shift in the edge position observed in the spectra from both emission angles is a consequence of the increased oxidation state of the chromium cation. The increase in oxidation state in chromium oxide, i.e. the increase in the binding energy of the 1s electrons, results in a shift to a higher energy of the K-edge compared to chromium metal.

The derived XANES spectra are based on intensity measurements at specific emission angles, which represent only a fraction of the comprehensive data set collected. When XANES information is collected from only one emission angle, it can be difficult to interpret the spectrum.

In order to improve the signal-noise ratio, an advanced data processing routine was used. The implementation of this data processing started with the creation of a three-dimensional (3D) data cube, as visually shown in Figure 4.4(a). The 3D data cube contains a combination of the following data.

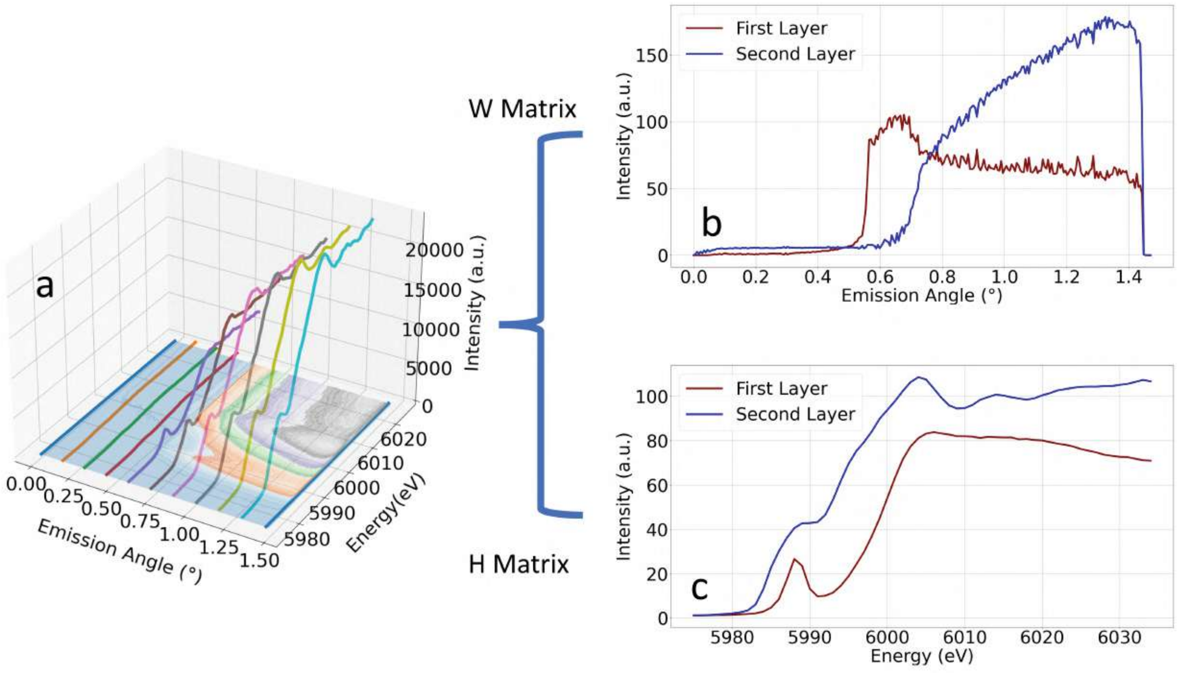

Fig. 4.4: NMF Decomposition of Data Cube: (a) 3D data cube with axes of emission angle, intensity, and excitation energy for reference sample. (b) 'W' matrix highlighting the distinct angular intensity profiles of the two layers for reference sample. (c) 'H' matrix showcasing the XANES spectra for both layers with improved signal-to-noise ratio for reference sample.

- Emission Angle: This dimension covers the range of angles at which X-ray emissions were measured and represents depth- or layer-specific information of the sample.
- Intensity: A measure of the strength of the emitted X-rays, this axis captures the variation in observed signals between emission angles and energies.
- Excitation Energy: This axis represents the energies at which the sample is excited and gives an insight into how different energies affect the emitted intensity and therefore the properties of the sample.

The three-dimensional data set was analyzed using non-negative matrix factorization (NMF) because the data contains only positive counts. Unlike principal component analysis (PCA), which can produce both positive and negative values, NMF keeps all values non-negative, making it more suitable for count data. This property of NMF aligns naturally with the data, making it easier to identify meaningful features and patterns. As a result, NMF provides a clearer, more interpretable analysis that highlights important characteristics in the data.

The pre-established knowledge of the bilayer structure of the sample guided the NMF process, where the number of components was set to two. This approach resulted in the decomposition of the data cube into ’W’ and ’H’ matrices representing different components of the original 3D data set. Figure 4.4(b) illustrates the ’W’ matrix. It shows the separate angular intensity profiles for each layer. Figure 4.4(c) presents the ’H’ matrix, which contains the XANES spectra from two different layers. This figure also highlights the improved signal-to-noise ratio in the XANES spectra obtained from the ’H’ matrix compared to those taken from a single emission angle. This improvement demonstrates the effectiveness of NMF. As a result, XANES spectra generated by NMF combine data from multiple angles, offering a more reliable and noise-reduced representation of the sample’s characteristics rather than depending solely on intensity variations from a single angle.

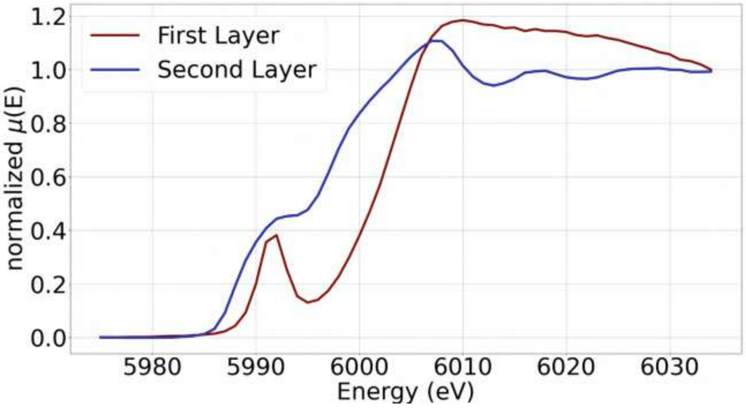

Fig. 4.5: Normalized XANES spectra for the first (chromium oxide) and second (metallic chromium) layers, derived from the ’H’ matrix of NMF analysis.

It was crucial to ensure comparability of the XANES spectra through normalization after subtraction from the ’H’ matrix. This process is performed using XASViewer software. Normalization adjusts the spectra by setting the pre-edge baseline to zero and normalizing the post-edge levels to one. This step is necessary to qualitatively compare different spectra and easily identify differences. The normalized spectra, as shown in Figure 4.5, include the spectra of the chromium oxide layer (first layer) and the metallic chromium layer (second layer).

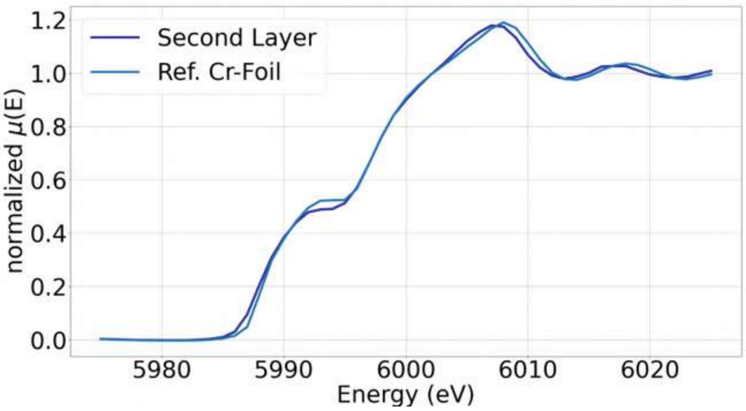

Fig. 4.6: Comparison of the normalized XANES spectrum of Second Layer with the reference spectrum from a Cr-Foil.

Figure 4.6 presents a comparison between the normalized XANES spectrum of the second layer and the reference spectrum derived from a chromium foil. This comparison reveals a notable consistency in the spectrum of the second layer with that of the reference chromium foil.

The XANES spectrum of the first layer is characterized by an increase in the pre-peak feature (at 5992 eV) and a shift towards a higher energy of the main absorption edge, now at 6003 eV (see Fig. 4.5). The XANES spectrum obtained from the first layer shows stronger similarities to CrO_3, despite a slightly less intense pre-peak and edge shift (see in Fig. 4.7).

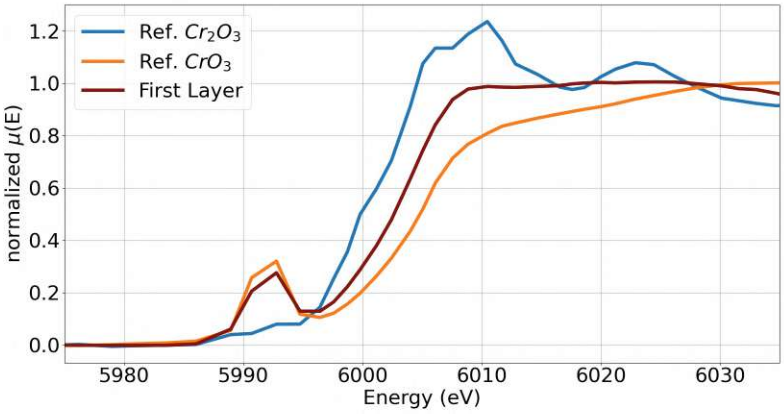

Fig. 4.7: Comparison of the normalized XANES spectrum of First Layer with the reference Cr-Oxides.

According to a literature search on the deposition method, several chromium oxidation products can be observed in similarly deposited samples [131]. Linear combination fitting (LCF) was used to identify these possible oxidation products. The LCF results show a contribution of Cr_2O_3 (35%) and CrO3 (65%). A comparison of the spectrum of this distribution obtained after LCF analysis with the spectrum of the first layer is shown in Figure 4.8(a). For a more detailed comparison, the first derivatives of these two spectra are also shown in Figure 4.8(b). This composition was confirmed by X-ray photoelectron spectroscopy (XPS), which gave Cr2p binding energies of 576.6 eV and 578.8 eV, in agreement with the known binding energies of Cr_2O_3 and CrO_3 respectively [132] (see Figure 4.8(c)).

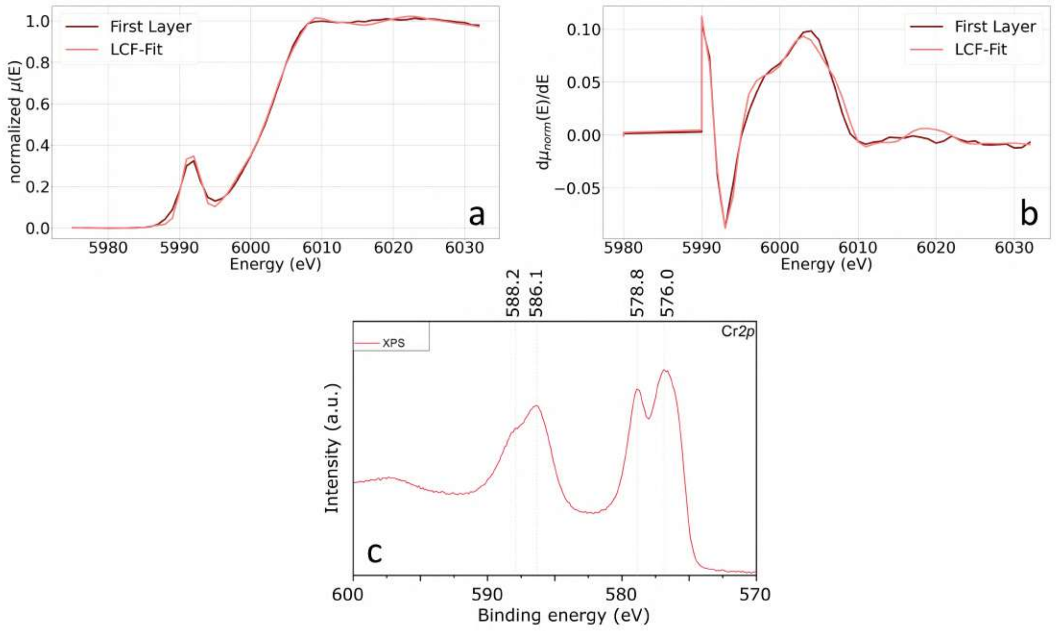

Fig. 4.8: (a) XANES spectrum of the reference sample first layer (red) and linear combination fitting (light red) in norm(E) (a); (b) the first derivative of the norm(E) (b); linear combination fitting results shows that the composition of the first layer is mixture of Cr_2O_3 (35%) and CrO_3 (65%) (R-factor = 0.0012255, X^2 = 0.00939, Reduced X^2= 0.0002041); (c) XPS spectrum of surface of the reference sample (Cr2p orbital) with peak positions. The peak at 576.0 eV corresponds to the Cr_2O_3 and the peak at 578.8 eV correspond to the CrO_3.

4.2 Compositionally complex CrCoNi alloy

The reliability of the employed methodology was demonstrated through the analysis of a reference sample. Subsequently, the focus shifted to the application of this approach to real-life samples. The chosen material for this study was the compositionally complex CrCoNi alloy. This alloy provided an opportunity to assess the effectiveness and adaptability of the technique in real-life scenarios. The following sections detail the findings from the comprehensive analysis of samples subjected to temperatures of 600°C and 800°C for periods of 10 minutes and 1 hour, respectively.

4.2.1 600° C for 10 minutes exposed sample

In order to obtain a thin oxide layer, the sample was exposed to a temperature of 600 °C for 10 minutes. Recognizing that the intensity of the signal from a thin oxide layer would be low, the exposure time for the 600 °C for 10 minutes sample was increased from 20 minutes to 30 minutes, distinctively from the procedure used for the reference sample. However, this extension in spot measurement time would consequently prolong the overall duration of the experiment. To maintain the experiment within a feasible timeframe, the energy range was restricted to 5975 eV to 6025 eV. Despite this narrower energy range, it remains sufficient to gather data on the pre-peak region and the edge shift, which are critical for analyzing the oxidation state. The first step was to analyze the angular intensity profile of the Cr-K_α emission line at 6025 eV, just beyond the K absorption edge. This analysis revealed the possible layers of the sample.

Figure 4.9(a) displays the angular intensity profile for this sample at 6025 eV. The angular intensity profile reveals two distinct intensity jumps. Closer inspection of the angular intensity profile shows a gradual increase in intensity with an angle up to about 0.8°, where a slight bend or 'shoulder' can be observed. Beyond 0.8°, and particularly after 0.9°, the intensity increases at a different rate, suggesting a change in behavior. This pattern suggests the presence of two distinct regions or layers within the sample; the shallower angles correspond to the surface, while the wider angles correspond to deeper levels (bulk).

To extend the analysis, angular intensity profiles were collected as a function of excitation energy, as shown in Figure 4.9(b). For clarity, Figures 4.9(c) and (d) show intensity variation at selected emission angles. 4.9(c) shows a sequence of intensities at a shallow angle of approximately 0.6°. The highest intensity is at 6005 eV. This is followed by 6010 eV and then 6015 eV. Conversely, a different order of intensities is observed in Figure 4.9(d), which captures data at a wider angle around 1.2°. In this plot, 6010 eV has the highest intensity, followed by 6005 eV. As mentioned earlier, such variations are caused by the different electronic environment of the chromium, which is used to create the XANES spectrum.

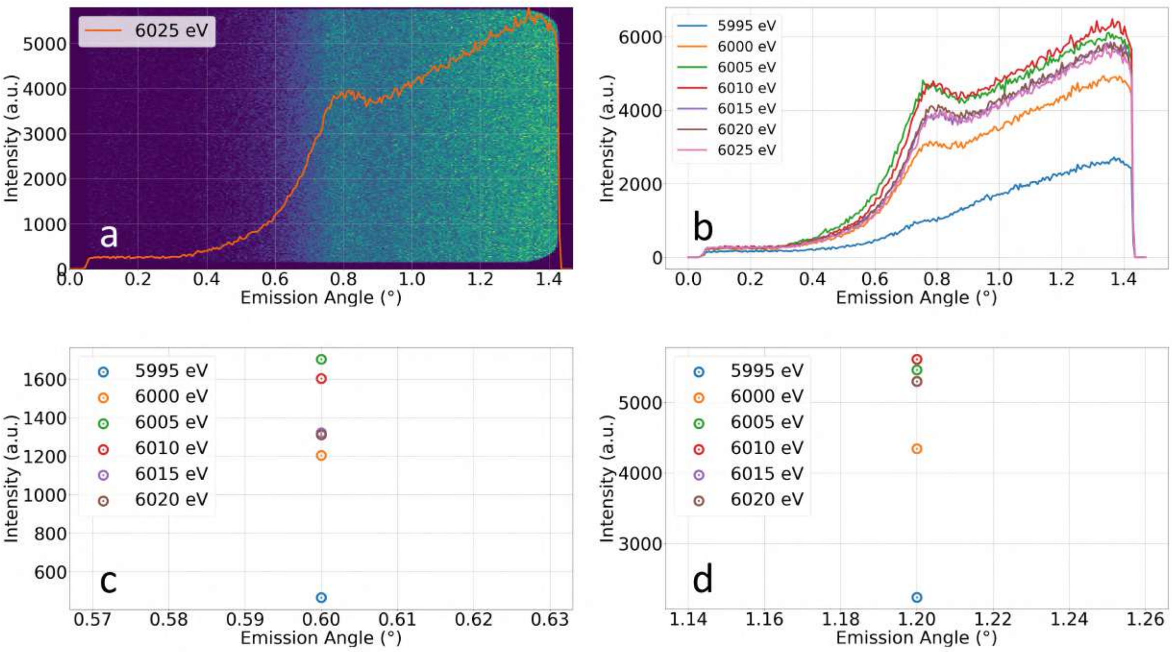

Fig. 4.9: (a) Angular intensity profile of the 600 °C for 10 minutes sample at 6025 eV. (b) Collection of angular intensity profiles of the 600 °C for 10 minutes sample as a function of excitation energy. (c) Intensity variation for different excitation energies at 0.6° and 1. d) at 1.2°

After data acquisition, the process was continued using NMF analysis. This technique, previously used in the evaluation of reference samples, is used to separate overlapping signals.

Figure 4.10(a) shows the 3D data cube for the 600 °C for 10 minutes sample used for NMF analysis. Similar to the reference sample, this visualization provides an overall view of the data set. Given the angular intensity profiles indicating two distinct layers in the

600 °C for 10 minutes sample, it was decided to select two components for NMF analysis. This process resulted in the extraction of 'W' and 'H' matrices representing the angular intensity profiles and XANES spectra of the respective layers within the sample.

Figure 4.10(b) shows the angular intensity profiles of the two layers identified in the 600 °C for 10 minutes sample after NMF analysis. The shape of the angular intensity profile corresponding to the surface layer is similar to the angular intensity profiles of the thin layers. As explained in the Methods section, the thickness of the layer has a significant influence on the shape of the angular intensity profile. This correlation between the thickness of the layer and the shape of the angular intensity profile can be used to determine the thickness of the layer from its angular intensity profile.The 'H' matrix shown in Figure 4.10(c), representing the XANES spectra of the two components.

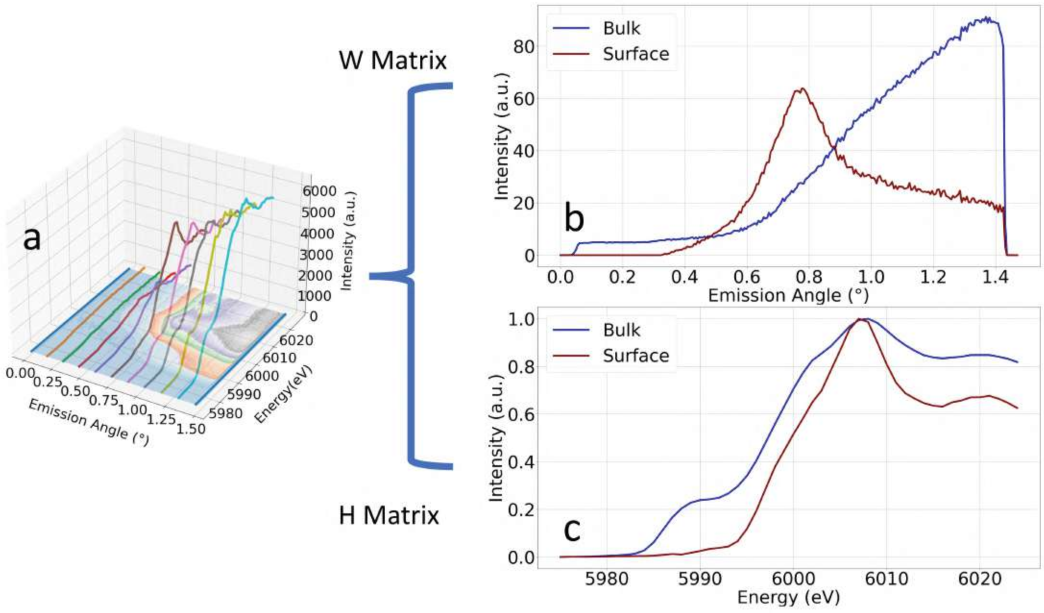

Fig. 4.10: NMF Decomposition of Data Cube: (a) 3D data cube with axes of emission angle, intensity, and excitation energy for 600 °C for 10 minutes sample. (b) 'W' matrix highlighting the distinct angular intensity profiles of the two layers for 600 °C for 10 minutes sample. (c) 'H' matrix showcasing the XANES spectra for both layers with improved signal-to-noise ratio for 600 °C for 10 minutes sample.

In Figure 4.11, the normalized spectra from both layers of the 600 °C for 10 minutes sample are depicted. In particular, the spectrum originating from the surface signal exhibits a positive edge shift, typically indicative of an oxidation state. In addition, the presence of two subtle peaks in the pre-peak region is consistent with the expected spectral signature of an oxide layer, namely Cr_2O_3.

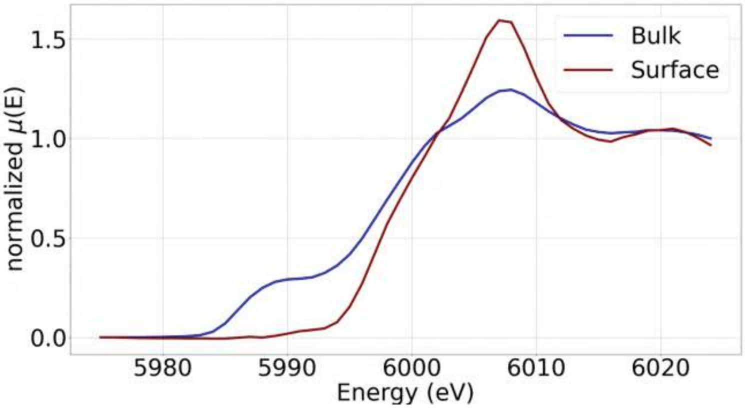

Fig. 4.11: Normalized XANES spectra for the surface layer (chromium oxide) and bulk (metallic chromium) part of the 600 °C for 10 minutes sample, derived from the 'H' matrix of NMF analysis.

Further analysis of the surface properties of the 600 °C for 10 minutes sample involves determining the oxidation state of the oxide layer present on the surface. This is accomplished by comparing the XANES spectrum from the surface with the reference spectrum.

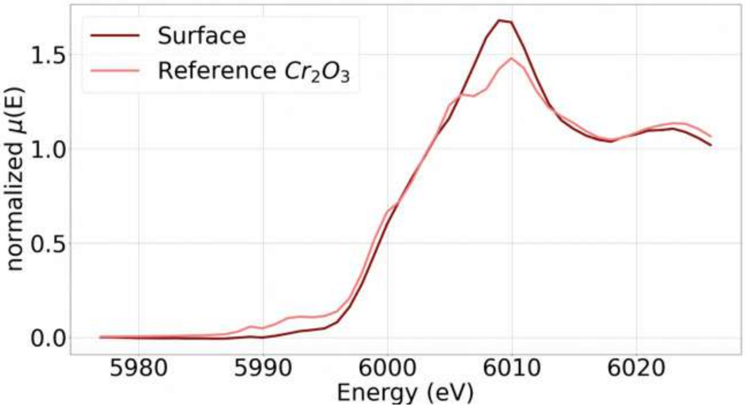

Fig. 4.12: Comparison of the normalized XANES spectrum of a surface layer of 600 °C for 10 minutes sample with the reference spectrum of Cr_2O_3.

The XANES spectrum obtained from the surface layer of the 600 °C for 10 minutes sample shows remarkable similarity to the reference Cr_2O_3 spectrum, as shown in Figure 4.12. It seems that half an hour of exposure per spot was not enough to capture these subtle features in detail due to the thin surface layer. Despite these differences, the overall spectral characteristics are broadly consistent with those of the reference spectrum.

4.2.2 800 °C for 1 hour exposed sample

The next phase of the investigation focused on a compositionally complex CrCoNi exposed to a temperature of 800 °C for 1 hour. To ensure consistency in the experimental approach, this sample was analyzed using half an hour excited for each 1 eV increment within the 5975-6025 eV range. As expected, one hour exposed sample at 800 °C exhibits a similar oxidation state to 600 °C sample. However, the layer thickness is to be more pronounced as a result of both the longer exposure time and the higher temperature.

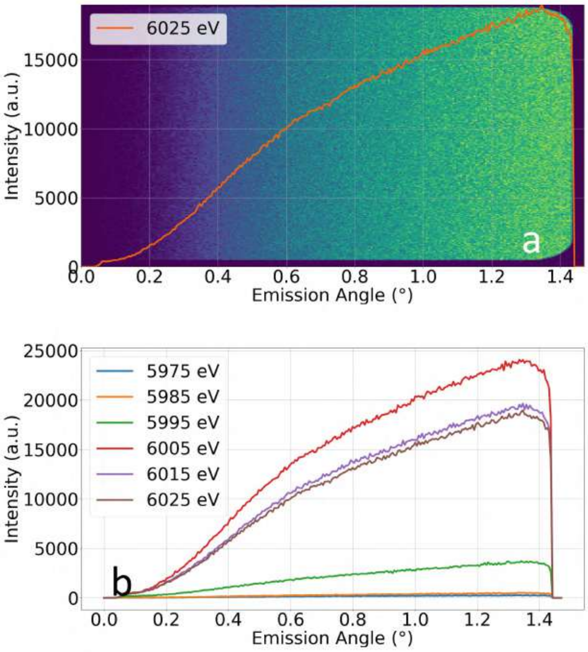

Fig. 4.13: a) Angular intensity profile of the 800 °C for 1 hour sample at 6025 eV. b) Collection of angular intensity profiles of the 800 °C for 1 hour sample as a function of excitation energy.

Figure 4.13(a) shows the angular intensity profile of the CrCoNi exposed to 800 °C for 1 hour. In this case, the angular intensity profile shows no variation at 6025 eV, in contrast to the observations made in CrCoNi 600 °C for 10 minutes sample. The shape of the angular intensity profiles shows that the thickness of the investigated layer was greater than that of the previous surface layer on the 600 °C for 10 minutes exposed sample. To generate the XANES spectra, angular intensity profiles were collected as a function of excitation energy. Some of the collected angular intensity profiles are shown in Figure 4.13(b).

Despite the lack of recognizable layers, further analysis of the sample was continued. Rather than using NMF analysis, which is typically effective for multi-layer structures, a more direct approach was used for this sample. Given the homogeneity of the layer, the intensities at all emission angles in each angular intensity profile were summed to obtain the XANES spectrum.

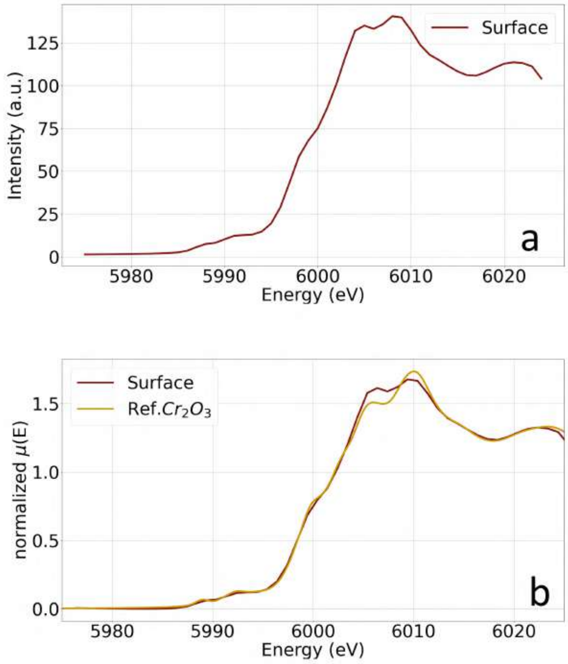

Fig. 4.14: (a) The derived spectrum from cumulative intensities at all emission angles. (b) A comparison of the normalized XANES spectrum of the 800 °C for 1 hour sample with the reference Cr_2O_3 spectrum

Figure 4.14(a) shows the XANES spectrum of the CrCoNi sample exposed at 800 °C for 1 hour. There are similarities between this spectrum and the oxide layer in the sample exposed at 600 °C for 10 minutes. To validate these similarities, this spectrum was compared with the Cr_2O_3 reference spectrum after normalization.

Figure 4.14(b) shows the normalized spectrum of the 800 °C for 1 hour exposed sample together with the Cr_2O_3 reference spectrum and shows remarkable similarities. The spectrum obtained from the 800 °C for 1 hour sample is more similar to Cr_2O_3 than the surface layer of the 600 °C for 10 minutes sample. This greater similarity can be attributed to the thicker oxide layer formed on the CrCoNi sample after exposure at 800 °C for 1 hour. The increased layer thickness caused the substrate signal to be trapped within the oxide layer, resulting in the oxide layer signal dominating at all emission angles. Thus eliminated the inconsistencies observed in the signal regions of the 600 °C for 10 minutes sample.

4.3 Angular intensity profile dynamics

The comprehensive study of the oxidation characteristics of compositionally complex CrCoNi alloy samples at 600 °C and 800 °C raises the question: how different are the angular intensity profiles of these exposed specimens compared to the unexposed alloy? The aim is to clarify the influence of layer growth on the angular intensity profiles. This demonstrates that GEXANES analysis can be used to study the initial stages and growth of oxide layers in the environment in which they are formed.

Three different angular intensity profiles are shown in Figure 4.15. Figure 4.15(a) corresponds to the unexposed alloy and shows a homogeneous profile indicative of the substrate only, with no additional layers. Figure 4.15(b) shows the profile for the sample exposed to 600 °C for 10 minutes, revealing the presence of both the oxide layer and the substrate emissions, as previously discussed. The profile in Figure 4.15(c) represents the sample exposed at 800 °C for 1 hour, which shows a uniform profile without any layer sign. Taken together, these profiles demonstrate the ability to monitor the oxidation process through changes in the angular intensity profiles, thus providing insight into the formation of new layers.

This study highlights the potential of using angular intensity profiles for in-situ analysis. By tracking the evolution of these profiles under varying conditions, the effectiveness of this approach in monitoring real-time oxidation dynamics is highlighted.

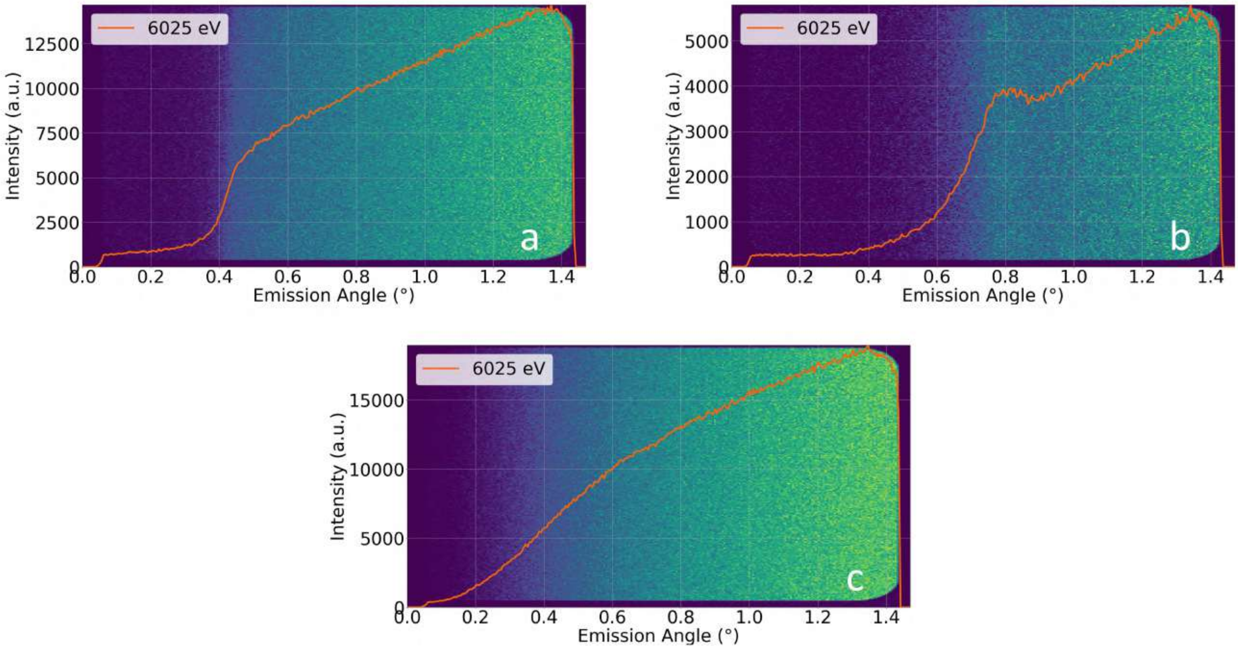

Fig. 4.15:
a) Angular intensity profile of the unexposed CrCoNi sample at 6025 eV, b) Angular intensity profiles of the CrCoNi sample exposed at 600 °C for 10 minutes, c) Angular intensity profiles of the CrCoNi sample exposed at 800 °C for 1 hour.

The analysis of selected samples by GEXANES allowed the evaluation of initial hypotheses regarding the analytical capabilities of this method. The distinctive features observed in the reference, 600 °C for 10 minutes and 800 °C for 1 hour samples and the dynamics of the angular intensity profiles provide valuable insights into the evolution of the oxidation states. These results confirm the effectiveness of GEXANES in analyzing such layered structures and suggest its applicability for real-time in-situ studies. One challenge, however, is the time-intensive nature of the process, especially at shallow angles of detection; the acquisition of a XANES spectrum for a single sample can take approximately one day. This long duration limits its suitability for synchrotron facilities, highlighting the need for method optimization to improve its practicality.

4.4 Optimization of the method

During the proof-of-concept phase, GEXANES showed great promise for the analysis of layered materials. However, the length of time required for spectrum acquisition in the current methodology was a notable challenge. This chapter focuses on optimizing the methodology to improve time efficiency while maintaining data quality. To meet this challenge, Bayesian optimization (BO) was applied to the GEXANES data collection process.

Optimization experiments specifically targeted the reference sample. Spectra were obtained from the 5975-6035 eV energy range. The following sections present the results of the BO-informed experiments using exposure times of 5 minutes and 1 minute per spot and compare these results to the reference sample data in the Proof of Concept section.

The decision to experiment with a 5-minute exposure represented a conservative approach aimed at significantly reducing the traditional 20-minute standard while maintaining comparable data quality.

This decision was based on quantitative analysis: the XANES spectrum from the surface layer typically achieves a total total count of $2x10^6$ during a 20-minute exposure. It was anticipated that reducing the exposure to 5 minutes would give a total count of approximately $5x10^5$ for the surface layer. Although this total count is below the accepted standard for XANES spectra (10^6), the integration of a kernel function is designed to effectively compensate for the increased noise, and this is a good basis for testing the kernel function.

In addition, the choice of a 1-minute exposure was a more exploratory method to test the limits of efficiency and assess the impact on data integrity at drastically reduced exposure times. In this context, the role of the kernel function becomes even more crucial, as it is the key to mitigating the noise challenges associated with such short exposures. The study aims to determine the minimum feasible exposure time that yields scientifically valid results, thereby pushing the limits of current capabilities in XANES spectroscopy.

4.4.1 Bayesian Optimization with 5-minute exposure

The BO-informed method uses an intelligent selection of the energy points for measurement, optimizing the energy scanning process down to 25 points. For obtaining the desired energy values, the monochromator angle is aligned with the angle corresponding to the energy value sent from the optimization algorithm. The measurement process is initiated upon aligning the monochromator. Data obtained from the BO-informed method are compiled into a data set, with the process continuing until a specific stopping criterion, set at 25 measurement points, is reached. The rationale behind setting this criterion in the BO-informed experiments is discussed in the following paragraphs. During the optimization process, cumulative intensities from all emission angles are incorporated into the algorithm with the aim of improving count statistics. This technique, similar to the analytical approach for the 800 °C sample, is designed to support statistical robustness and enhance the algorithm's prediction accuracy.

Subsequent sections will present an exploration of four cumulative figures, each containing a pair of closely related graphics, resulting in eight different visual representations. Within each pair:

- The first graph displays the Gaussian Process (GP) mean estimate alongside results from the specific sampling points selected during the BO-informed experiment and the standard scan. This graph also includes the 95% confidence interval, offering an additional statistical perspective on the reliability of the estimates. The representation provides a clear comparative overview, highlighting the efficiency and accuracy of the BO-informed experiment over the traditional procedure.
- The second graph provides an in-depth look at the internal dynamics of the optimization method by visualizing the interaction between the mean and variance predictions of the GP and the UCB function.

These paired visualizations aim to offer a comprehensive understanding of the method's evolution and precision.

A crucial initial step in the BO process is the construction of a 'prior function', which represents a statistical model of the initial understanding before iterative processing. To establish this prior function, measurements are taken at seven equidistant energy points covering the defined energy range. This methodology is graphically represented in Figure 4.16(a).

Figure 4.16(a) features the orange curve as the mean function derived from the GP model, formulated based on the measurements from the initial seven energy points. This curve acts as a probabilistic representation of the function, with the surrounding grey area indicating the ± 95% confidence interval, quantifying the uncertainty in the model's predictions.

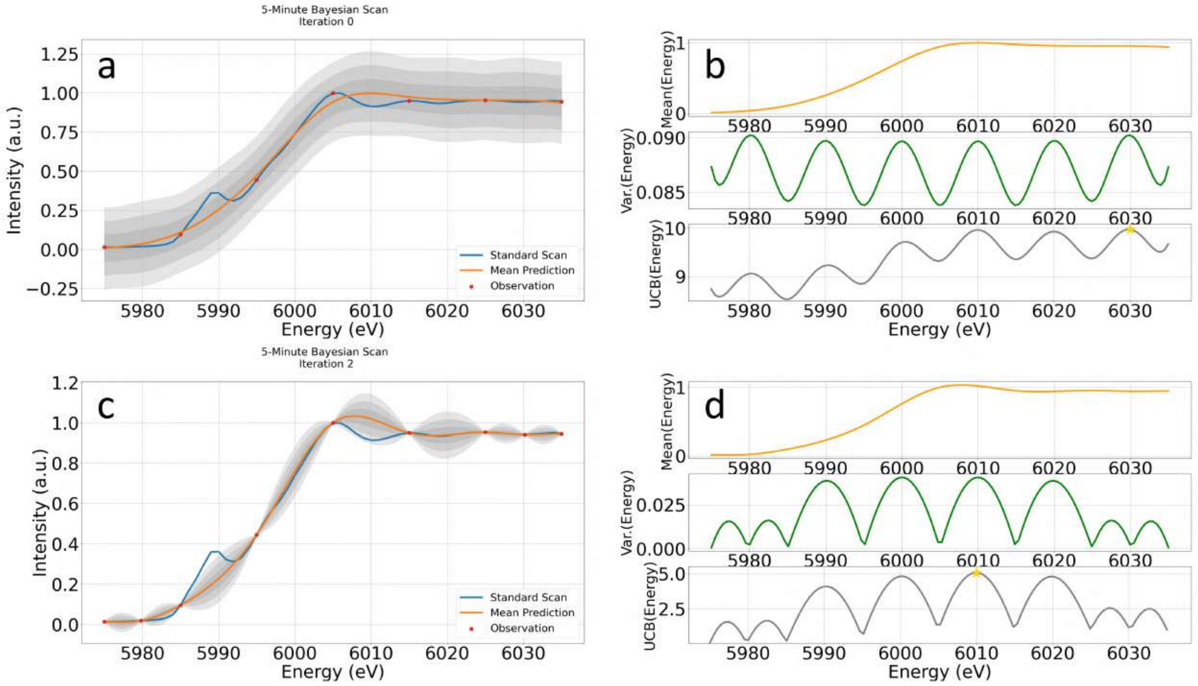

Fig. 4.16: Bayesian Optimization Iterations and Gaussian Process Model Development: (a) Initial setup with seven evenly distributed energy points used to establish the prior function, represented by the orange curve (mean function). The grey area showcases the ± 95% confidence interval around the predicted mean. (b) Displays the mean function at the top, the variance function in the middle, and the UCB function at the bottom. The gold star on the UCB plot indicates the next chosen sampling point. (c) Progression of the Gaussian Process model two iterations post-initial setup. The orange curve now incorporates the new measurements, with the grey area representing the adjusted ± 95% confidence interval. (d) Updated mean, variance, and UCB functions after two iterations. The gold star on the UCB plot signifies the upcoming sampling point, exemplifying the algorithm's intelligent point selection, with the next measurement point indicated as 6010 eV. The reduction in the UCB values and the confidence interval demonstrates the diminishing uncertainty between measured points, highlighting improved prediction accuracy.

In Figure 4.16(b), the top section of the graph illustrates the mean function of the GP model. Directly beneath it lies the variance function, and at the bottom of the graph, the Upper Confidence Bound (UCB) function is displayed. The gold star, positioned on the

UCB graph near 6030eV, indicates the next sampling point, suggesting that the upcoming measurement will occur at this energy level, with the GP model being updated accordingly.

Figures 4.16(c) and 4.16(d) detail the GP model's evolution through two subsequent iterations. In Figure 4.16(c), the mean function now includes recent measurements, highlighting the model's capacity for adaptation. Concurrently, the grey area, denoting the updated 95% confidence interval, has become narrower, reflecting a reduction in forecast uncertainty and underscoring the iterative refinement characteristic of BO.

Figure 4.16(d) presents the revised mean, variance, and UCB functions. The gold star on the UCB plot, indicating the next sampling point, is set at 6010 eV, exemplifying the algorithm's intelligent selection mechanism. The UCB function, after two iterations, shows a notable decrease in values post-measurement, indicative of diminished uncertainty among measured points. This decrease and the consequent narrowing of the confidence interval underscore an enhanced prediction accuracy of the GP model following the inclusion of new data.

Figure 4.17 delves deeper into the model's progressive iterations. Figures 4.17(a) and 4.17(b) depict the third iteration following the first seven measurements, while Figures 4.17(c) and 4.17(d) represent the fourth iteration. In particular, Figure 4.17(a) shows how things have changed since the second iteration and the measurement at 6010 eV, where it is clear that the confidence interval has grown. This widening is due to more uncertainty between the points, as shown in Figure 4.17(b). It narrowed at first after two iterations but grew again after the 6010 eV measurement. This dynamic causes the model to re-calibrate its predictions, leading to a broader confidence interval. Following the third iteration, the peak of the UCB function, identified at 6020 eV, signifies the subsequent measurement point.

In Figures 4.17(c) and 4.17(d), the impact of the 6020 eV measurement is evident. A reduction in uncertainty between points is observed, emphasizing the algorithm's adaptability and enhanced predictive capability due to iterative tuning and data incorporation. The UCB function's peak in Figure 4.17(d), located at 6000 eV, identifies the next targeted measurement point.

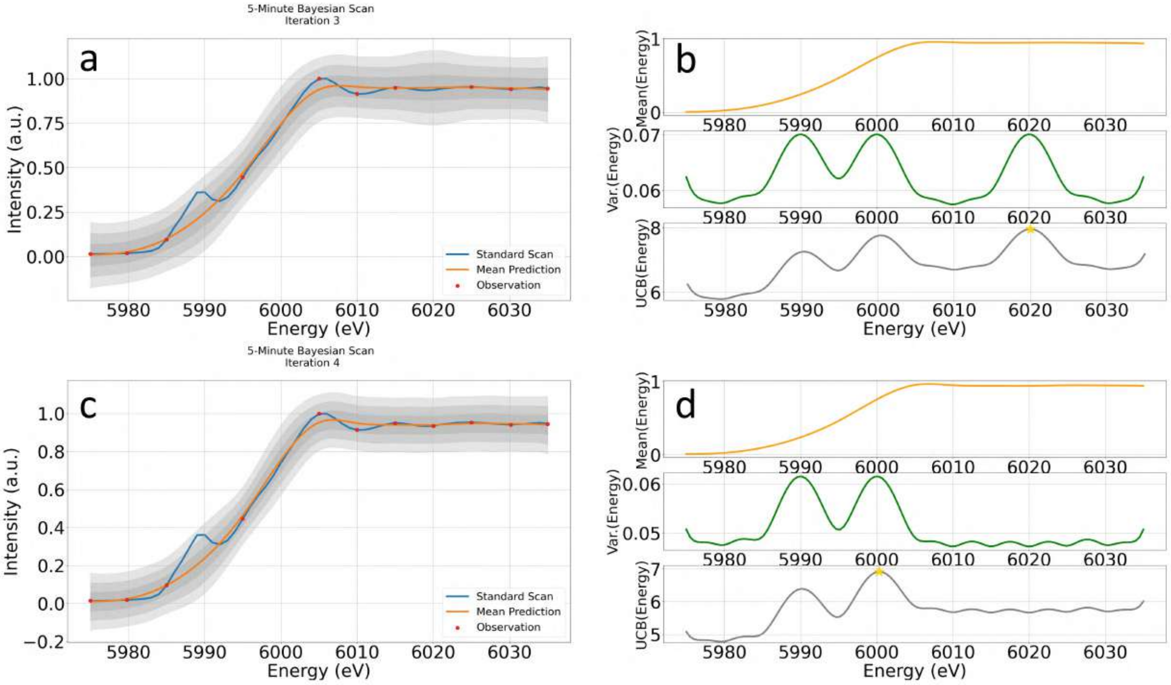

Fig. 4.17: Refinement of the Gaussian Process Model during Iterations 3th and 4th: (a) The results were obtained after measuring at 6010 eV during the second iteration. (b) The details of the evolving mean, variance, and UCB functions for this iteration are presented. The gold star on the UCB plot indicates the next sampling point at 6020 eV. (c) The results were obtained after measuring at 6020 eV for the third iteration. (d) Updated mean, variance, and UCB functions. The gold star in the UCB plot indicates that the algorithm's next measurement target is at 6000 eV.

In the BO-informed experiment, subsequent choices are influenced by each measurement, reflecting a progression from initial exploration to more informed decision-making. Data points accumulate over time, and the GP model is continuously updated, providing a clearer understanding of the dynamics of the black box function being explored.

The focus shifts from early iterations to the final stages of the scanning process, with an emphasis on the results of the 15th and 16th iterations following the baseline seven points. Figure 4.18 displays the outcomes of the final stages of the BO process. Results from the 15th iteration, subsequent to the baseline seven-point measurement, are shown in Figures 4.18(a) and 4.18(b). Figures 4.18(c) and 4.18(d) demonstrate the improvements achieved in the 16th iteration. Two regions with widened confidence intervals are identified in Figure 4.18(c). The UCB function in Figure 4.18(d) confirms that these regions are likely to guide future measurements. A significant reduction in uncertainty is evidenced,

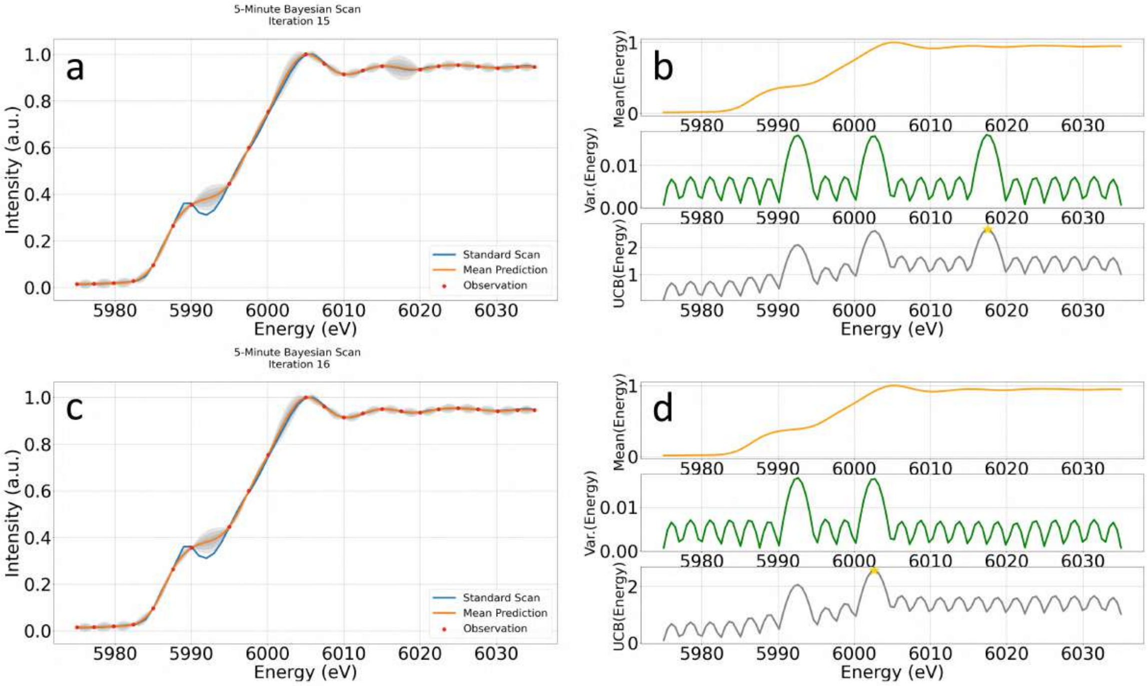

Fig. 4.18: Refinement of the Gaussian Process Model during Iterations 15th and 16th: (a) Results post the 15th iteration. (b) Details of the evolving mean, variance, and UCB functions for this iteration. The gold star on the UCB plot indicates the next sampling point at around 6018 eV. (c) The results were obtained after the 16th iteration, which measured around 6018 eV. (d) Updated mean, variance, and UCB functions. The gold star in the UCB plot suggests the next measurement target by the algorithm is around 6003 eV.

with the uncertainty interval between peaks, initially at 0.06 during the 4th iteration, decreasing by a factor of 4 to 0.015 by the end of the 16th iteration.

Figure 4.19 presents information from the last two steps, capturing the concluding point of the iterative process. After the 16th iteration establishes the next measurement point at approximately 6003 eV, the highest-confidence field range post-measurement centers around 5992 eV, as shown in the figure. This observation prompts the optimization algorithm to select this energy value for subsequent measurements.

Figures 4.19(a) and 4.19(b) further illustrate the evolution of the events. Figure 4.19(c) shows the new mean function of the Gaussian process model after the measurement at 5992 eV. Figure 4.19(d), on the other hand, shows that the inter-point uncertainty has gone down a lot, from about 0.09 after the first seven-point measurement to 0.005 after 18 iterative steps. This represents a reduction in uncertainty of approximately a factor of 18.

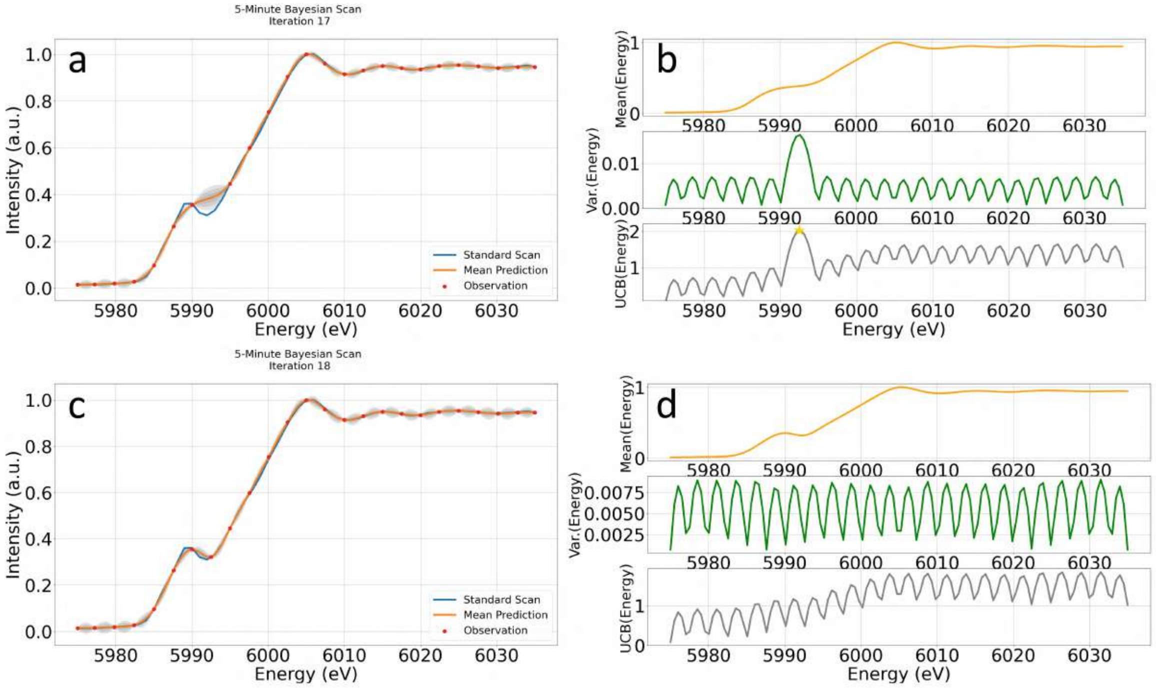

Fig. 4.19: Refinement of the Gaussian Process Model during Iterations 17th and 18th: (a) Results post the 17th iteration. (b) Details of the evolving mean, variance, and UCB functions for this iteration. The gold star on the UCB plot indicates the next sampling point at around 5992 eV. (c) The results were obtained after the 18th iteration, which involved measuring around 5992 eV. (d) Updated mean, variance, and UCB functions.

Additionally, the variance plot reveals a significant transformation in previously sharp peaks, indicative of uncertainty between points. These peaks now exhibit a more consistent appearance. This reduction in uncertainty, along with the newfound uniformity in the variance function, indicates that the desired efficiency in optimization has been achieved. As a result, the iterative process is terminated after the 18th iteration, and a comprehensive measurement at 25 different points is obtained.

In BO-informed experiments, intensities from all emission angles are included to guide the scanning process. However, this alone is not sufficient to detect two different layers of the reference sample. To address this, NMF was applied to the data set obtained from the BO-informed experiment. Figure 4.20 provides a detailed visualization: Figure 4.20(a) shows the 3D dataset that was used for the NMF analysis. Figures 4.20(b) and 4.20(c) show the angular intensity profile and XANES spectra of the different layers. The observations from these 25 points closely match those from the standard scan, albeit at lower resolution. To get a better picture, the same Gaussian process model that is at the heart of the BO process is used to combine the 25-point XANES spectra from the NMF analysis of both layers into a 120-point spectrum.

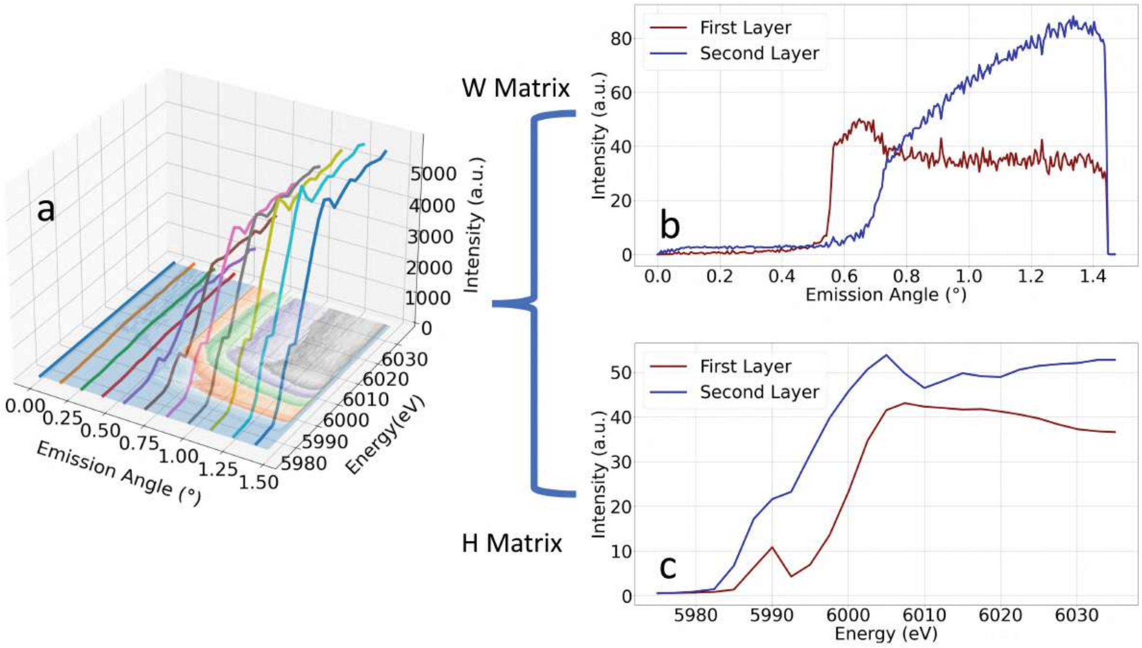

Fig. 4.20: (a) A 3D visualization of the dataset applied to NMF analysis. (b-c) Depict the angular intensity profile and corresponding XANES spectra of the extracted layers.

Figure 4.21 delves into the enhanced resolution spectra derived from the Gaussian Process model. In Figure 4.21(a), the 120-point XANES spectra for the two distinct layers of the reference sample are presented. In Figure 4.21(b), normalized spectra are displayed, facilitating a clearer comparative analysis between the layers. Initial observations suggest that the data align closely with those obtained from the standard scan.

A direct comparison of the normalized XANES spectra from both layers was performed to evaluate the sensitivity and efficiency of the BO-informed experiment compared to the standard experiment. In Figure 4.22, the similarity of these spectra is visually confirmed by comparing spectra from different layers, with a graph at the bottom quantifying the percentage difference between the points.

These values emphasize the robustness of the BO-informed experiment in producing results comparable to the standard experiment but with greater efficiency. This underlines

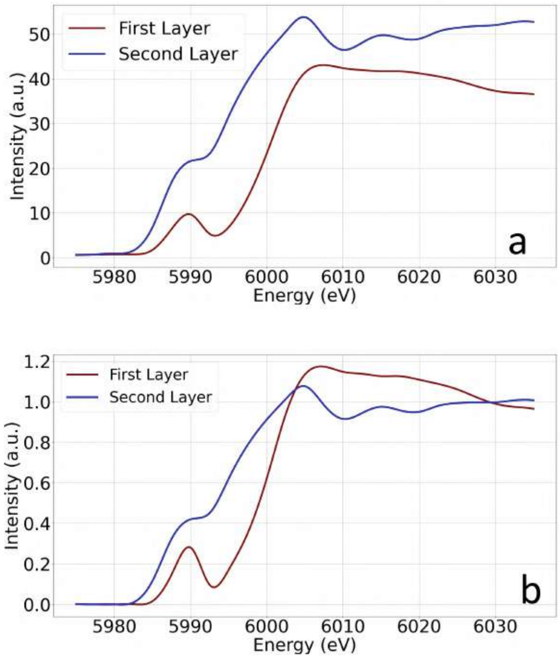

Fig. 4.21: (a) shows the 120-point XANES spectra derived from two distinct layers. (b) the normalized spectra permit clearer distinctions and comparative examinations between layers.

the potential of the BO-informed experiment as a promising analytical tool capable of reducing experimental time without compromising the accuracy of the results.

However, some discrepancies in the results for the first layer suggest that there is room for further improvements in the Bayesian approach. In particular, the local maxima in the pre-peak region were not optimally captured. To improve the performance of the algorithm, a two-layer approach can be implemented. First, NMF analysis would be applied to the angular intensity profile to identify the emission angles relevant to each layer. With this information, the optimization process could be refined to focus specifically on the range of angles associated with the target layer. This layer-specific optimization is expected to reduce the discrepancies observed in the current results.

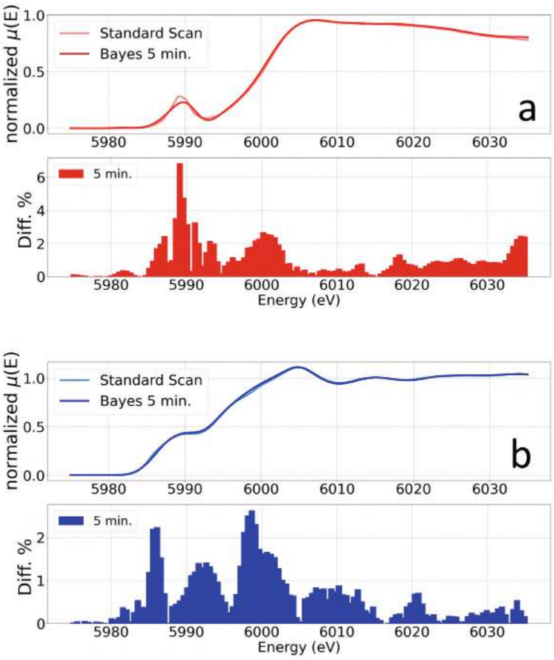

Fig. 4.22: Comparative Analysis of XANES Spectra Between Standard and Bayesian scans.

4.4.2 Bayesian Optimization with 1-minute exposure

The aim of implementing a faster Bayesian optimization approach was to determine whether meaningful data could be obtained from significantly reduced measurement times. Taking advantage of the efficiency of the Bayesian process, an optimization was carried out using 1-minute measurements per point to test its effectiveness.

This experiment maintained a fast iteration cycle similar to the previous optimization process of 5-minute per point. An initial set of 7 equally spaced data points was established, which formed the basis for the subsequent 18 iterations. This shorter measurement time challenges the efficiency and adaptability of BO-informed experiments.

Figure 4.23 provides key insights into the effectiveness of the faster Bayesian optimization. Figure 4.23(a) shows the spectra obtained from a standard experiment, the 5-minutes and the fast 1-minute BO-informed experiments, covering all emission angles before normalization. The first comparison shows a remarkable similarity between these spectra, highlighting the potential of the accelerated BO-informed experiment.

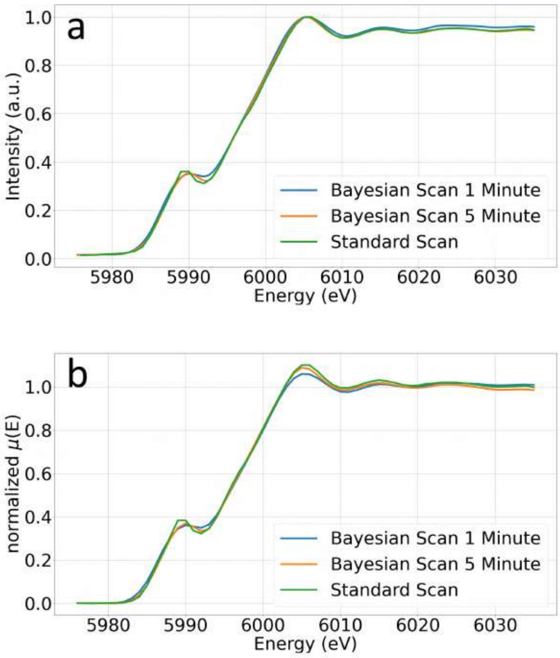

Fig. 4.23: (a) XANES spectra from all emission angles, derived from standard, Bayesian 5-minute, and Bayesian 1-minute scans without normalization. (b) Corresponding normalized XANES spectra.

Figure 4.23(b) shows the normalized data of the sum of all emission angles for standard, 1-minute, and 5-minute BO-informed experiments. The 1-minute Bayesian scan shows slight deviations, especially around the two distinct shoulder regions. Nevertheless, the overall agreement is remarkable.

A more detailed quantitative analysis is presented in Figure 4.24, using metrics such as root mean square error (RMSE) and percentage difference analysis. The relative accuracy and possible differences between the different methods are shown by these metrics. They give a full picture of how well the BO-informed experiment worked with different time constraints.

For the 5-minute Bayesian method, the RMSE was 0.011, showing commendable accuracy compared to the standard method. The maximum percentage difference was 3.1%, indicating that the highest deviations were kept under control. Impressively, the average percentage difference was a modest 0.85%, reinforcing the reliability of this 5-minute Bayesian approach.

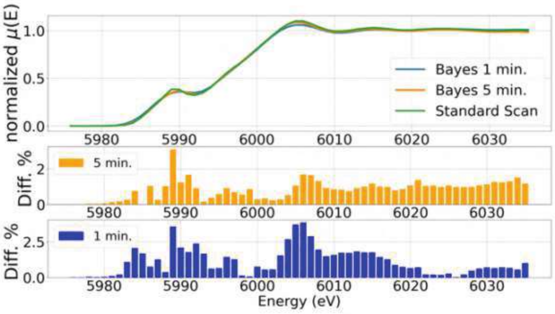

Fig. 4.24: Difference analysis of XANES spectra from all emission angles, derived from Standard, Bayesian 5-Minute scans after normalization.

On the other hand, the quick 1-minute Bayesian method showed some differences. The RMSE was 0.016, indicating a noticeable but expected trade-off between time efficiency and precision. Although the maximum percentage difference increased slightly to 3.84%, this limited increase should be appreciated given the drastic reduction in measurement time. The average percentage difference stabilized at 1.1%, demonstrating the ability of the method to maintain remarkable accuracy despite its short duration.

Together, these metrics provide valuable insights into the efficiencies and trade-offs inherent in both Bayesian methods and offer a clear perspective on their respective strengths and challenges.

Adopting the methodology from the 5-minute Bayesian case, an analogous approach was applied to the 1-minute Bayesian optimization. The XANES spectra were taken from the sped-up 1-minute Bayesian scans and then decomposed in a planned way using NMF. The goal of this approach was to identify and decompose the XANES profiles corresponding to individual layers within the reference sample.

To enhance the spectral resolution, the Gaussian process model was reintegrated. This involved inputting 25-point XANES spectra, derived from the NMF analysis of both layers, into the model. The model was then tasked with interpolating for each distinct layer, yielding a detailed 120-point spectrum. This procedure mirrored that employed in the 5-minute BO-informed experiment.

A comparison of the normalized spectra of the two different layers of the reference sample obtained with 1-minute, 5-minute, and standard scans is shown in Figures 4.25(a) and 4.25(b). Quantitative analysis was again applied to all results.

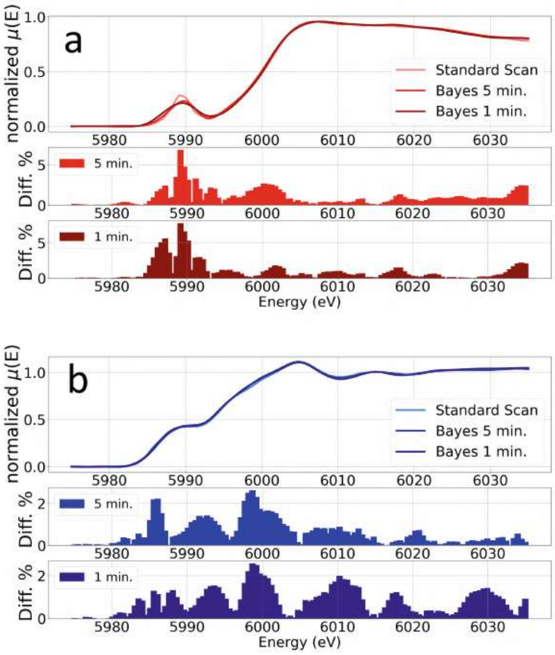

Fig. 4.25: Difference analysis of XANES spectra from all emission angles, derived from Standard, Bayesian 5-Minute, and Bayesian 1-Minute scans after normalization.

The comparison of normalized spectra from two distinct layers of the reference sample is elucidated through quantitative metrics. These metrics significantly enhance comprehension of results obtained from experiments informed by BO.

For the first layer:

- Using the 1-minute Bayesian optimization, the root mean square error (RMSE) was 0.016. The maximum percentage difference, indicating the peak deviation, was at 7.78%, while the mean percentage difference was 1%.
- In contrast, the 5-minute Bayesian method recorded a slightly lower RMSE of 0.0135. The highest deviation was measured at 6.85%, and the mean percentage difference with the 1-minute approach standing at 1%.

For the second layer:

- With the 1-minute Bayesian method, the RMSE was an impressive 0.011. The maximum deviation was slightly less pronounced at 2.56%, and the mean percentage difference was just 0.8%.

- The 5-minute Bayesian approach managed even tighter metrics for this layer with an RMSE of 0.009. The peak deviation was a tad higher at 2.63%, but the mean percentage difference was slightly lower at 0.6%.

The apparent minor trade-offs between speed and precision underscore the versatility of the BO-informed experiment, which produces impressive data quality even under significant time constraints.

An additional experiment was performed to determine whether the observed close alignment was due to BO or GP. Figure 4.26(a) presents a comparison of normalized XANES spectra from the first layer of the reference sample, based on the exposure duration per point of the standard experiment, with data collected from 60 equidistant points as previously mentioned. The standard experiment, with an exposure of 1 minute per point, captured the initial part of the spectrum (pre-peak region at 5975–6005 eV) but exhibited significant differences from the 20 minutes per point standard experiment in the region following the absorption edge (post-edge at 6005-6035 eV). To quantify these differences, the root mean square error (RMSE) was utilized. The RMSE between the 1-minute and 20-minute per point standard experiments was 0.0157 a.u. eV^{-1}. Additionally, the RMSE between the prediction obtained from the GP model, trained with 25 points from the 1 minute BO-informed experiment, and the 20 minutes per point standard experiment in the post-edge region was 0.005 a.u. eV^{-1}.

Figure 4.26(b) illustrates a comparison between two experimental procedures: a 1-minute per point standard experiment and a 1-minute per point BO-informed experiment. This comparison aimed to determine whether the close alignment of the BO-informed experiment's results with those of the established 20-minute per point standard experiment was solely due to the application of a Gaussian Process (GP) or an inherent aspect of the BO-informed methodology. As part of the 1-minute per point standard experiment, 60 points from the standard experiment were used to train a GP model and see how well it dealt with noise and described the data. However, even after applying the GP to the 1-minute per point standard experiment data, the features of the curve did not match those from the 20-minute per point standard experiment, while the 1-minute per point BO-informed experiment did. The RMSE calculated between the 20-minute per point

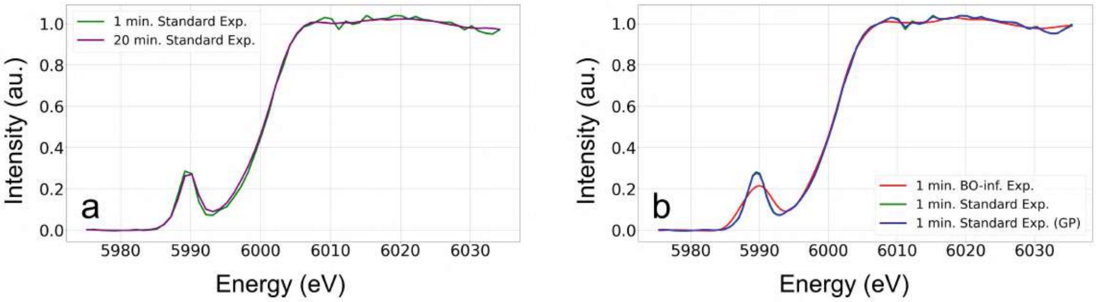

Fig. 4.26: (a) The comparison of normalized XANES spectra from the first layer of the reference sample for standard experiments conducted over a duration of 1-minute and 20-minute per point, with data collected from 60 equidistant points. (b) A comparative analysis between a 1-minute per point BO-informed experiment, a 1-minute per point standard experiment, and the prediction obtained from a GP model trained with 60 points from the 1-minute per point standard experiment.

standard experiment and the prediction obtained from the GP model, trained with 60 points from the 1-minute per point standard experiment, was 0.0124 a.u. eV^{-1}, indicating that while the GP contributes to data interpretation, it does not fully account for the features observed in the BO-informed experiment. The BO-informed approach is more effective at managing noise and preserving the features of the data from the 20-minute per point standard experiment.

Summarizing the results of this subsection, it is clear that BO-informed experiments offer a transformative approach to XANES analysis, significantly improving the efficiency of measurements without drastically reducing accuracy. Both the 5-minute and 1-minute fast methods give commendable results and the differences in accuracy remain small given the significant time savings. The effectiveness of integrating NMF with the Gaussian process model will further highlight the versatility and robustness of the BO-informed experiment.

Furthermore, while both time frames offer their own advantages and potential for improvement, the overarching benefit is clear: reduced measurement times, cost savings, and accelerated results. The future of XANES research is moving toward more agile yet reliable methods, with Bayesian optimization leading the way.

Chapter 5

Conclusion & Outlook

This thesis has advanced the field of material science by addressing two crucial questions: how to provide depth-resolved insights into layered materials under non-destructive and ambient conditions, and how to enhance the efficiency of spectroscopic data acquisition through machine learning techniques.

To address the first question, this work combines X-ray absorption near-edge structure spectroscopy (XANES) and grazing emission X-ray fluorescence spectroscopy (GEXRF) into grazing emission XANES (GEXANES) to develop a novel approach for analyzing layered materials. Traditional methods such as X-ray photoelectron spectroscopy (XPS), secondary ion mass spectrometry (SIMS), and Meitner-Auger electron spectroscopy (M-AES) have played critical roles in surface analysis. However, their limitations—especially the need for high vacuum conditions and restricted depth profiling—necessitated the exploration of innovative alternatives. The combination of XANES and GEXRF emerged as a significant alternative, operating under more versatile conditions and offering enhanced capabilities for in-situ measurements.

The effectiveness of GEXANES was initially validated using a reference sample. This technique allows for the extraction of information from multiple layers within a single experiment. Theoretical calculations have assisted in establishing the optimal experimental setup and have provided insights into the potential information depth that can be obtained. The analyses of the chemical states of the layers under ambient conditions for both reference samples and CrCoNi samples have been thoroughly conducted. Identifying angular intensity profiles as indicators of layer evolution has opened new avenues for in-situ studies. By observing additional layers in the angular intensity profiles, early stages of the oxidation process can be analyzed. The use of advanced pnCCD detectors can enhance these studies by enabling the simultaneous monitoring of layer evolution from different atoms. This represents a significant advancement in analytical chemistry, as the pnCCD detector allows for the capture of distinct angular intensity profiles of various atoms in a single measurement.

After GEXANES was successfully used to answer the second research question, this study looked into how machine learning, especially active learning techniques, could be used to make the process of collecting spectroscopic data more efficient. To optimize the experimental process, a pipeline was first established that allows the active learning algorithm to autonomously control the entire experiment. This pipeline evaluates data in real time.

The integration of machine learning through active learning techniques, such as Bayesian Optimization (BO), has significantly enhanced the efficiency of GEXANES data acquisition. Given the extended measurement times typically required in the high-demand and resource-intensive synchrotron facilities, the application of BO has proven to be crucial. This approach enabled substantial reductions in data acquisition times, reducing what were once lengthy sessions (20 hours) to quick 125 minutes and even 25 minutes sessions without sacrificing significant data quality.

The benefits of this optimization go beyond just improving efficiency. The entire research methodology has been revolutionized, with reduced measurement times indicating significant cost savings and enabling real-time decision-making and thereby improving overall operational effectiveness. These advancements demonstrate the transformative potential of machine learning in optimizing scientific research processes, specifically by tailoring data collection strategies to be both cost-effective and time efficient.

The integration of BO not only increases the applicability of GEXANES but also has important implications for the development of more efficient laboratory-based XAFS instruments. This transformative approach could revolutionize the way these instruments are used in a variety of scientific fields, particularly by enabling the rapid analysis of large numbers of samples.

However, this research is just a preliminary step. The potential for further optimization is seen, particularly through the integration of additional active learning layers with machine learning models. This approach, based on the use of a well-defined database, promises faster analyses by exploiting the knowledge gained from previous measurements.

In conclusion, this work has successfully addressed its key research questions, demonstrating the continuing evolution of analytical methods in materials science. By combining XANES and GEXRF, it has provided a powerful tool for depth-resolved analysis of layered materials under ambient conditions. Furthermore, the integration of machine learning techniques has significantly enhanced the efficiency of data acquisition, paving the way for more productive and cost-effective research in materials science. The future is expected to bring further innovations that will unravel the complexity of materials at the atomic and molecular levels, building upon the foundations laid by this research.

Bibliography

[1] M. J. Mirshojaeian Hosseini and R. A. Nawrocki. “A Review of the Progress of Thin-Film Transistors and Their Technologies for Flexible Electronics”. In: *Micromachines* 12.6 (2021). ISSN: 2072-666X. DOI: `10.3390/mi12060655`. URL: `https://www.mdpi.com/2072-666X/12/6/655`.

[2] M. A. Green. “Thin-film solar cells: review of materials, technologies and commercial status”. In: *Journal of Materials Science: Materials in Electronics* 18 (2007), pp. 15–19.

[3] K. Gerhardus, V. Jeff, T. Neil, M. Oliver, G. Melissa, and P. Joe. *International Measures of Prevention, Application, and Economics of Corrosion Technologies Study*. Mar. 2016.

[4] C. Stephan-Scherb, W. Schulz, M. Schneider, S. Karafiludis, and G. Laplanche. “High-temperature oxidation in dry and humid atmospheres of the equiatomic CrMnFeCoNi and CrCoNi high-and medium-entropy alloys”. In: *Oxidation of Metals* 95 (2021), pp. 105–133.

[5] A. Ayyagari, V. Hasannaeimi, H. S. Grewal, H. Arora, and S. Mukherjee. “Corrosion, erosion and wear behavior of complex concentrated alloys: a review”. In: *Metals* 8.8 (2018), p. 603.

[6] S. Praveen and H. S. Kim. “High-entropy alloys: potential candidates for high-temperature applications–an overview”. In: *Advanced Engineering Materials* 20.1 (2018), p. 1700645.

[7] J. Chen, X. Zhou, W. Wang, B. Liu, Y. Lv, W. Yang, D. Xu, and Y. Liu. “A review on fundamental of high entropy alloys with promising high–temperature properties”. In: *Journal of Alloys and Compounds* 760 (2018), pp. 15–30.

[8] M. Dada, P. Popoola, S. Adeosun, and N. Mathe. “High entropy alloys for aerospace applications”. In: *Aerodynamics*. IntechOpen, 2019.

[9] Z. Yang, P.-F. Sun, X. Li, B. Gan, L. Wang, X. Song, H.-D. Park, and C. Y. Tang. “A critical review on thin-film nanocomposite membranes with interlayered structure: mechanisms, recent developments, and environmental applications”. In: *Environmental science & technology* 54.24 (2020), pp. 15563–15583.

[10] S. Chung, K. Cho, and T. Lee. “Recent progress in inkjet-printed thin-film transistors”. In: *Advanced science* 6.6 (2019), p. 1801445.

[11] G. Lei, C. Lou, X. Liu, J. Xie, Z. Li, W. Zheng, and J. Zhang. “Thin films of tungsten oxide materials for advanced gas sensors”. In: *Sensors and Actuators B: Chemical* 341 (2021), p. 129996.

[12] J. W. Park, B. H. Kang, and H. J. Kim. “A review of low-temperature solution-processed metal oxide thin-film transistors for flexible electronics”. In: *Advanced Functional Materials* 30.20 (2020), p. 1904632.

[13] S. Moitzheim, B. Put, and P. M. Vereecken. “Advances in 3D thin-film Li-ion batteries”. In: *Advanced Materials Interfaces* 6.15 (2019), p. 1900805.

[14] K. Vijayan, S. Vijayachamundeeswari, K. Sivaperuman, N. Ahsan, T. Logu, and Y. Okada. “A review on advancements, challenges, and prospective of copper and non-copper based thin-film solar cells using facile spray pyrolysis technique”. In: *Solar Energy* 234 (2022), pp. 81–102.

[15] D. N. G. Krishna and J. Philip. “Review on surface-characterization applications of X-ray photoelectron spectroscopy (XPS): Recent developments and challenges”. In: *Applied Surface Science Advances* 12 (2022), p. 100332. ISSN: 2666-5239. DOI: `https://doi.org/10.1016/j.apsadv.2022.100332`. URL: `https://www.sciencedirect.com/science/article/pii/S2666523922001222`.

[16] M. Finšgar. “Electrochemical, 3D topography, XPS, and ToF-SIMS analyses of 4-methyl-2-phenylimidazole as a corrosion inhibitor for brass”. In: *Corrosion Science* 169 (2020), p. 108632. ISSN: 0010-938X. DOI: `https://doi.org/10.1016/j.corsci.2020.108632`. URL: `https://www.sciencedirect.com/science/article/pii/S0010938X20302468`.

[17] I. Iatsunskyi, G. Gottardi, V. Micheli, R. Canteri, E. Coy, and M. Bechelany. “Atomic layer deposition of palladium coated TiO2/Si nanopillars: ToF-SIMS, AES and XPS characterization study”. In: *Applied Surface Science* 542 (2021), p. 148603. ISSN: 0169-4332. DOI: `https://doi.org/10.1016/j.apsusc.2020.148603`. URL: `https://www.sciencedirect.com/science/article/pii/S0169433220333614`.

[18] I. Morawski and M. Nowicki. “Properties of Au film on Ru(0001) revealed by AES, LEED, and DEPES”. In: *Applied Surface Science* 569 (2021), p. 151100. ISSN: 0169-4332. DOI: `https://doi.org/10.1016/j.apsusc.2021.151100`. URL: `https://www.sciencedirect.com/science/article/pii/S0169433221021577`.

[19] S.-K. Otto, Y. Moryson, T. Krauskopf, K. Peppler, J. Sann, J. Janek, and A. Henss. “In-depth characterization of lithium-metal surfaces with XPS and ToF-SIMS: Toward better understanding of the passivation layer”. In: *Chemistry of Materials* 33.3 (2021), pp. 859–867.

[20] P. Cornette, S. Zanna, A. Seyeux, D. Costa, and P. Marcus. “The native oxide film on a model aluminium-copper alloy studied by XPS and ToF-SIMS”. In: *Corrosion Science* 174 (2020), p. 108837. ISSN: 0010-938X. DOI: `https://doi.org/10.1016/j.corsci.2020.108837`. URL: `https://www.sciencedirect.com/science/article/pii/S0010938X20309537`.

[21] A. Guilherme Buzanich, M. Radtke, K. V. Yusenko, T. M. Stawski, A. Kulow, C. T. Cakir, B. Röder, C. Naese, R. Britzke, M. Sintschuk, and F. Emmerling. “BAMline—A real-life sample materials research beamline”. In: *The Journal of Chemical Physics* 158.24 (June 2023), p. 244202. ISSN: 0021-9606. DOI: `10.1063/5.0157194`. eprint: `https://pubs.aip.org/aip/jcp/article-pdf/doi/10.1063/5.0157194/18016765/244202\_1\_5.0157194.pdf`. URL: `https://doi.org/10.1063/5.0157194`.

[22] S.-C. Lin, C.-C. Chang, S.-Y. Chiu, H.-T. Pai, T.-Y. Liao, C.-S. Hsu, W.-H. Chiang, M.-K. Tsai, and H. M. Chen. "Operando time-resolved X-ray absorption spectroscopy reveals the chemical nature enabling highly selective CO2 reduction". In: *Nature Communications* 11.1 (2020), p. 3525.

[23] Y. Kayser, J. Szlachetko, and J. Sà. "Scanning-free grazing emission x-ray fluorescence by means of an angular dispersive arrangement with a two-dimensional position-sensitive area detector". In: *Review of Scientific Instruments* 84.12 (Dec. 2013), p. 123102. ISSN: 0034-6748. DOI: `10.1063/1.4838575`. eprint: `https://pubs.aip.org/aip/rsi/article-pdf/doi/10.1063/1.4838575/15727982/123102\_1\_online.pdf`. URL: `https://doi.org/10.1063/1.4838575`.

[24] S. Staeck, A. Andrle, P. Hönicke, J. Baumann, D. Grötzsch, J. Weser, G. Goetzke, A. Jonas, Y. Kayser, F. Förste, et al. "Scan-Free GEXRF in the Soft X-ray Range for the Investigation of Structured Nanosamples". In: *Nanomaterials* 12.21 (2022), p. 3766.

[25] Y. Kayser, J. Sá, and J. Szlachetko. "Depth-resolved X-ray absorption spectroscopy by means of grazing emission x-ray fluorescence". In: *Analytical chemistry* 87.21 (2015), pp. 10815–10821.

[26] C. T. Cakir, T. Piotrowiak, U. Reinholz, A. Ludwig, F. Emmerling, C. Streli, A. Guilherme Buzanich, and M. Radtke. "Exploring the depths of corrosion: A novel GE-XANES technique for investigating compositionally complex alloys". In: *Analytical Chemistry* 95.10 (2023), pp. 4810–4818.

[27] R. S. Becker, J. A. Golovchenko, and J. R. Patel. "X-Ray Evanescent-Wave Absorption and Emission". In: *Physical Review Letters* 50.3 (1983), pp. 153–156. DOI: `10.1103/PhysRevLett.50.153`. URL: `https://link.aps.org/doi/10.1103/PhysRevLett.50.153`.

[28] S. Xiang, P. Huang, J. Li, Y. Liu, N. Marcella, P. K. Routh, G. Li, and A. I. Frenkel. "Solving the structure of "single-atom" catalysts using machine learning–assisted XANES analysis". In: *Physical Chemistry Chemical Physics* 24.8 (2022), pp. 5116–5124.

[29] A. Martini, A. Guda, S. Guda, A. Bugaev, O. Safonova, and A. Soldatov. “Machine learning powered by principal component descriptors as the key for sorted structural fit of XANES”. In: *Physical Chemistry Chemical Physics* 23.33 (2021), pp. 17873–17887.

[30] M. Vermeulen, A. McGeachy, B. Xu, H. Chopp, A. Katsaggelos, R. Meyers, M. Alfeld, and M. Walton. “XRFast a new software package for processing of MA-XRF datasets using machine learning”. In: *Journal of Analytical Atomic Spectrometry* 37.10 (2022), pp. 2130–2143.

[31] A. Kulow, A. G. Buzanich, U. Reinholz, F. Emmerling, S. Hampel, U. E. A. Fittschen, C. Streli, and M. Radtke. “Comparison of three reconstruction methods based on deconvolution, iterative algorithm and neural network for X-ray fluorescence imaging with coded aperture optics”. In: *Journal of Analytical Atomic Spectrometry* 35.7 (2020), pp. 1423–1434.

[32] S. M. Moosavi, K. M. Jablonka, and B. Smit. “The role of machine learning in the understanding and design of materials”. In: *Journal of the American Chemical Society* 142.48 (2020), pp. 20273–20287.

[33] N. Fujinuma, B. DeCost, J. Hattrick-Simpers, and S. E. Lofland. “Why big data and compute are not necessarily the path to big materials science”. In: *Communications Materials* 3.1 (2022), p. 59.

[34] A. Lee, S. Sarker, J. E. Saal, L. Ward, C. Borg, A. Mehta, and C. Wolverton. “Machine learned synthesizability predictions aided by density functional theory”. In: *Communications Materials* 3.1 (2022), p. 73.

[35] A. Davariashtiyani, Z. Kadkhodaie, and S. Kadkhodaei. “Predicting synthesizability of crystalline materials via deep learning”. In: *Communications Materials* 2.1 (2021), p. 115.

[36] C. Kuenneth, J. Lalonde, B. L. Marrone, C. N. Iverson, R. Ramprasad, and G. Pilania. “Bioplastic design using multitask deep neural networks”. In: *Communications Materials* 3.1 (2022), p. 96.

[37] K. S. Mao, T. J. Gerczak, J. M. Harp, C. S. McKinney, T. G. Lach, O. Karakoc, A. T. Nelson, K. A. Terrani, C. M. Parish, and P. D. Edmondson. “Identifying chemically similar multiphase nanoprecipitates in compositionally complex non-equilibrium oxides via machine learning”. In: *Communications Materials* 3.1 (2022), p. 21.

[38] A. Samarakoon, D. A. Tennant, F. Ye, Q. Zhang, and S. A. Grigera. “Integration of machine learning with neutron scattering for the Hamiltonian tuning of spin ice under pressure”. In: *Communications Materials* 3.1 (2022), p. 84.

[39] A. G. Kusne, H. Yu, C. Wu, H. Zhang, J. Hattrick-Simpers, B. DeCost, S. Sarker, C. Oses, C. Toher, S. Curtarolo, et al. “On-the-fly closed-loop materials discovery via Bayesian active learning”. In: *Nature communications* 11.1 (2020), p. 5966.

[40] Y. Zhang, R. Xie, T. Long, D. Günzing, H. Wende, K. J. Ollefs, and H. Zhang. “Autonomous atomic Hamiltonian construction and active sampling of X-ray absorption spectroscopy by adversarial Bayesian optimization”. In: *npj Computational Materials* 9.1 (2023), p. 46.

[41] M. Teixeira Parente, G. Brandl, C. Franz, U. Stuhr, M. Ganeva, and A. Schneidewind. “Active learning-assisted neutron spectroscopy with log-Gaussian processes”. In: *Nature Communications* 14.1 (2023), p. 2246.

[42] D. R. Jones, M. Schonlau, and W. J. Welch. “Efficient global optimization of expensive black-box functions”. In: *Journal of Global optimization* 13 (1998), pp. 455–492.

[43] B. Settles. “From theories to queries: Active learning in practice”. In: *Active learning and experimental design workshop in conjunction with AISTATS 2010*. JMLR Workshop and Conference Proceedings. 2011, pp. 1–18.

[44] E. Burnaev and M. Panov. “Adaptive design of experiments based on gaussian processes”. In: *Statistical Learning and Data Sciences: Third International Symposium, SLDS 2015, Egham, UK, April 20-23, 2015, Proceedings 3*. Springer. 2015, pp. 116–125.

[45] H. Liu, S. Xu, Y. Ma, X. Chen, and X. Wang. “An adaptive Bayesian sequential sampling approach for global metamodeling”. In: *Journal of Mechanical Design* 138.1 (2016), p. 011404.

[46] N. Houlsby, F. Huszár, Z. Ghahramani, and M. Lengyel. “Bayesian active learning for classification and preference learning”. In: *arXiv preprint arXiv:1112.5745* (2011).

[47] A. Rakotondrajoa and M. Radtke. “Machine learning based quantification of synchrotron radiation-induced x-ray fluorescence measurements—a case study”. In: *Machine Learning: Science and Technology* 2.2 (2020), p. 025004.

[48] V. Starostin, L. Pithan, A. Greco, V. Munteanu, A. Gerlach, A. Hinderhofer, and F. Schreiber. “End-to-End Deep Learning Pipeline for Real-Time Processing of Surface Scattering Data at Synchrotron Facilities”. In: *Synchrotron radiation newS* 35.4 (2022), pp. 21–27.

[49] S. I. Campbell, D. B. Allan, A. M. Barbour, D. Olds, M. S. Rakitin, R. Smith, and S. B. Wilkins. “Outlook for artificial intelligence and machine learning at the NSLS-II”. In: *Machine Learning: Science and Technology* 2.1 (2021), p. 013001.

[50] T. Konstantinova, P. M. Maffettone, B. Ravel, S. I. Campbell, A. M. Barbour, and D. Olds. “Machine learning enabling high-throughput and remote operations at large-scale user facilities”. In: *Digital Discovery* 1.4 (2022), pp. 413–426.

[51] T. Ueno and H. Iwasawa. “Measurement Informatics in Synchrotron Radiation X-Ray Spectroscopy”. In: *Synchrotron Radiation News* 35.4 (2022), pp. 3–8.

[52] B. Shahriari, K. Swersky, Z. Wang, R. P. Adams, and N. De Freitas. “Taking the human out of the loop: A review of Bayesian optimization”. In: *Proceedings of the IEEE* 104.1 (2015), pp. 148–175.

[53] M. M. Noack, P. H. Zwart, D. M. Ushizima, M. Fukuto, K. G. Yager, K. C. Elbert, C. B. Murray, A. Stein, G. S. Doerk, E. H. Tsai, et al. “Gaussian processes for autonomous data acquisition at large-scale synchrotron and neutron facilities”. In: *Nature Reviews Physics* 3.10 (2021), pp. 685–697.

[54] Editors of Encyclopaedia Britannica. *Electromagnetic Spectrum.* Accessed on November 19, 2024. Oct. 2024. URL: `https://www.britannica.com/science/electromagnetic-spectrum`.

[55] J. Hubbell. “Review of photon interaction cross section data in the medical and biological context”. In: *Physics in Medicine & Biology* 44.1 (1999), R1.

[56] U. Tardad. “Supreme Theory of Everything: A New Quantum Concept of the Photoelectric Effect”. In: *London Journals of Research in Science: Natural and Formal* 22.14 (2022), pp. 1–12.

[57] H. C. Ishikawa-Ankerhold, R. Ankerhold, and G. P. Drummen. “Advanced fluorescence microscopy techniques—Frap, Flip, Flap, Fret and flim”. In: *Molecules* 17.4 (2012), pp. 4047–4132.

[58] L. Meitner. “Über die β-Strahl-Spektra und ihren Zusammenhang mit der γ-Strahlung”. In: *Zeitschrift für Physik* 11 (1922), pp. 35–54.

[59] P. Auger. “Sur l’effet photoélectrique composé”. In: *J. Phys. Radium* 6.6 (1925), pp. 205–208.

[60] B. K. Agarwal and B. K. Agarwal. “Scattering of X-rays”. In: *X-Ray Spectroscopy: An Introduction* (1991), pp. 195–206.

[61] J. Als-Nielsen and D. McMorrow. *Elements of modern X-ray physics.* John Wiley & Sons, 2011.

[62] S. M. Midgley. “A parameterization scheme for the x-ray linear attenuation coefficient and energy absorption coefficient”. In: *Physics in Medicine & Biology* 49.2 (2004), p. 307.

[63] R. Jenkins et al. *X-ray fluorescence spectrometry.* Vol. 2. Wiley Online Library, 1999.

[64] B. Beckhoff, B. Kanngießer, N. Langhoff, R. Wedell, and H. Wolff. *Handbook of practical X-ray fluorescence analysis.* Springer Science & Business Media, 2007.

[65] Y. Yoneda and T. Horiuchi. “Optical flats for use in X-ray spectrochemical microanalysis”. In: *Review of scientific instruments* 42.7 (1971), pp. 1069–1070.

[66] H. Aiginger, P. Wobrauschek, and C. Streli. “Principles and development of total reflection X-ray fluorescence analysis”. In: *Analytical sciences* 11.3 (1995), pp. 471–475.

[67] F. Meirer, A. Singh, P. Pianetta, G. Pepponi, C. Streli, and T. Homma. “Synchrotron radiation-induced total reflection X-ray fluorescence analysis”. In: *TrAC Trends in Analytical Chemistry* 29.6 (2010), pp. 479–496.

[68] P. Wobrauschek. “Total reflection x-ray fluorescence analysis—a review”. In: *X-Ray Spectrometry: An International Journal* 36.5 (2007), pp. 289–300.

[69] M. Schmeling. “Total reflection X-ray fluorescence”. In: *Physical Sciences Reviews* 4.7 (2019), p. 20170161.

[70] Y. Kayser, J. Szlachetko, D. Banaś, W. Cao, J.-C. Dousse, J. Hoszowska, A. Kubala-Kukuś, and M. Pajek. “High-energy-resolution grazing emission X-ray fluorescence applied to the characterization of thin Al films on Si”. In: *Spectrochimica Acta Part B: Atomic Spectroscopy* 88 (2013), pp. 136–149.

[71] L. G. Parratt. “Surface studies of solids by total reflection of X-rays”. In: *Physical review* 95.2 (1954), p. 359.

[72] A. Iida, K. Sakurai, A. Yoshinaga, and Y. Gohshi. “Grazing incidence X-ray fluorescence analysis”. In: *Nuclear Instruments and Methods in Physics Research Section A: Accelerators, Spectrometers, Detectors and Associated Equipment* 246.1-3 (1986), pp. 736–738.

[73] D. K. de Boer. “Glancing-incidence x-ray fluorescence of layered materials”. In: *Physical Review B* 44.2 (1991), p. 498.

[74] D. Ingerle, F. Meirer, G. Pepponi, E. Demenev, D. Giubertoni, P. Wobrauschek, and C. Streli. “Combined evaluation of grazing incidence X-ray fluorescence and X-ray reflectivity data for improved profiling of ultra-shallow depth distributions”. In: *Spectrochimica Acta Part B: Atomic Spectroscopy* 99 (2014), pp. 121–128.

[75] P. Hönicke, U. Waldschläger, T. Wiesner, M. Krämer, and B. Beckhoff. “Towards a calibration of laboratory setups for grazing incidence and total-reflection X-ray fluorescence analysis”. In: *Spectrochimica Acta Part B: Atomic Spectroscopy* 174 (2020), p. 106009.

[76] H. Urbach and P. De Bokx. “Calculation of intensities in grazing-emission X-ray fluorescence”. In: *Physical Review B* 53.7 (1996), p. 3752.

[77] Y. Kayser. “Synchrotron radiation based high–resolution grazing emission X–ray fluorescence”. PhD thesis. Université de Fribourg, 2011.

[78] J. Szlachetko, D. Banaś, A. Kubala-Kukuś, M. Pajek, W. Cao, J.-C. Dousse, J. Hoszowska, Y. Kayser, M. Szlachetko, M. Kavčič, et al. “Application of the high-resolution grazing-emission x-ray fluorescence method for impurities control in semiconductor nanotechnology”. In: *Journal of Applied Physics* 105.8 (2009).

[79] A. Kubala-Kukuś, D. Banaś, W. Cao, J.-C. Dousse, J. Hoszowska, Y. Kayser, M. Pajek, M. Salomé, J. Susini, J. Szlachetko, et al. “Observation of ultralow-level Al impurities on a silicon surface by high-resolution grazing emission x-ray fluorescence excited by synchrotron radiation”. In: *Physical Review B* 80.11 (2009), p. 113305.

[80] Y. Kayser, D. Banaś, W. Cao, J.-C. Dousse, J. Hoszowska, P. Jagodziński, M. Kavčič, A. Kubala-Kukuś, S. Nowak, M. Pajek, et al. “Depth profiles of Al impurities implanted in Si wafers determined by means of the high-resolution grazing emission X-ray fluorescence technique”. In: *Spectrochimica Acta Part B: Atomic Spectroscopy* 65.6 (2010), pp. 445–449.

[81] S. H. Nowak, D. Banaś, W. Błchucki, W. Cao, J.-C. Dousse, P. Hönicke, J. Hoszowska, Y. Kayser, A. Kubala-Kukuś, M. Pajek, et al. “Grazing angle X-ray fluorescence from periodic structures on silicon and silica surfaces”. In: *Spectrochimica Acta Part B: Atomic Spectroscopy* 98 (2014), pp. 65–75.

[82] Y. Kayser, J. Sá, and J. Szlachetko. “Nanoparticle characterization by means of scanning free grazing emission X-ray fluorescence”. In: *Nanoscale* 7.20 (2015), pp. 9320–9330.

[83] V. Szwedowski, J. Baumann, I. Mantouvalou, L. Bauer, W. Malzer, and B. Kanngießer. “Scan-Free Grazing Emission XRF Measurements in the Laboratory Using a CCD”. In: *physica status solidi c* 14.12 (2017), p. 1700158.

[84] R. Santos, D. Oliveira, J. Assis, and M. Anjos. “Development of a portable grazing exit X-ray fluorescence system using a gold anode X-ray tube”. In: *Radiation Physics and Chemistry* 167 (2020), p. 108245.

[85] T. Ashida and K. Tsuji. “Development of a compact grazing exit X-ray fluorescence spectrometer for fast trace elemental analysis”. In: *Spectrochimica Acta Part B: Atomic Spectroscopy* 101 (2014), pp. 200–203.

[86] T. Noma, K. Takada, and A. Iida. “Surface-sensitive x-ray fluorescence and diffraction analysis with grazing-exit geometry”. In: *X-Ray Spectrometry: An International Journal* 28.6 (1999), pp. 433–439.

[87] M. Monaghan, T. Nigam, M. Houssa, S. De Gendt, H. Urbach, and P. De Bokx. “Characterization of silicon oxynitride films by grazing-emission X-ray fluorescence spectrometry”. In: *Thin Solid Films* 359.2 (2000), pp. 197–202.

[88] P. Hönicke, Y. Kayser, B. Beckhoff, M. Müller, J.-C. Dousse, J. Hoszowska, and S. H. Nowak. “Characterization of ultra-shallow aluminum implants in silicon by grazing incidence and grazing emission X-ray fluorescence spectroscopy”. In: *Journal of Analytical Atomic Spectrometry* 27.9 (2012), pp. 1432–1438.

[89] Y. Kayser, J. Sá, and J. Szlachetko. “Depth-Resolved X-ray Absorption Spectroscopy by Means of Grazing Emission X-ray Fluorescence”. In: *Analytical Chemistry* 87.21 (2015). PMID: 26458105, pp. 10815–10821. DOI: `10.1021/acs.analchem.5b03346`. eprint: `https://doi.org/10.1021/acs.analchem.5b03346`. URL: `https://doi.org/10.1021/acs.analchem.5b03346`.

[90] F. Meirer, G. Pepponi, C. Streli, P. Wobrauschek, and N. Zoeger. “Grazing exit versus grazing incidence geometry for x-ray absorption near edge structure analysis of arsenic traces”. In: *Journal of Applied Physics* 105.7 (Apr. 2009), p. 074906. ISSN: 0021-8979. DOI: `10.1063/1.3106086`. eprint: `https://pubs.aip.org/aip/jap/`

article-pdf/doi/10.1063/1.3106086/15031948/074906_1_online.pdf. URL: https://doi.org/10.1063/1.3106086.

[91] H. Urbach and P. de Bokx. "Grazing emission x-ray fluorescence from multilayers". In: *Physical Review B* 63.8 (2001), p. 085408.

[92] J. T. Bushberg and J. M. Boone. *The essential physics of medical imaging*. Lippincott Williams & Wilkins, 2011.

[93] O. Hemberg, M. Otendal, and H. Hertz. "Liquid-metal-jet anode electron-impact x-ray source". In: *Applied Physics Letters* 83.7 (2003), pp. 1483–1485.

[94] J. Baumann, Y. Kayser, and B. Kanngießer. "Grazing emission X-ray fluorescence: Novel concepts and applications for nano-analytics". In: *physica status solidi (b)* 258.3 (2021), p. 2000471.

[95] G. Margaritondo. "Who were the founders of synchrotron radiation? Historical facts and misconceptions". In: *Journal of Vacuum Science & Technology A* 40.3 (2022).

[96] S. Mobilio, F. Boscherini, C. Meneghini, et al. *Synchrotron Radiation*. Springer, 2016.

[97] Santarelli. *EPSIM 3D/JF, Synchrotron Soleil*. https://de.m.wikipedia.org/wiki/Datei:Sch%C3%A9ma_de_principe_du_synchrotron.jpg [Accessed: (28.02.2024)]. 2022.

[98] Y. Sasaki, Y. Suzuki, Y. Tomioka, and A. Fukuhara. "Observation of an interference effect for fluorescent x rays". In: *Physical Review B* 48.10 (1993), p. 7724.

[99] W. Grünert and K. Klementiev. "X-ray absorption spectroscopy principles and practical use in materials analysis". In: *Physical Sciences Reviews* 5.4 (2020), p. 20170181.

[100] G. Bunker. *Introduction to XAFS: a practical guide to X-ray absorption fine structure spectroscopy*. Cambridge University Press, 2010.

[101] A. Gaur, B. D. Shrivastava, and H. Nigam. "X-ray absorption fine structure (XAFS) spectroscopy–a review". In: *Proc. Indian Natl. Sci. Acad.* Vol. 79. 2013, pp. 921–966.

[102] J. J. Rehr and R. C. Albers. “Theoretical approaches to x-ray absorption fine structure”. In: *Reviews of modern physics* 72.3 (2000), p. 621.

[103] A. Tharwat and W. Schenck. “A survey on active learning: State-of-the-art, practical challenges and research directions”. In: *Mathematics* 11.4 (2023), p. 820.

[104] S. Tong. *Active learning: theory and applications*. Stanford University, 2001.

[105] B. Settles. “Active learning literature survey”. In: (2009).

[106] S. C. Hoi, R. Jin, and M. R. Lyu. “Large-scale text categorization by batch mode active learning”. In: *Proceedings of the 15th international conference on World Wide Web*. 2006, pp. 633–642.

[107] S. Tong and D. Koller. “Support vector machine active learning with applications to text classification”. In: *Journal of machine learning research* 2.Nov (2001), pp. 45–66.

[108] D. D. Lewis. “A sequential algorithm for training text classifiers: Corrigendum and additional data”. In: *Acm Sigir Forum*. Vol. 29. 2. ACM New York, NY, USA. 1995, pp. 13–19.

[109] H. S. Seung, M. Opper, and H. Sompolinsky. “Query by committee”. In: *Proceedings of the fifth annual workshop on Computational learning theory*. 1992, pp. 287–294.

[110] B. Settles, M. Craven, and S. Ray. “Multiple-instance active learning”. In: *Advances in neural information processing systems* 20 (2007).

[111] N. Roy and A. McCallum. “Toward optimal active learning through monte carlo estimation of error reduction”. In: *ICML, Williamstown* 2 (2001), pp. 441–448.

[112] J. B. Mockus and L. J. Mockus. “Bayesian approach to global optimization and application to multiobjective and constrained problems”. In: *J. Optim. Theory Appl.* 70.1 (July 1991), pp. 157–172.

[113] E. Schulz, M. Speekenbrink, and A. Krause. “A tutorial on Gaussian process regression: Modelling, exploring, and exploiting functions”. In: *Journal of Mathematical Psychology* 85 (2018), pp. 1–16. ISSN: 0022-2496. DOI: `https://doi.org/10.`

1016/j.jmp.2018.03.001. URL: https://www.sciencedirect.com/science/article/pii/S0022249617302158.

[114] R. Garnett. *Bayesian optimization.* Cambridge University Press, 2023.

[115] C. K. Williams and C. E. Rasmussen. *Gaussian processes for machine learning.* Vol. 2. 3. MIT press Cambridge, MA, 2006.

[116] F. Armborst. "Study and Optimization of the Transverse Beam Parameters before Injection into the Storage Ring BESSY II". PhD thesis. Sept. 2019. DOI: 10.18452/20386.

[117] A. Kulow. "Spatial resolved dispersive X-ray absorption spectroscopy and coded aperture X-ray fuorescence imaging". PhD thesis. Wien, 2020.

[118] O. Schwarzkopf, A. Jankowiak, A. Vollmer, and B. I. I. team. "Materials discovery at BESSY". In: *The European Physical Journal Plus* 138.4 (2023), p. 348.

[119] W. Görner, M. Hentschel, B. Müller, H. Riesemeier, M. Krumrey, G. Ulm, W. Diete, U. Klein, and R. Frahm. "BAMline: the first hard X-ray beamline at BESSY II". In: *Nuclear Instruments and Methods in Physics Research Section A: Accelerators, Spectrometers, Detectors and Associated Equipment* 467-468 (2001). 7th Int.Conf. on Synchrotron Radiation Instrumentation, pp. 703–706. ISSN: 0168-9002. DOI: https://doi.org/10.1016/S0168-9002(01)00466-1. URL: https://www.sciencedirect.com/science/article/pii/S0168900201004661.

[120] A. Erko and I. Zizak. "Hard X-ray micro-spectroscopy at Berliner Elektronenspeicherring für Synchrotronstrahlung II". In: *Spectrochimica Acta Part B: Atomic Spectroscopy* 64.9 (2009), pp. 833–848. ISSN: 0584-8547. DOI: https://doi.org/10.1016/j.sab.2009.07.003. URL: https://www.sciencedirect.com/science/article/pii/S0584854709001785.

[121] I. Zizak. "mySpot: a versatile microfocussing station for scanning methods at BESSY II". In: *Journal of large-scale research facilities JLSRF* 2 (2016), A101–A101.

[122] I. Zizak. "The mySpot beamline at BESSY II". In: *Journal of large-scale research facilities JLSRF* 2 (2016), A102–A102.

[123] V. Borovikov, V. Djurba, M. Fedurin, V. Repkov, G. Karpov, G. Kulipanov, M. Kuzin, N. Mezentsev, V. Shkaruba, D. Kraemer, and D. Richter. "Superconducting 7T Wave Length Shifter for BESSY-II". In: *Nuclear Instruments and Methods in Physics Research Section A: Accelerators, Spectrometers, Detectors and Associated Equipment* 467-468 (2001). 7th Int.Conf. on Synchrotron Radiation Instrumentation, pp. 181–184. ISSN: 0168-9002. DOI: `https://doi.org/10.1016/S0168-9002(01)00269-8`. URL: `https://www.sciencedirect.com/science/article/pii/S0168900201002698`.

[124] A. Batrakov, E. Bekhtenev, V. Borovikov, V. Djurba, M. Fedurin, V. Repkov, G. Karpov, S. Khruschev, G. Kulipanov, M. Kuzin, V. Lev, and N. Mezentsev. "Superconducting wave length shifters and multipole wigglers developed in Budker INP." In: (Jan. 2001).

[125] A. Erko, F. Schäfers, A. Firsov, W. Peatman, W. Eberhardt, and R. Signorato. "The BESSY X-ray microfocus beamline project". In: *Spectrochimica Acta Part B: Atomic Spectroscopy* 59.10 (2004). 17th International Congress on X-Ray Optics and Microanalysis, pp. 1543–1548. ISSN: 0584-8547. DOI: `https://doi.org/10.1016/j.sab.2004.03.015`. URL: `https://www.sciencedirect.com/science/article/pii/S0584854704001880`.

[126] O. Scharf, S. Ihle, I. Ordavo, V. Arkadiev, A. Bjeoumikhov, S. Bjeoumikhova, G. Buzanich, R. Gubzhokov, A. Günther, R. Hartmann, M. Kühbacher, M. Lang, N. Langhoff, A. Liebel, M. Radtke, U. Reinholz, H. Riesemeier, H. Soltau, L. Strüder, A. F. Thünemann, and R. Wedell. "Compact pnCCD-Based X-ray Camera with High Spatial and Energy Resolution: A Color X-ray Camera". In: *Analytical Chemistry* 83.7 (2011). PMID: 21355541, pp. 2532–2538. DOI: `10.1021/ac102811p`. eprint: `https://doi.org/10.1021/ac102811p`. URL: `https://doi.org/10.1021/ac102811p`.

[127] I. Ordavo, S. Ihle, V. Arkadiev, O. Scharf, H. Soltau, A. Bjeoumikhov, S. Bjeoumikhova, G. Buzanich, R. Gubzhokov, A. Günther, R. Hartmann, P. Holl, N. Kimmel, M. Kühbacher, M. Lang, N. Langhoff, A. Liebel, M. Radtke, U. Reinholz, H. Riesemeier, G. Schaller, F. Schopper, L. Strüder, C. Thamm, and R. Wedell. "A new pnCCD-

based color X-ray camera for fast spatial and energy-resolved measurements". In: *Nuclear Instruments and Methods in Physics Research Section A: Accelerators, Spectrometers, Detectors and Associated Equipment* 654.1 (2011), pp. 250–257. ISSN: 0168-9002. DOI: `https://doi.org/10.1016/j.nima.2011.05.080`. URL: `https://www.sciencedirect.com/science/article/pii/S0168900211011715`.

[128] Y.-X. Wang and Y.-J. Zhang. "Nonnegative Matrix Factorization: A Comprehensive Review". In: *IEEE Transactions on Knowledge and Data Engineering* 25.6 (2013), pp. 1336–1353. DOI: `10.1109/TKDE.2012.51`.

[129] F. G. Coury, G. Zepon, and C. Bolfarini. "Multi-principal element alloys from the CrCoNi family: outlook and perspectives". In: *Journal of Materials Research and Technology* 15 (2021), pp. 3461–3480.

[130] G. Laplanche, A. Kostka, C. Reinhart, J. Hunfeld, G. Eggeler, and E. George. "Reasons for the superior mechanical properties of medium-entropy CrCoNi compared to high-entropy CrMnFeCoNi". In: *Acta Materialia* 128 (2017), pp. 292–303.

[131] M. Mohammadtaheri, Q. Yang, Y. Li, and J. Corona-Gomez. "The effect of deposition parameters on the structure and mechanical properties of chromium oxide coatings deposited by reactive magnetron sputtering". In: *Coatings* 8.3 (2018), p. 111.

[132] C. D. Wagner. "NIST X-ray photoelectron spectroscopy database". In: *NIST Standarad Reference Database 20* (2000).